The Dissertation Committee for Isaac Vicente Manzanera Esteve
certifies that this is the approved version of the following dissertation:

Development of Variable Temperature NMR Force Microscopy: Proton Spin Relaxation Measurements in Ammonium Sulfate

Committee:

John T. Markert, Supervisor

Alejandro de Lozanne

Xiaoqin Li

Zhen Yao

John Goodenough

Development of Variable Temperature NMR Force Microscopy: Proton Spin Relaxation Measurements in Ammonium Sulfate

by

Isaac Vicente Manzanera Esteve, B.S.

DISSERTATION

Presented to the Faculty of the Graduate School of

The University of Texas at Austin

in Partial Fulfillment

of the Requirements

for the Degree of

DOCTOR OF PHILOSOPHY

THE UNIVERSITY OF TEXAS AT AUSTIN

August 2012

To my wife, mother, father and sister.

Acknowledgments

I would like to thanks first of all to my wife, Julia Raymond, my parents, Vicente and Rosa, and my syster Diana. Their love, support and help made possible this journey. Their wise advice makes them partly responsible for this success.

I would like to thank also those who crossed paths with mine during all these years. Wei Lu, thanks for your help to start this journey with Labview. Yong J. Lee, thanks for being always available and very helpful with technical questions about stages and electronics. Han-Jong Chia, thanks for your help starting to put together in my mind some of the pieces of the puzzle that is NMRFM. Rosa Cardenas, you have been a great lab mate and very helpful with the day-to-day frustrations. Jeremy Paster, thanks for your help with the ups and downs of the lab. Mark Monti and Dan Tennant, you have made of the lab a cool place to work and think about NMRFM and physics. Amanda Turbyfill and Jonathan Weyn your help, with editing and with the day-to-day construction of the NMR and NMRFM experiments is greatly appreciated. Neliza and Morgann thanks for sharing tools and help with ideas to overcome the everyday technical problems.

I want especially to thank Alex de Lozanne for his help, advice and guidance. Chih-Kang (Ken) Shih, thanks for challenging me or some times just listening when it was necessary. I would finally like to thank John T. Markert, first of all for his trust; letting a new graduate student come to the lab with crazy ideas and start changing everything is not easy to accept. Thanks for his support, to develop this new system and for always listening to my new ideas. Your recommendations have been very helpful.

Development of Variable Temperature NMR Force Microscopy: Proton Spin Relaxation Measurements in Ammonium Sulfate

Publication No. ________________

Isaac Vicente Manzanera Esteve, Ph.D.
The University of Texas at Austin, 2012

Supervisor: John T. Markert

Nuclear magnetic resonance force microscopy (NMRFM) of a micron size sample of ammonium sulfate was performed by measuring the cantilever deflection produced by coupling the magnetic force to a mechanical cantilever at its resonance frequency. Spin-lattice and spin-spin relaxation measurements were obtained with our newly developed NMRFM probe.

A system with more advanced positioning, acquisition and analysis has been fabricated. A new device in which a semi-automatic system performs nanoposition control, spin manipulation, dynamical measurements, and data analysis has been demonstrated to be successful. The new system has proven to be an improvement with respect to other versions of NMRFM probes, thanks to its versatility for pulse sequence designs, faster data acquisition, and automatic analysis of the information.

This thesis presents an explanation of the theoretical details of nuclear magnetic resonance force microscopy, and experiments are described in which dynamical measurements of proton spin interactions are obtained.

Finally, relaxation time effects of the observed force signal are considered in detail. A novel spin manipulation technique which is being implemented for future measurements is described in detail, and magnet configurations for larger magnetic field gradients and consequently larger signal-to-noise ratio, are also described.

Table of Contents

Chapter 4. Experimental NMRFM System 57

Chapter 1

Introduction

Magnetic Resonance Force Microscopy (MRFM) is the name given to the field that couples forces generated by resonantly precessing spins in a magnetic field gradient with a cantilever at its resonance frequency. This technique was proposed initially by John Sidles in 1991 [1] as a potential method for performing three dimensional imaging of biological molecules and its viability was demonstrated in 1992 by Dan Rugar and John Sidles [2] in an electron spin resonance signal measurement. In this first attempt, a force of 10^{-14} N was generated with a spatial resolution of 19 μm in one dimension. That result was still far from the single atomic, three dimensional resolution necessary for protein structure determination. However, several groups' efforts have been developing improvements in the technique, in one, C. L. Degen, M Poggio, H. J. Mamin, C. T. Rettner, and D. Rugar [3] detected, with three dimensional resolution, less than 100 nuclear spins in a 4-nm-thick slice.

Even though this resolution is approximately 10^8 times better than the best signal obtained by conventional Magnetic Resonance Imaging (MRI), a 100 times improvement from the last best result is still needed to measure the challenging force signal of 10^{-19} N generated by a single proton [4]. In order to achieve single nuclear spin detection, a substantial improvement in the generation of larger gradient fields and also in cantilevers with smaller spring constants, larger quality factors and larger resonance frequencies that will provide better force sensitivity measurements will be required.

This dissertation first reviews, in Chapter 2, the principles of how magnetic moments behave in magnetic fields. Later on we move into spin manipulation techniques and from there introduce the basics of Nuclear Magnetic Resonance Force Microscopy and how and which useful information can be obtained using this technique. This thesis will then focus, in Chapter 3, on describing the theoretical foundations and experimental details involved in NMRFM. With this background, a thorough explanation of the efforts behind the fabrication, design, and characterization of a variable temperature probe is described in Chapter 4. A discussion of the experiment performed and results obtained will be provided in Chapter 5, including the measurements of the spin-spin and the spin-lattice relaxation times, (44 ± 2 μs) and (5.6 ± 0.7 s) respectively, of proton spins in a micron scale ammonium sulfate sample with a resolution of 11 to 16 μm. To finalize this dissertation, a discussion of the development of this technique that can possibly allow us to achieve atomic resolution in future work is provided.

Chapter 2

Foundations of Magnetic Resonance

2.1 Introduction

Magnetic resonance is a spectroscopic phenomenon that takes place when a magnetic system in which its magnetic moments $\vec{\mu}$ precess around an external magnetic field $\vec{B}$ is perturbed by an electromagnetic absorption or emission equal to the difference in energy between two energy levels of the system [5],[6].

This chapter tries to answer questions about how spins can be manipulated using magnetic fields that vary in tune with the precession frequency of the magnetic moments, and also discusses the types of information that can be obtained about the magnetic system using magnetic resonance.

2.2 Spin Precession in a Magnetic Field

The result of the interaction between an external magnetic field $\vec{B}$, which will be assumed to be pointing always along the z axis, $\vec{B} = B_0\hat{z}$, and the magnetic moment $\vec{\mu}$ of a nucleus is the establishment of an energy state with a Hamiltonian given by [5]:

$$\mathcal{H} = -\vec{\mu} \cdot \vec{B} \tag{2.1}$$

Here the magnetic moment is described by $\vec{\mu} = \gamma \vec{J} = \gamma \hbar \vec{I}$, where γ is the gyromagnetic ratio, $\vec{J}$ is the total angular momentum and $\vec{I}$ is the spin angular momentum operator in units of $\hbar$. The product $\vec{\mu} \cdot \vec{B}$ then gives

$$\mathcal{H} = -\ \gamma \hbar B_0 I_z, \tag{2.2}$$

where I_z is the z-component of the angular momentum operator and its eigenvalues are denoted by $m = I, I-1, ..., -I$. The final expression of the magnetic energy is thus described by

$$E = -\ \gamma \hbar B_0 m. \tag{2.3}$$

In the case of a magnetic moment with spin 1/2 there are two possible values of m, $+1/2$ and $-1/2$, corresponding to the two energy levels available in the system. The energy difference between these two states is given by:

$$\Delta E = \gamma \hbar B_0 = \hbar \omega_0 \tag{2.4}$$

Here ΔE represents the energy that an electromagnetic field must match to be absorbed by the magnetic moments and induce a transition from one state to another. This energy difference is directly proportional to the gyromagnetic ratio, an intrinsic property of the type of nuclei, and the magnetic field, a variable of the system. An example of this energy difference as a function of the magnetic field is shown in Figure 2.1.

When the magnetic moments $\vec{\mu}$ are placed in a magnetic field $\vec{B_0}$, a torque, or the rate of change of the angular momentum is induced, causing the magnetic moments to precess at the Larmor frequency [7]

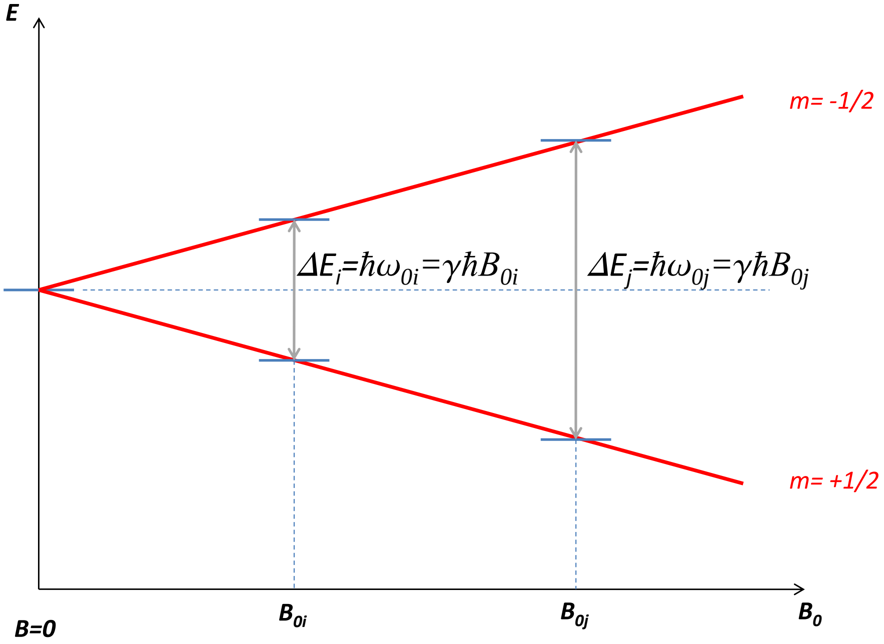

Figure 2.1: Energy levels and energy differences between the two states as a function of the intensity of the magnetic field B_0. When $B_0 = 0$ there is only one energy level, when $B_0 = B_{0i}$ the energy level for spin 1/2 is split in two and ΔE_i is the energy necessary to perform a transition between states. A similar situation happens for ΔE_j for $B_0 = B_{0j}$.

$$\vec{\tau} = \frac{d\vec{J}}{dt} = \vec{\mu} \times \vec{B} \tag{2.5}$$

The equation of motion that describes the precession of the magnetic moments is

$$\frac{d\vec{\mu}}{dt} = \vec{\mu} \times \left(\gamma\vec{B}\right) \tag{2.6}$$

where $\gamma B = \omega_0$ is the precession frequency. These definitions are valid for a single magnetic moment, and a more detailed description for the net magnetization is discussed below.

2.3 Boltzmann Polarization

When the system is composed of multiple magnetic moments with spin 1/2 in a magnetic field , the ratio between the number of spins in the higher energy state (N_-, spin down) and lower energy state (N_+, spin up), separated by a energy difference ΔE, is described by the Boltzmann distribution [5], [6]:

$$\frac{N_-}{N_+} = e^{-\Delta E/k_B T} = e^{-\gamma\hbar B_0/k_B T} \tag{2.7}$$

This equation shows the magnetic polarization dependency on the magnetic field and temperature, where k_B is the Boltzmann constant and T is the temperature of the system. The net magnetic moment is defined to be the product of the magnetic moment and the difference between the number of magnetic moments in the higher and lower energy states,

$$M_z = \mu(N_- - N_+) \tag{2.8}$$

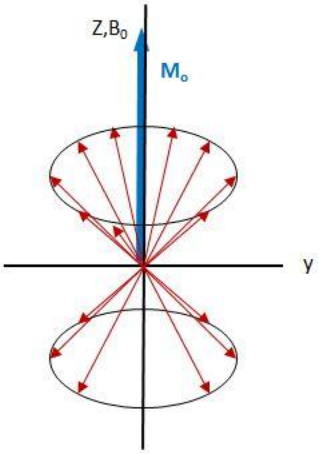

Figure 2.2: Difference in magnetic moment population due to Boltzmann polarization.

Using Equation (2.7) and $N = N_+ + N_-$, the description of the net magnetic moment in equilibrium, M_0, is

$$M_0 = N\mu \tanh\left(\frac{\mu B_0}{k_B T}\right) \tag{2.9}$$

Since the external magnetic field was described as $\vec{B} = B_0\hat{z}$, the net equilibrium magnetization only has z-component. For states when the ratio $\dfrac{\mu B_0}{k_B T} \ll 1,\ \tanh x \cong x$, Equation (2.9) can be expressed as:

$$M_0 = M_z = \chi_0 B_0 = \frac{C}{T} B_0 \tag{2.10}$$

where $C = \dfrac{N\mu^2}{k_B}$ is the Curie constant and $\chi_0 = C/T$ is the magnetic susceptibility [6, 8].

2.4 Spin Dynamics and Magnetic Resonance

Equation (2.5) describes the dynamics of a magnetic moment $\vec{\mu}$ when it is submerged in a magnetic field $\vec{B}_0$. The equation of motion of the net magnetization $\vec{M}$ can be expressed as

$$\frac{d\vec{M}}{dt} = \vec{M} \times \gamma \vec{B}_0 \tag{2.11}$$

which describes how the rate of precession of the magnetization vector is proportional to the field. The angular velocity of the magnetization precessing around B_0 is called the Larmor frequency and is expressed as:

$$\omega_0 = \gamma B_0 \tag{2.12}$$

The application of a rotating rf field $\vec{B}_1$ applied perpendicular to $\vec{B}_0$ and at the same rate as the Larmor frequency, provides electromagnetic quanta (photons) equal in energy to the difference between two energy levels of the system. Such effect induces magnetic resonance transitions that allow for the manipulation and control of the dynamics of the magnetic moments.

To control the dynamics of the magnetic moments, a coil can be used to generate an oscillating field perpendicular to $\vec{B}_0\hat{z}$ of the form

$$\vec{B}_1 = 2B_1 \cos(\omega_{RF} t)\hat{y}, \tag{2.13}$$

that can be understood as the superposition of two circularly rotating magnetic fields with same frequency but in opposite directions in the x–y plane.

$$\vec{B}_{x\text{–}y} = \vec{B}_- + \vec{B}_+ \tag{2.14}$$

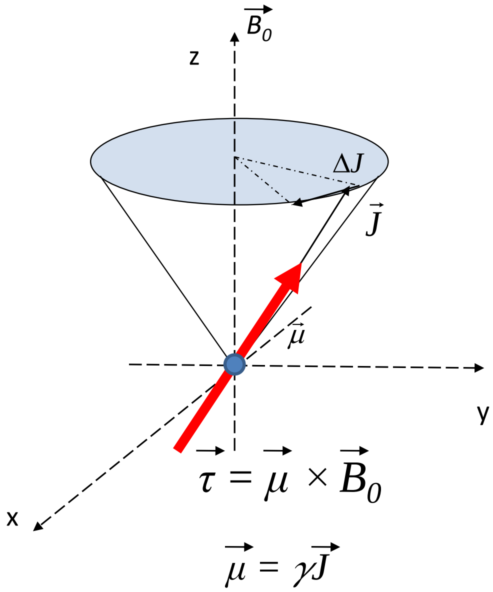

Figure 2.3: Precession of the magnetic moment around the magnetic field $B_0\hat{z}$ at the Larmor frequency. The magnetic moment experiences a change in direction of its angular momentum due to the non-alignment between the magnetic moment and the magnetic field.

where

$$\vec{B}_- = B_1(\cos(\omega_{RF}t)\hat{x} + \sin(\omega_{RF}t)\hat{y}) \tag{2.15}$$

$$\vec{B}_+ = B_1(\cos(\omega_{RF}t)\hat{x} - \sin(\omega_{RF}t)\hat{y}) \tag{2.16}$$

Of the two components, only the B_- rotates in the same direction as the precession of magnetic moments. Consequently only the left circularly polarized radiation, Equation (2.15), will be absorbed by the spins. The effect of adding $\vec{B_1}$ to the system changes the equation of motion (2.11) with the substitution of $\vec{B_0}$ for an effective field $\vec{B}_{eff}$:

$$\frac{d\vec{M}}{dt} = \vec{M} \times \gamma \vec{B_{eff}} \tag{2.17}$$

Transforming the system from the laboratory frame (x, y, z) to the rotating frame (x', y', z), $\vec{B_1}$ can be understood as a static vector in the (y') direction [5, 9] and the effective field can be expressed as

$$\vec{B}_{eff} = \left[\left(B_0 - \frac{\omega_{RF}}{\gamma} \right) \hat{z} + B_1 \hat{y'} \right]. \tag{2.18}$$

Here, $\dfrac{\omega_{RF}}{\gamma}$ represents a fictitious magnetic field that alters the value of B_{eff} in the z component. We will discuss the different techniques to alter or modify the effective magnetic field and the corresponding behavior of the magnetization in the next section.

2.5 Spin Manipulation Techniques

To start this section we need to keep in mind some statements [10]:

a. As long as the effective magnetic field and the magnetization are not parallel, a torque will be applied on the magnetization resulting in a change in the direction of the magnetization perpendicular to the field and the magnetization itself.

b. The angular velocity of the precession is proportional to the gyromagnetic ratio and to the magnitude of the effective magnetic field.

c. If the effective field and the magnetization are parallel, the magnetization will remain aligned with the field and will follow the effective field orientation if the change in direction is be slow enough to satisfy the adiabatic condition (section 3.3.1).

d. The effective magnetic field in the rotating frame can be modified by changing the magnitude of ω_{RF}.

Now that these statements have been specified, it can be seen that the two main methods used to manipulate the orientation of the spins are 1) sudden (rf pulses) or 2) gradual (adiabatic rapid passage ARP).

2.5.1 RF Pulse Manipulation

If an oscillating magnetic field as described in (2.13) is applied to the system, matching the Larmor frequency, $\omega_{RF} = \omega_0 = \gamma B_0$, the effective field described in (2.18) will become $\vec{B}_{eff} = B_1 \hat{y}'$. Since this effective magnetic field and the magnetization vector are perpendicular, then, as mentioned in statement a., a torque vector will force the magnetization to precess in the x'–z plane with frequency $\omega_1 = \gamma B_1$.

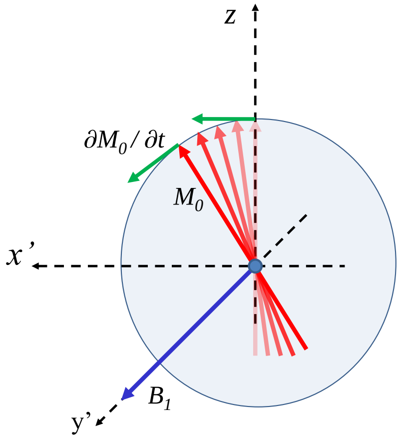

Figure 2.4: Manipulation of the direction of the magnetization using a RF pulse at the Larmor frequency.

The reorientation of the magnetization to a desired angle θ can be controlled by using rf pulses for a specific time length, since $\theta = \omega_1 t = \gamma B_1 t$. The most used rf pulses for spin manipulation are those of time lengths corresponding to rotations of $\frac{\pi}{2}$ and π radians. The pulse lengths corresponding commonlyto a specific angle can be described by:

$$t = \frac{\theta}{\gamma B_1} \tag{2.19}$$

where θ corresponds to the desired angle of orientation of the magnetization with respect to the positive z axis.

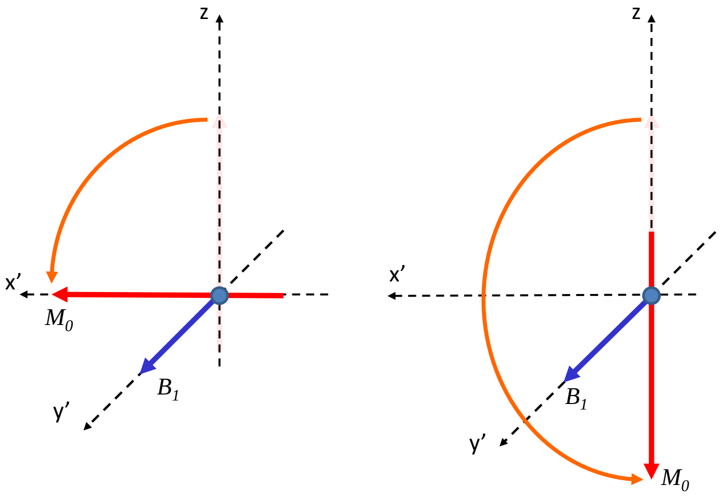

Figure 2.5: The pulse lengths control the final orientation of the magnetization. The figure on the left represents a $\pi/2$ pulse of length $t = (\pi/2)/\gamma B_1$ and the figure on the right represents a π pulse of length $t = \pi/\gamma B_1$

2.5.2 Adiabatic Rapid Passage

The effective field, $\vec{B}_{eff} = \left[\left(B_0 - \dfrac{\omega_{RF}}{\gamma}\right)\hat{z} + B_1\hat{y'}\right]$ shows that if the applied rf field oscillates around the Larmor frequency, then the z component of the effective field is not cancelled. The orientation of B_{eff} seen by the spins is determined by controlling the value of the frequency of B_1. The larger the difference between ω_{RF} and ω_0 the smaller the angle θ between the z axis and the B_{eff}.

Keeping the statements b. and c. of section (2.1.4) in mind, it can be noticed that if B_{eff} is close enough to the initial direction of the magnetization, that is, if $B_0 \gg \dfrac{\omega_{RF}}{\gamma}$ or $B_0 \ll \dfrac{\omega_{RF}}{\gamma}$, then the angle θ between B_{eff} and z is very small and the magnetic moments will align parallel to the new magnetic field. If the effective field changes in direction, for example, by changing ω_{RF} so that $\dfrac{\omega_{RF}}{\gamma}$ approaches B_0 slowly enough to satisfy the adiabatic condition (section 3.3.1), the magnetic moments will follow the direction of B_{eff}. The angle of orientation of the spins can be changed using this technique as can be seen in Figure 2.6 and the effect of π and $\frac{\pi}{2}$ pulses explained in the previous section can be replicated.

However, when the rf field is turned on, even when the frequency ω_{RF} is far from resonance, B_{eff} is not perfectly aligned with the z axis ($\theta \neq 0$). The statement a. in section (2.1.4) indicates that there will be a torque on the magnetization that will make it precess around B_{eff}. Figure 2.7 shows the angle θ as the determining factor in the amplitude of the precession of M around B_{eff}.

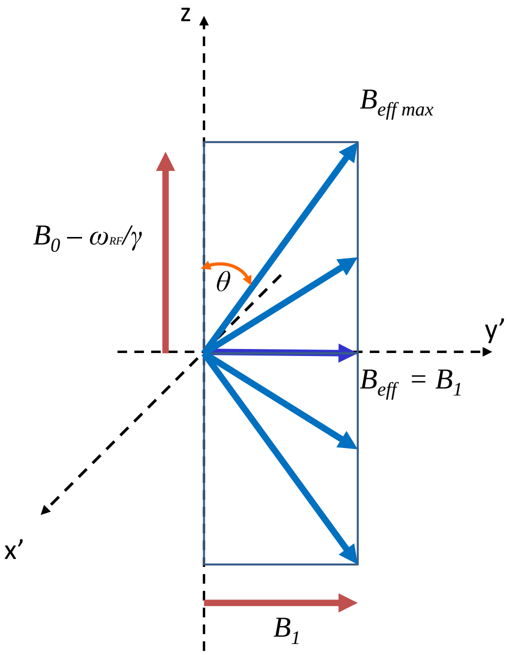

Figure 2.6: We can see the range in values of the magnitude of the effective field: from the maximum value $B_{eff_{max}}$ when θ is very small to the minimum value of the effective field $B_{eff_{min}} = B_1$ when $\theta = \frac{\pi}{2}$.

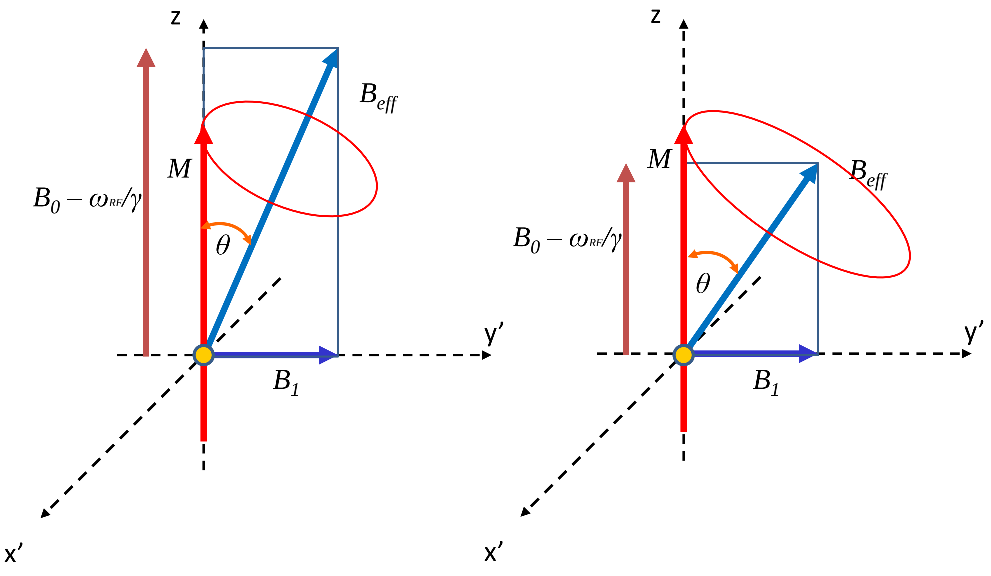

Figure 2.7: Angle of precession of the magnetization around the effective field for two different initial values of $B_0 - \omega/\gamma$ for the same B_1. The larger the difference $B_0 - \omega/\gamma$, the smaller the precession angle θ of the magnetization around B_{eff}.

If the adiabatic rapid passage technique is applied, θ, the angle between the magnetization and effective field, will remain constant while the angle between B_{eff} and the z axis is modified. The precession frequency, $\omega = \gamma B_{eff}$, will also change as the magnitude of the effective field varies. It is clear from this point that during this technique, $\theta = 0$ (or as small as possible) will be desired to make any possible effect of the magnetization precessing around the effective field as small as possible.

2.6 Relaxation Times and Bloch Equations

In earlier sections, the motion of non-interacting spins described by $\frac{d\vec{M}}{dt} = \vec{M} \times \vec{B}$ when a magnetic field is applied has been seen and the resulting precession of the magnetization has been described. However, the spins are not isolated from each other, so as a result they interact with its neighbors giving rise to mechanisms that contribute to spin relaxations.

2.6.1 Spin-Lattice Relaxation Time

In an equilibrium state between the magnetic moments of a sample and an external magnetic field $B_0\hat{z}$, the magnetization will be $M_z = M_0 = C\frac{B_0}{T}$. If this state is perturbed by an rf field $B_1\hat{y}'$ for a time equivalent to a $\pi/2$ pulse, the magnetization will then point in the $\hat{x}'$ direction. If the field is turned off and no other perturbation is produced, the moments will release the excess of energy to the lattice of the sample, relaxing back and aligning parallel to $B_0\hat{z}$.

Since this transition is not instantaneous, for most processes, the evo-

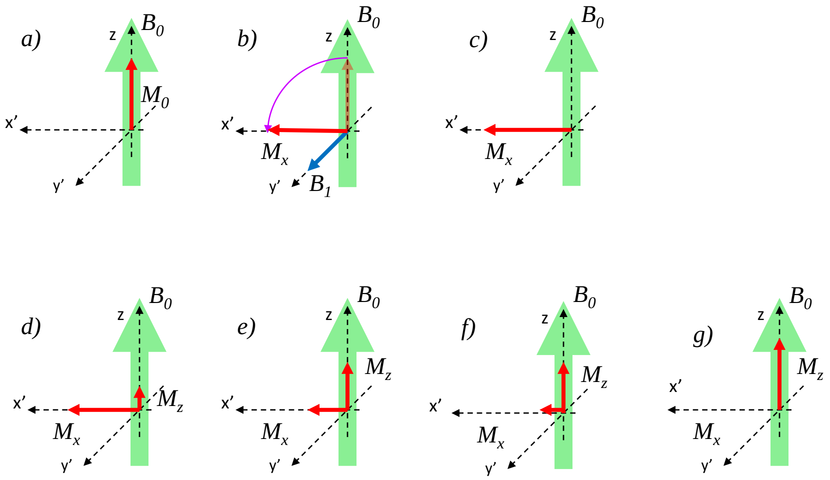

Figure 2.8: Magnetic manipulation sequence for observation of the spin-lattice relaxation. a) Saturated value of the magnetization M_0 due to the magnetic field $B_0\hat{z}$. b) The application of a $\pi/2$ pulse will orient the magnetization in the $\hat{x}'$ direction. c) Orientation of the magnetization $M_x = M_0$ in the $\hat{x}'$ direction. d), e), f) Recovery process of the magnetization M_z due to the release of excess of energy to the lattice. g) Final steady state of the magnetization $M_z = M_0$.

lution of M_z can be expressed as a function of a time constant T_1:

$$M_z = M_0 \left(1 - e^{-(t/T_1)}\right). \tag{2.20}$$

The time constant T_1 is called the spin-lattice or longitudinal relaxation time constant and it is an indicator of the mechanisms used by the spins to release energy to the lattice. Some major examples of spin-lattice interactions are modulated magnetic dipole-dipole interactions, magnetic nuclei-electron interactions and nuclear electric quadrupole interactions, and each one of these mechanisms has a different contribution to the value of the relaxation time [5, 10].

2.6.2 Spin-Lattice Relaxation Time in the Rotating Frame

As in the case of T_1, if an rf field $B_1\hat{y}'$, is applied for a time $\pi/2$, the magnetization will be $M_z = 0$ and $M_x = M_0$ perpendicular to B_1. In the previous section we turned off the magnetic field and let the magnetization relax back to the z axis parallel to B_0. Now, instead, we simultaneously turn off B_1 and turn on B_1 with a 90^o phase with respect to the original pulse. This makes $B_1 x'$ parallel to the magnetization of the system M_x

It was seen that for the spin-lattice relaxation time case, Figure 2.8, after the $\pi/2$ pulse, the effective field becomes $\vec{B}_{eff} = B_0\hat{z}'$. Now in the case of the spin-lattice relaxation time in the rotating frame, Figure 2.9, the effective field becomes $\vec{B}_{eff} = B_1\hat{x}'$, parallel to the magnetization M_x. Because the magnetic field B_1 is still on the difference between energy levels is smaller, in

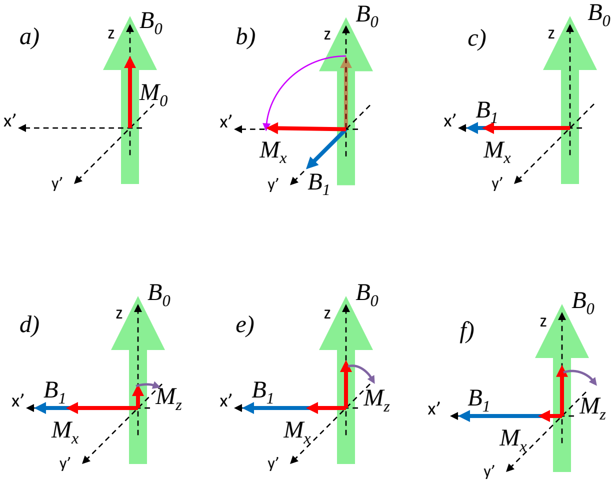

Figure 2.9: Magnetic manipulation sequence for observation of the Spin-Lattice relaxation in the rotating frame. a) Saturated value of the magnetization M_0 due to the magnetic field $B_0\hat{z}$. b) Application of a $\pi/2$ pulse to orient the magnetization in the $\hat{x}'$ direction. c) Application of a RF pulse in the $\hat{x}'$ direction parallel to the orientation of the magnetization $M_x = M_0$. d), e) Recovery process of the magnetization to the new energy state by releasing the excess of energy to the Lattice. f) Final steady state of the magnetization M_x in equilibrium with B_1.

equilibrium, ($M_{x0} = C\frac{B_1}{T}$ versus $M_0 = C\frac{B_0}{T}$), and relaxation to the smaller equilibrium value occurs. The exponential time constant, now different from T_1, is expressed as a function of a different time constant $T_{1\rho}$, such that

$$M_x = M_{x0} + (M_0 - M_{x0})\, e^{-(t/T_{1\rho})} \tag{2.21}$$

or since $B_1 \ll B_0$,

$$M_x \approx M_0 e^{-(t/T_{1\rho})} \tag{2.22}$$

that is, the magnetization decays nearly to zero.

2.6.3 Free Induction Decay (FID) of the Magnetization in the *x'-y'* Plane

As mentioned in the spin-lattice relaxation time section, after a $\pi/2$ pulse the magnetization that is pointing along the x' axis will decay with time due to the relaxation process and the magnetization will grow in the z axis. But there is another, usually faster process involved in the decay of the magnetization in the $x' - y'$ plane. The magnetic field induces the nuclei to precess, at the Larmor frequency, around it. If there is some magnetic field inhomogeneity inside the sample, different nuclei will feel different fields, so they will precess at different frequencies around the z axis. Consequently, if the magnetization has been oriented in the $x' - y'$ plane, the spins will precess at different angular velocities. The result is a de-phasing process in which the

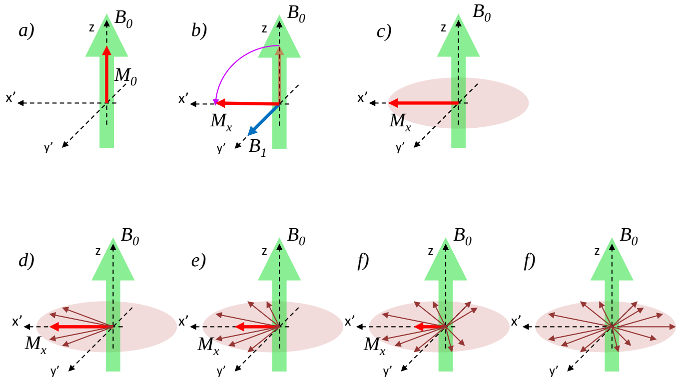

Figure 2.10: Magnetic manipulation sequence for free induction decay (FID) observation in the rotating frame. a) Saturated value of the magnetization M_0 due to the magnetic field $B_0\hat{z}$. b) Application of a $\pi/2$ pulse to orient the magnetization in the $\hat{x}'$ direction. c) Orientation of the magnetization $M_x = M_0$ in the $\hat{x}'$ direction. d), e), f) De-phasing process of the magnetization due to the inhomogeneity of the magnetic field in the sample. g) The magnetization is completely destroyed since the magnetic moments cancel each others.

magnetization spreads until the magnetic moments cancel each others and the net magnetization is zero.

We define the characteristic relaxation time T_2^* as the time constant which describes the decay of the magnetization contained in the $x' - y'$ plane. Therefore, T_2^* indicates the de-phasing rate in the $x' - y'$ plane, a process also called the free induction decay (FID) of the magnetic moments and described by the equation

$$M_x = M_0 e^{-t/T_2^*}. \tag{2.23}$$

.

Sometimes the shape decay approximates a gaussian more than an exponential

$$M_z = M_0 e^{-t^2/2T_2^{*2}}. \tag{2.24}$$

2.6.4 Spin-Spin Relaxation Time

If we are interested in the relaxation time of the spins due to the local dipole-dipole interactions between isochromats [1] spins, first it is necessary to minimize the decay effect produced by the inhomogeneity of the magnetic field. The relaxation time that describes the dipole-dipole interactions is called T_2, or the spin-spin relaxation time.

We can express the total contribution of both rates T_2 and T_2^* as

$$\frac{1}{T_2^*} = \frac{1}{T_2} + \frac{\gamma \Delta B_0}{2}. \tag{2.25}$$

If we wait long enough after a $\pi/2$ pulse for the magnetic moments to de-phase due to the inhomogeneity of the magnetic field inside the sample and to the spin-spin interactions between the local spins, the net magnetization in the $x' - y'$ plane will be zero. If a second pulse of length π is applied, the magnetic moments will be forced to rotate about the y' axis. This process inverts the relative position of the spins with respect to each other so that

---

[1] Understanding isochromatas spins as, spins which energy difference between the levels up and down, is exactly the same.

now the magnetic moments that precess slower are ahead of the faster ones. A re-phasing process called a spin-echo takes place at a time t from the π pulse, equal to the time between the $\pi/2$ and the π pulses.

An interesting part of this re-constructive sequence is that at the peak of the spin-echo, the de-phasing effect due to the inhomogeneity of the magnetic field is cancelled and only the effects of the spin-spin interaction remain active. The longer the time between the $\pi/2$ and π pulses the larger the net decay due to dipole-dipole interactions, and the lower the magnitude of the spin-echo.

Since T_2 is measured by observing the magnetization at the peak of the echo for different time between pulses, the spin-spin interaction will be a function of $2t$ and it can be expressed as:

$$M_x(2t) = M_0 e^{-2t/T_2}. \tag{2.26}$$

2.6.5 Bloch Equation

As we have seen, when the nuclei interact with their neighbors, the different interaction processes will each contribute in a different manner to the dynamics of the spins. Consequently, the equations of motion must include time evolution terms that describe these effects. Bloch's solution for the spin-lattice and the spin-spin relaxation times that considers the time evolution of the magnetization are:

$$\frac{dM_z}{dt} = \gamma \left(\vec{M} \times \vec{B} \right)_z + \frac{M_0 - M_z}{T_1} \tag{2.27}$$

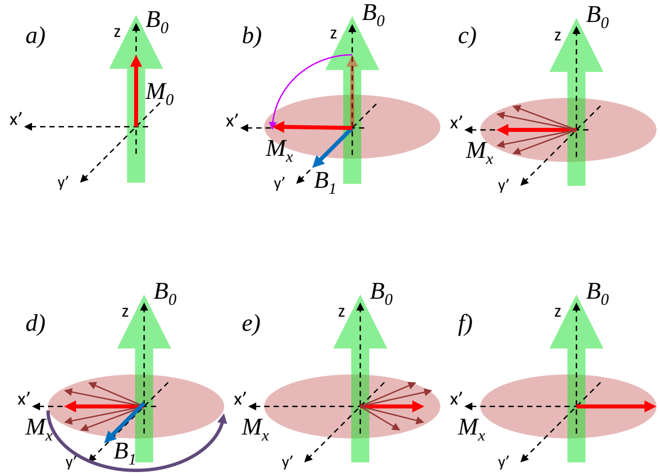

Figure 2.11: Magnetic manipulation sequence for observation of a spin-echo. a) Saturated value of the magnetization M_0 due to the magnetic field $B_0\hat{z}$. b) Application of a $\pi/2$ pulse to orient the magnetization in the $\hat{x}'$ direction. c) Orientation of the magnetization $M_x = M_0$ in the $\hat{x}'$ direction and dephasing of the spins. d) Application of a π pulse to invert the system with respect to the y' axis. e) Re-phasing process of the magnetization due to the inhomogeneity of the magnetic field in the sample. f) The magnetization is completely coherent in the $x' - y'$ plane, causing a spin echo.

$$\frac{dM_x}{dt} = \gamma \left(\vec{M} \times \vec{B} \right)_x + \frac{M_x}{T_2} \tag{2.28}$$

$$\frac{dM_y}{dt} = \gamma \left(\vec{M} \times \vec{B} \right)_y + \frac{M_y}{T_2} \tag{2.29}$$

Other interaction mechanisms will not be discussed here, but a deeper explanation of the modification of the Bloch equations when other relaxation times need to be included can be found in *Principles of Magnetic Resonance*, by C.P. Slichter.

Chapter 3

Detecting and Manipulation of Spins in Nuclear Magnetic Resonance Force Microscopy

In the previous chapter we examined the main techniques used to manipulate the nuclear magnetization. We explained how interactions with nuclei induce the relaxation of the nuclear magnetization and indicated the characteristic relaxation times. The goal of this chapter is to present the theory behind the force-detection techniques used to measure the magnetization and interactions of the nuclei contained in a micrometer size sample.

3.1 Force Detection of Magnetic Resonance

In 1991, John Sidles proposed a more sensitive method of detecting magnetic signals than the inductive detection techniques of conventional NMR and MRI [1, 20]. The proposed technique consists of a magnetized sample and a gradient magnet used to induce a periodic magnetic force, acting on a cantilever [11, 12]:

$$\vec{F}(t) = (\vec{M}(t) \cdot \vec{\nabla})\vec{B}. \tag{3.1}$$

Newton's third law predicts that there is no difference between attaching the sample on the cantilever while the gradient magnet is kept still, as in Figure 3.1, and attaching the magnet on the cantilever while the sample's position is fixed. However, the advantages of sample-on-cantilever configuration will be discussed when we address noise effects in subsequent chapters.

Since the force generated by the nuclei is very small, it is necessary to couple to the magnetic force at the cantilever's resonance frequency. By doing so the cantilever response to a force is

$$A = Q\frac{F}{k}. \tag{3.2}$$

It can be seen that the response amplitude of oscillation, A, due to the periodically driven force of amplitude F is increased by the value of the quality factor Q (compared to a static restoring force) and is inversely proportional to the spring constant k.

The basic configuration of our MRFM experiment is shown in Figure 3.1, representing a sample-on-cantilever geometry. The large magnetic field $\vec{B}_0 = (B_{field} + B_{PM})\hat{z}$ magnetizes the sample spins and the gradient permanent magnet (PM) generates an inhomogeneous magnetic field which induces a magnetic force. An rf coil generates the magnetic field $\vec{B}_1 = B_1\hat{y'}$, perpendicular to $\vec{B}_0$, that modulates the spins at the resonance frequency of the cantilever. This modulation causes spin flips along the $z - y'$ plane needed for the adiabatic rapid passage technique. The modulated magnetic force produces an amplitude response of the cantilever observed using laser interferometry.

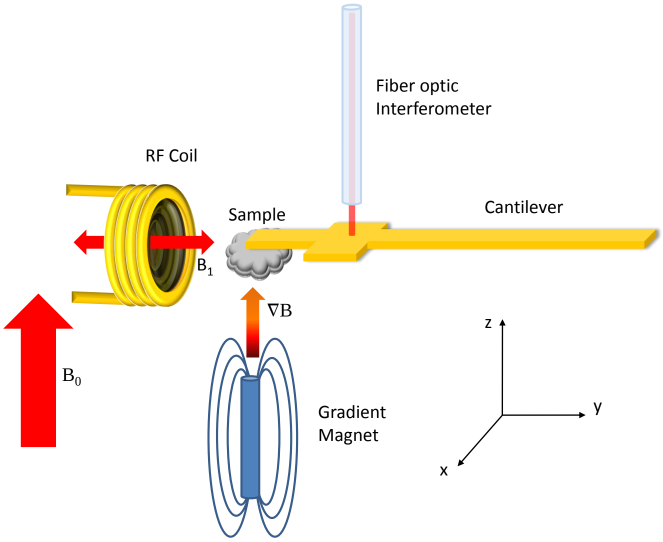

Figure 3.1: A Magnetic Resonance Force Microscopy (MRFM) setup. This sketch shows the sample-on-oscillator configuration.

3.1.1 Magnetization

In subsequent paragraphs and sections, the conservation of the magnetization and efficiency of the frequency and amplitude modulations will be discussed. The magnitude of the equilibrium magnetization, as described by Equation (2.9), is a function of temperature and external magnetic field. When $\dfrac{\mu B}{k_B T} \ll 1$, the magnetization can be expressed as [8]

$$M_0 = \frac{N\gamma^2\hbar^2 I(I+1)}{3k_B T} B_0 \tag{3.3}$$

In order to increase the magnetic force $\vec{F}(t) = (\vec{M}(t) \cdot \vec{\nabla})\vec{B}$, low temperature and high magnetic fields are necessary to maximize the magnitude of the magnetization M_0. This magnitude must also be effectively conserved during the modulation protocol, and the quantity $\vec{M}(t) \cdot \vec{\nabla}\vec{B}$ must be maximized by controlling the magnetic field $\vec{B}_{eff}$.

The effective field $\vec{B}_{eff} = \left[\left(B_0 - \frac{\omega_{RF}}{\gamma}\right)\hat{z} + B_1\hat{y'}\right]$ is controlled by modifying the frequency and/or amplitude of the rf field. However the component along the z axis will be directly proportional to the difference between the Larmor frequency ω_0 and ω_{RF}. Defining $\omega_{RF} = \omega_0 - \Omega$ we can express the effective magnetic field as:

$$\vec{B}_{eff} = \left[\left(B_0 - \frac{\omega_0}{\gamma} + \frac{\Omega}{\gamma}\right)\hat{z} + B_1\hat{y'}\right] \tag{3.4}$$

When $\omega_{RF} = \omega_0$, the term Ω is zero and the z component of B_{eff} is also zero. On the other hand, the maximum value of the effective field is given by

$$\vec{B}_{eff_{max}} = \frac{\Omega}{\gamma}\hat{z} + B_1\hat{y}' \tag{3.5}$$

wich also corresponds to the maximum value of the z component.

During the inversion process the magnitude of the effective field changes in a range between $\sqrt{(\frac{\Omega}{\gamma}\cos(\omega_c t))^2 + B_1^2}$ and B_1. Since neither of these values makes B_{eff} much bigger than B_0, the spins will relax back to the z direction. However, because the magnitude of the effective field varies while ramping the rf field, the relaxation time will also change as a function of the different magnitudes of the effective fields. Because of this effect, the manipulation of the spins should be performed in a time shorter than the combination of all the $T_{1\rho}$; essentially, before the total magnetization is lost.

3.1.2 Gradient of the Magnetic Field

Figure 3.2 shows the contribution of a permanent magnet to the magnitude of the magnetic field. By adding a large field gradient a spatial dependency of the magnetic field, $\vec{B}_0 = (B_{field} + B_{PM})\hat{z}$ is introduced in the system. If B_0 is inhomogeneous inside a sample there will be a different Larmor frequency for each different value of the magnetic field as shown in Figure 3.2 bottom left. A simulation of the magnetic field along the z axis for a cylindrical permalloy wire of radius 0.2 mm and length 10 mm is shown in Figure 3.2 top left graph.

The resonance slice, Δz, is defined as the section in which, despite the inhomogeneity of the magnetic field induced by the gradient magnet, the magnetic moments can be manipulated as a whole system. This definition can be expressed as

$$\Delta z = \frac{2\Omega/\gamma}{\nabla_z B}, \tag{3.6}$$

where $2\Omega/\gamma$, the range between $B_0 - \omega_{RF}/\gamma$ and $-(B_0 - \omega_{RF}/\gamma)$ when $\omega_{RF} = \omega_0 - \Omega$ shown in Figure 2.6, describes the range in which the spins feel almost the same effective magnetic field $\Delta B = \dfrac{\Delta\omega}{\gamma} = \dfrac{2\Omega}{\gamma}$, and $\nabla_z B$ is the gradient of the magnetic field relative to position. Figure 3.3 shows the resonance slice thickness at a given position as a function of the amplitude $\dfrac{\Omega}{\gamma}$.

The field gradient is responsible in part for the magnitude of the magnetic force $F = M(\partial B/\partial z)$ and the spatial resolution. As long as the resonance slice Δz is larger than the sample, larger magnetic field gradients will increase

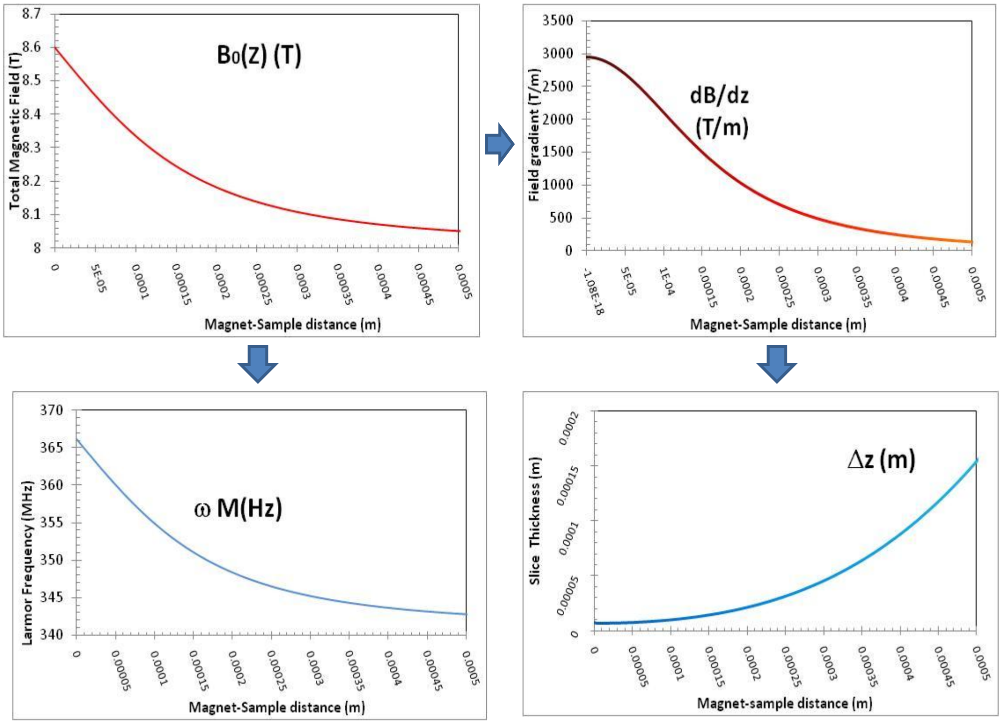

Figure 3.2: Clockwise from the top left, total magnetic field $\vec{B}_0 = (B_{field} + B_{PM})\hat{z}$ generated by a cylindrical permanent magnet at different magnet-sample distances along the z axis. Gradient of the magnetic field behaviour for same permanent magnet and space interval. Resonance slice, Equation (3.6) describes the change in thickness as a function of magnet-sample distance. Finally, representation of the Larmor frequency of the spins proportional to the magnetic field as a function of magnet-sample distance.

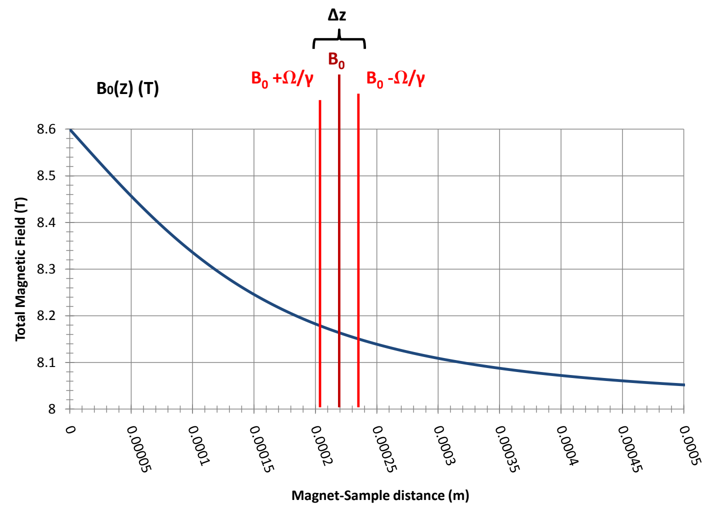

Figure 3.3: The magnetic field $\vec{B_0} = (B_{field} + B_{PM})\hat{z}$ and the resonance slice Δz where the N spins inside the resonance slice, Δz, feel the "same" field.

the magnitude of the magnetic force. In the case where Δz is smaller than the thickness of the sample, larger gradient magnets involve shorter resonance slices with a smaller number of spins N within them to induce the magnetic force. As a result, it is clear that increasing the gradient does not always generate larger forces [13].

Using Equations (3.1) and (3.3) and substituting $N = n \cdot V = n \cdot (A\Delta z)$ and $\nabla_z B = 2\Omega/(\gamma\Delta z)$, it can be seen that for Δz smaller than the sample, the force becomes independent of the gradient of the magnetic field and linearly proportional to γ, A and Ω:

$$F = n 2\Omega A \frac{\gamma \hbar^2 I(I+1)}{3k_B T} B_0 \tag{3.7}$$

Figure 3.2 (top right) shows how, for different positions with respect to the permanent magnet, there are different values of the magnetic field gradient as a consequence the respective resonance slice thickness will also be different. It can also be seen that, in order to achieve the highest resolution possible (thinnest resonance slice), the sample-magnet distance must be as short as possible.

3.2 Mechanical Oscillator

The cantilever is an essential part of a NMRFM experiment. Owing to its sensitivity, it is able to detect extremely small forces generated by the spin-magnet interaction. One of the advantages of using a cantilever is that it can be treated as a simple damped harmonic oscillator driven with a periodic force. This is the case when the modulated magnetic force matches the cantilever's resonance frequency [22, 34].

The equation of motion that describes the oscillation of the cantilever as a damped driven harmonic oscillator is:

$$m\frac{d^2z}{dt^2} + \Gamma\frac{dz}{dt} + kz = F_0\cos\left(\omega_c t\right) \tag{3.8}$$

where z is the position of the tip, m is the effective mass of the cantilever, k is the spring constant and $\Gamma = \dfrac{k}{\omega_c Q}$ characterizes the energy dissipation of the cantilever. On the right side of the equation, the driven term is composed of the amplitude of the force F_0 that is modulated to oscillate at the resonance frequency of the cantilever, $\omega_c = 2\pi f_c = \sqrt{k/m}$. The cantilever's response time to a perturbing force is described by $\tau_c = 2Q/\omega_c$ after which it approaches a steady state. It can be seen that oscillators with a large ω_c will have a fast response time to perturbations, while large Q oscillators have a slow response.

The performance of the cantilever is characterized by the minimum detectable force which is ultimately limited by the thermal noise of the cantilever and it is given by [22, 34]

$$F_{min} = \sqrt{S_f \Delta\nu} = \sqrt{\frac{4kk_B T \Delta\nu}{\omega_c Q}}. \tag{3.9}$$

Consequently the ideal cantilever with very high sensitivity $A = Q\dfrac{F}{k}$ to an external force, F, and very low thermal noise must have very low k, and very high Q and ω_c. At the same time, low temperatures increase the sample magnetization and decrease the thermal noise of the cantilever contributing to an improvement in the sensitivity of the measurements.

3.3 Magnetic Modulation

The magnetic force generated by the sample spins is so small that it must be coupled to the resonance frequency of the cantilever to increase the response by a factor of Q as described by Equation (3.2). At the same time, the amplitude of the modulation contributes to the size of resonance slice, to the magnitude of the z component of the oscillated magnetization, and to the magnitude of the force generated by the sample. The protocol used to modulate the magnetization will play a crucial part in the sensitivity of the measurements.

3.3.1 Cyclic Adiabatic Inversion (CAI)

This technique is based on the implementation of periodic adiabatic rapid passages that cyclicly invert the spins at the resonance frequency of the mechanical oscillator.

To start the cyclic adiabatic inversion sequence, it is necessary to make B_{eff} and B_0 parallel to grab as many spins as possible and also to make the angle of precession

$$\cos\theta_{eff} = \frac{B_{eff}\hat{z}}{B_{eff}} = \frac{M_z}{M_0} = \frac{\frac{\Omega}{\gamma}\cos(\omega_c t)}{\sqrt{(\frac{\Omega}{\gamma}\cos(\omega_c t))^2 + B_1^2}} \tag{3.10}$$

as small as possible. Figure 3.4 and Equation 3.10 show that this can be achieved by setting the frequency of the rf field as far as possible from the Larmor frequency without having to reduce the amplitude to zero.

Once B_0 and B_{eff} are parallel, we bring the magnetic field to the $x' - y'$ plane by tuning ω_{RF} to ω_0. Then, a frequency-modulated wave of the form

$$\omega_{RF} = \omega_0 + \Delta\omega_{RF}(t) \tag{3.11}$$

can be generated to oscillate the z component of the magnetization.

For the case of a sinusoidal modulation with the same frequency as the mechanical oscillator, this turning can be expressed as

$$\omega_{RF} = \omega_0 + \Omega\cos(\omega_c t). \tag{3.12}$$

Therefore, the effective field will be given by

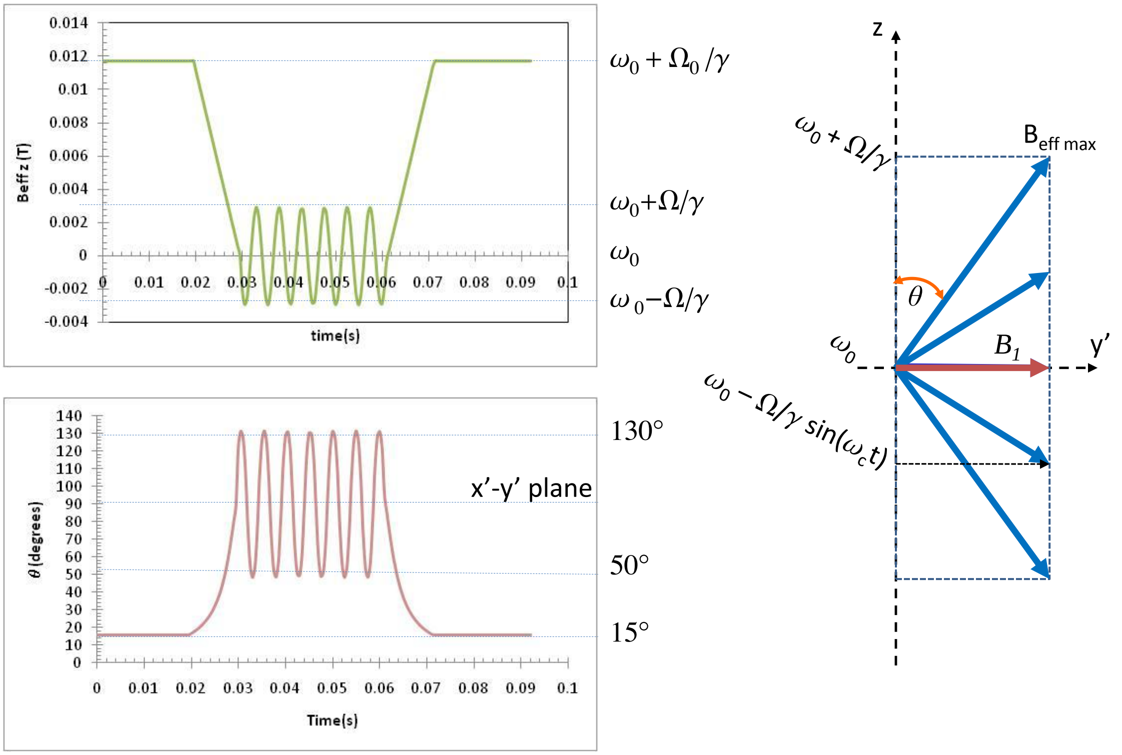

Figure 3.4: Cyclic adiabatic inversion protocol. The top left figure represents the values of the effective field component parallel to B_0 during the modulation protocol. Figure bottom left represents the angle between B_{eff} and B_0 z during the same protocol. Right figure is representation of the vector $\vec{B}_{eff}$ orientations during inversion.

$$\vec{B}_{eff} = \left[\left(B_0 - \frac{\omega_0 + \Omega\cos(\omega_c t)}{\gamma} \right) \hat{z} + B_1 \hat{y'} \right], \tag{3.13}$$

and as a result the z component of the magnetization during the cyclic adiabatic inversion will be:

$$M_z(t) = M_0 \cos(\theta_{eff}(t)) = M_0 \cdot \frac{\frac{\Omega}{\gamma}\cos(\omega_c t)}{\sqrt{(\frac{\Omega}{\gamma}\cos(\omega_c t))^2 + B_1^2}}. \tag{3.14}$$

The protocol shown in Figure 3.4, ends by setting the rf field far from the Larmor frequency to ensure that the magnetization ends pointing in the same direction as B_0 or with the smallest angle θ possible.

During cyclic adiabatic inversion, Equation 3.14 is an indication of how much of the total magnetization is effectively used to generate the force that will drive the cantilever [14]. It can be seen that the maximum value of the z component of the magnetization depends on $\frac{\Omega}{\gamma B_1}$. Figure 3.5 shows the ratio between the total magnetization due to the external magnetic field and the effective magnetization responsible for generating the magnetic force. For the cases where $\frac{\Omega}{\gamma}$ is large compared to B_1, $M_z(t)_{max}$ reaches values close to M_0, so the magnetic force is maximum.

In principle it is always desirable to keep the ratio $\frac{\Omega}{\gamma B_1}$ as large as possible so that the induced magnetic force is maximized. However, this maximization is possible only if the change in direction of the effective field is performed slowly enough to keep the spins locked to B_{eff}. Hence, an adiabatic condition arises requiring that the Larmor precession frequency be greater than the

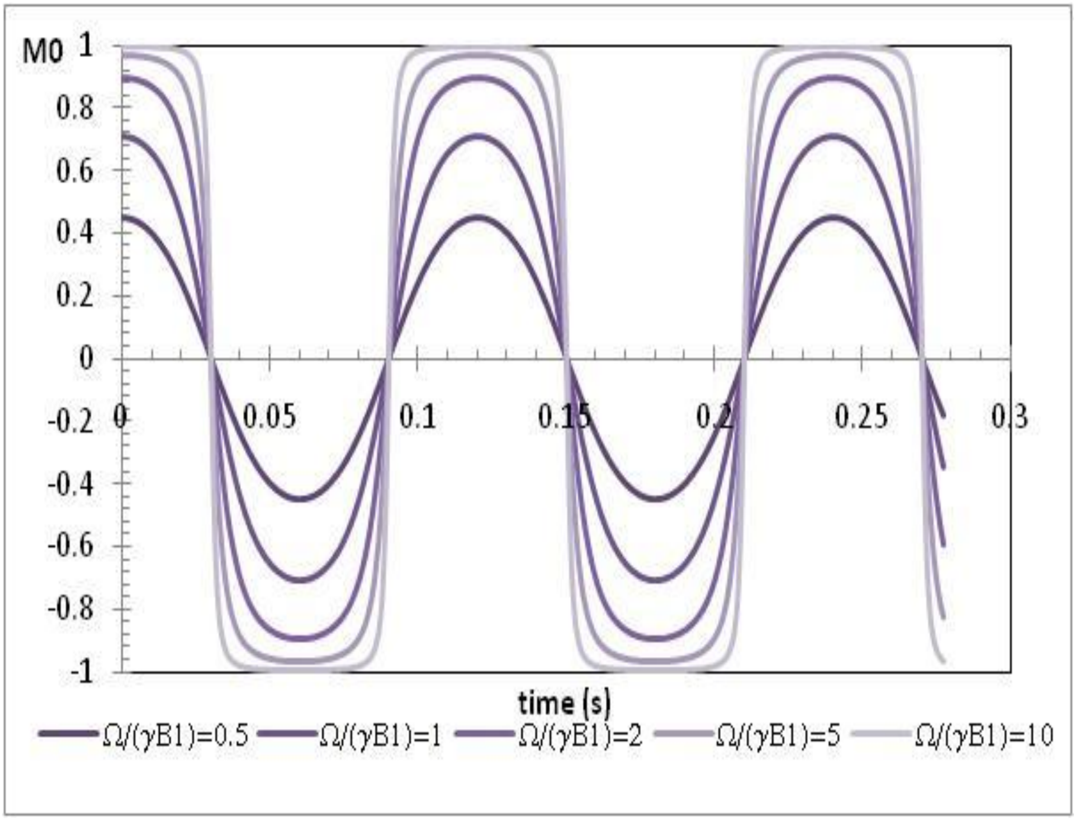

Figure 3.5: Representation of the $M_z(t)/M_0$ expression, Equation (3.14), for different values of $\dfrac{\Omega}{\gamma B_1}$.

angular frequency due to the change in effective field. This statement can be expressed as:

$$\gamma B_{eff_{min}} \gg \frac{d\phi}{dt} |_{max} \tag{3.15}$$

The angular velocity of B_{eff} is described by $\dfrac{d\phi}{dt}$. Here $\phi = (\frac{\pi}{2} - \theta)$, and can be expressed as:

$$\tan\phi = \frac{B_{eff}\hat{z}}{B_{eff}\hat{y}'} = \frac{\Omega}{\gamma B_1}\cos(\omega_c t). \tag{3.16}$$

A simple calculation shows that the angular velocity of the effective field can be expressed as:

$$\frac{d\phi}{dt} = \frac{\dfrac{\omega_c \cdot \Omega}{\gamma B_1}\sin(\omega_c t)}{\left(\dfrac{\Omega}{\gamma B_1}\cos(\omega_c t)\right)^2 + 1}. \tag{3.17}$$

The maximum value of the angular velocity is achieved when B_{eff} passes through resonance, leaving $\dfrac{d\phi}{dt}_{max} = \dfrac{\omega_c \cdot \Omega}{\gamma B_1}$. It is also shown that the larger the ratio $\dfrac{\Omega}{\gamma B_1}$, the larger the maximum angular velocity of the effective field.

Since the minimum value of the Larmor frequency happens when $B_{eff_{min}} = B_1$, the cyclic adiabatic condition can be expressed as

$$\gamma B_1 \gg \frac{\omega_c \cdot \Omega}{\gamma B_1} \tag{3.18}$$

and this can be rearranged to give

$$\frac{(\gamma B_1)^2}{\omega_c \Omega} \gg 1. \tag{3.19}$$

This **adiabatic condition** (Equation 3.19) presents a huge constraint in the future challenges to achieve single nuclear atomic resolution. It can be seen that in principle, a large numerator and small denominator will help to ensure that the spins responsible for the intensity of the magnetization are not lost due to non-adiabatic effects during the modulation of the force and, to achieve condition (3.19), Ω and ω_c must be sufficiently small.

However, it is necessary that the magnitude of the force $F(t) = M_z(t) \cdot \frac{\partial B}{\partial z}$ be large enough to be detected by the cantilever. Equation 3.14 indicate that the maximum signal will be obtained when the ratio $M_z(t)/M_0 = \frac{\frac{\Omega}{\gamma}\cos(\omega_c t)}{\sqrt{(\frac{\Omega}{\gamma}\cos(\omega_c t))^2 + B_1^2}} \simeq 1$. In other words, Ω must be at least 6 times larger than γB_1 as shown in Figure 3.5. Equation 3.19 indicates that the cantilever's resonance frequency must be small. Mechanical resonators with low resonance frequencies are generally large and fragile with long ring up times, ($\tau_c = 2Q/\omega_c$, as seen in section 3.2); also a small ω_c increases the threshold of the minimum detectable force as indicated by Equation 3.9, and because of this the sensitivity of the cantilever is also reduced. Since the numerator in Equation 3.19 must be large, but γ is an intrinsic property of the nuclei and not can be modified, large B_1 fields are desirable. However, large rf fields decrease the ratio $M_z(t)/M_0$, reducing the effectiveness of the magnetic force; they also can cause heating.

The result of those factors is that force sensitivity and the adiabatic condition are in some ways opposed to one another. The key to achieving the maximum resolution is to find the values that maximize the sensitivity and at the same time are within the boundaries that the cyclic adiabatic inversion stipulates. As an example, one technique is to use different shapes of modulation that follow the CAI constraint but allow the use of larger amplitudes of modulation. Figure 3.6 is an example that shows how triangular waves admit the use of larger Ω, while they conserve the adiabaticity during the inversions.

CAI with sinusoidal or triangular waveform has the advantage that the sample magnetization remains spin-locked during the modulation of the effective field and that the transition between inversions is continuous. But, even with the "ideal" experiment with very low ω_c, large B_1, γ and Ω there is still the inconvenience of signal artifacts due to rf fields producing spurious forces at the cantilever resonant frequency, ω_c. This effect and its causes will be demonstrated and explained below.

3.3.2 Sawtooth Modulation

Sawtooth modulation also locks the spins to the effective field during inversions, but the modulation waveform has twice the cantilever's resonance frequency ω_c, as seen in Figure 3.7. However, the force is still modulated at the resonance frequency of the cantilever. As a consequence, any artifact effect will appear at $2\omega_c$ and will not interfere with the force measurements.

The largest problem with the sawtooth wave is that there is a discontinuity between sweeps, as is shown in Figure 3.8. Consequently, if the magnetization precesses around B_{eff} with some angle $\theta \neq 0$, the angle of precession can increase with each inversion, decreasing the component of the

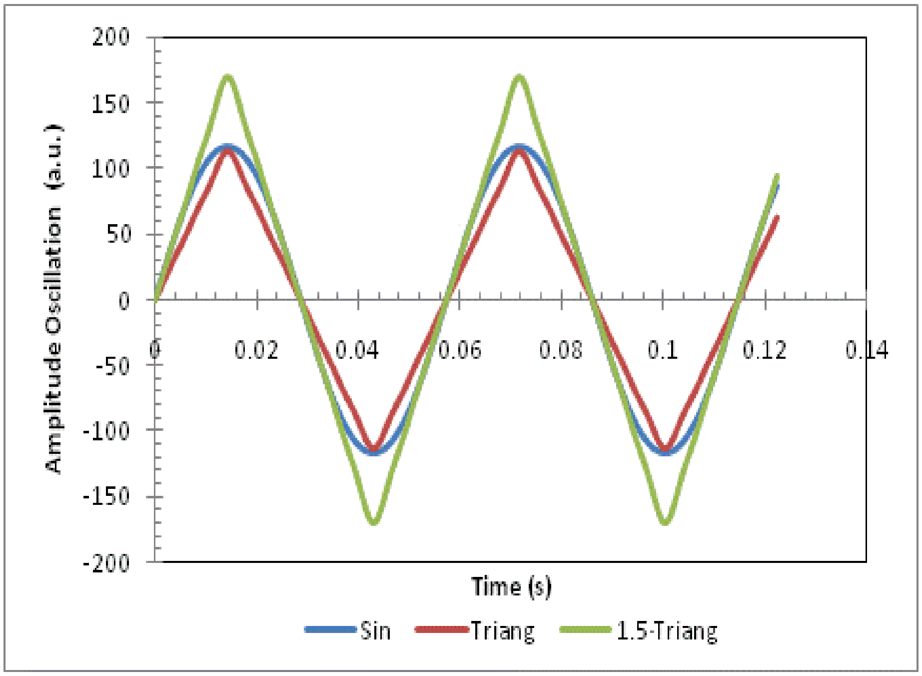

Figure 3.6: Three different modulation waves inside the CAI boundaries for $\gamma = 42.58$ MHz/T, $B_1 = 33$ Gauss and $\omega_c = 6.28$ kHz. The sinusoidal wave, blue, and triangular, red, have amplitude $\Omega = 500$ kHz. It can be seen that the triangular wave has a more shallow slope, or a smaller $\frac{d\phi}{dt}$, than the sinusoidal wave. On the other hand the third triangular wave has an amplitude modulation 1.5 times larger than the other two, but the same slope as the sinusoidal wave.

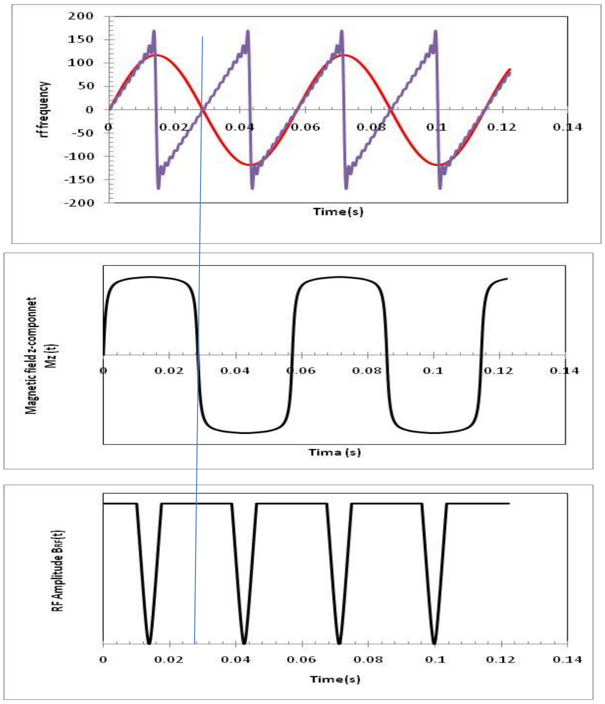

Figure 3.7: A sawtooth wave oscillates at double the resonance frequency of the sinusoidal and triangular wave and can use a larger Ω within the boundaries of the adiabatic condition. The diagram shows that the discontinuity between sweeps is fixed by bringing the amplitude of B_1 to zero to make $\theta = 0$ before each inversion and to avoid phase discontinuities in the spin-locking to the effective field.

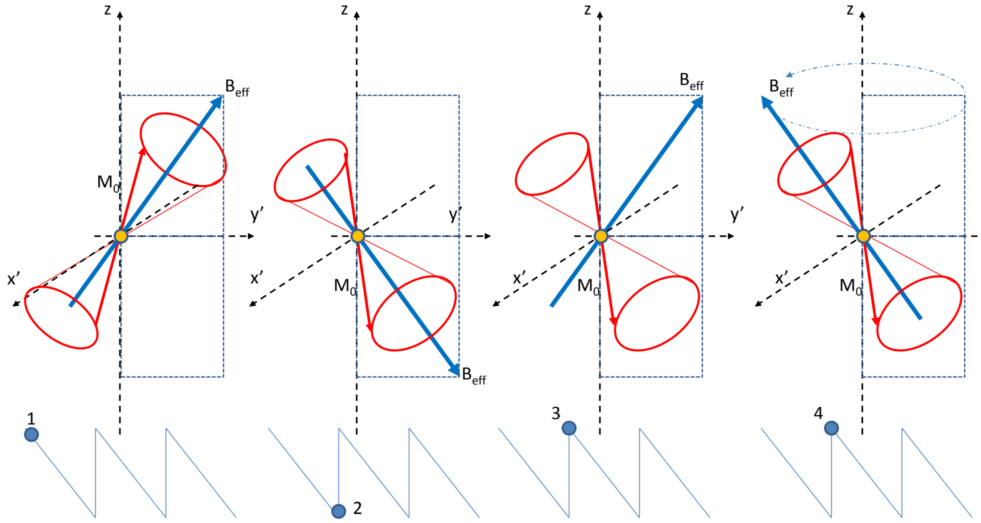

Figure 3.8: 1) When turning the RF field on, the magnetization will precess around B_{eff} with angle θ. Since the inversion is adiabatic, there is no loss of spins when the spins reach position (2). Because the process to go from (2) to (3) is instantaneous, the magnetic field "null cone" remains in the same orientation but B_{eff} is back now to its original position without having the spins locked to it. A 180° phase shift of the effective field with respect to the axis y' would align the effective field with the magnetization (4) allowing adiabatic rapid passage to be performed to flip the spins back to (1).

magnetization along the effective field. One solution to overcome this problem is to perform 180° phase changes in the B_1 field between each of the sweeps. The alternating phase (y'), $(-y')$, (y'), $(-y')$, ... technique will ensure that the magnetization vector $M_z(t)$ remains spin-locked to B_{eff}. A second solution is to ensure that the angle $\cos\theta_{eff} = \dfrac{B_{eff}\hat{z}}{B_{eff}} = \dfrac{M_z}{M_0}$ is zero at the beginning and end of the inversion, or in other words: $\vec{B}_{eff} = B_{eff}\hat{z}$ This condition can be accomplished synchronizing the rf modulation with amplitude modulation that gradually turns off B_1 when B_{eff} is close to $\hat{z}$ to assure that $\theta = 0$. Application of these techniques can be found at [15], [16], [17], [18], [19] and [20] where the case of field amplitude modulation can be seen implemented in Figure 3.7.

3.3.3 Cyclic Non-Adiabatic Inversion (CyNAI)

The Cyclic Adiabatic Inversion condition is very limiting when very high sensitivity is needed. We are studying the possibility of developing a novel method that can help us to overcome its constraints. The technique – Inversion of MAgnetization Non-adiabatically EmphaSized (IMANES) – is based on coupling the inversions of the spins with the cantilever resonance frequency by the application of π pulses.

The first protocol proposed to perform non-adiabatic inversions is shown in Figure 3.9, which explains the basic idea behind the process that can be used to invert the magnetization $M_z(t)$. By opening and closing the rf gate synchronized with the frequency of the cantilever, two π pulses will invert the

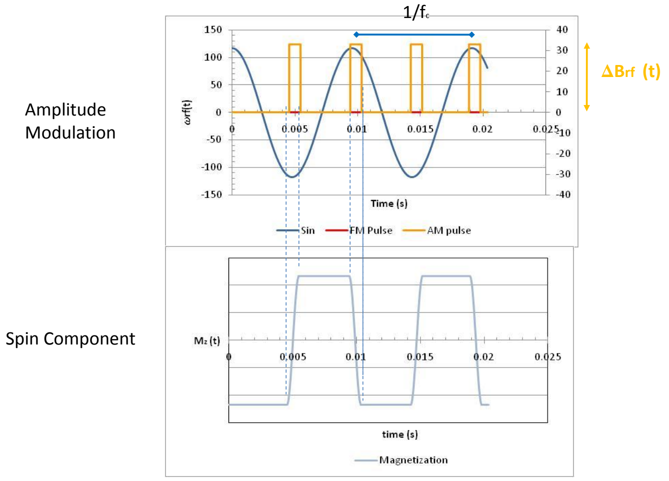

Figure 3.9: The application of π pulses are generated by turning ON and OFF the RF field amplitude and the frequency constant.

magnetization, coupling the magnetic force with the resonance frequency of the cantilever. In order to have a better control of the spin flips,a shift in phase by 180° between pulses is recommended.

We have developed a second possible protocol based on this technique, in which the application of a pulse at ω_0 of length $t_\pi = \dfrac{\pi}{\gamma B_1}$ inverts the direction of the magnetization. This orientation of the spins can be held fixed by keeping the rf field on with a 90° phase, far from resonance, at $\omega_{rf} = \omega_0 - \Omega/\gamma$. After a time $t_{hold\ down} = \dfrac{1/f_c - 2t_\pi}{2}$, a second pulse at frequency ω_0 and phase 180° (to correct for pulse imperfection) and of the same length t_π inverts the spins to their original position. The spins are held here by again keeping the rf field on at $\omega_{rf} = \omega_0 + \Omega/\gamma$ and phase 90° for a time $t_{hold\ up}$ of

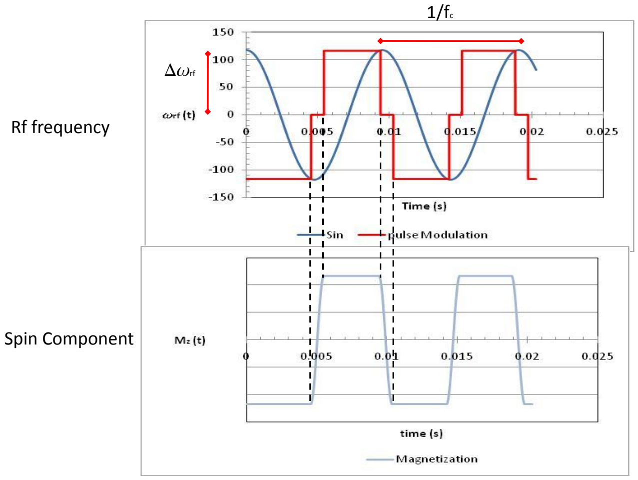

Figure 3.10: The application of π pulses at twice the resonance frequency of the cantilever modulates the force with frequency ω_c. The sinusoidal signal in the top graph is only for visual reference.

the same length as $t_{hold\ down}$. This protocol can now be repeated continuously, resulting in a modulation of the magnetization that matches the cantilever frequency ω_c.

The only condition that this pulse protocol needs to meet to work properly is that the Rabi frequency must be larger or the same as the cantilever's resonance frequency, $\omega_c \leq \omega_1 = \gamma B_1$. In other words, the spin flip must be faster than the time it takes for the cantilever to perform half a cycle. It has been observed that the rf artifact is zero when $\omega_c = \omega_1$ since modulation is not necessary and there is no change in the rf field.

For a typical sinusoidal CAI wave with this technique, for small B_1 or

γ, or large ω_c, the frequency modulation amplitude must be small to obey the adiabatic condition and, as a result, $M_{z_{max}}$ will be small. However, using this technique, we can maximize the amplitude thorough the modulation since the adiabatic condition is not necessary as long as $\omega_c \leq \omega_1$. Additionally, cantilevers with high resonance frequencies can be more beneficial since a large frequency does not affect the modulation amplitude, but decreases the ring-up time of the cantilever and reduces F_{min}.

We have developed a third possible protocol based on this technique, shown in Figure 3.11. In this case, we first invert the magnetization M_z that is aligned with $\vec{B_0}$ by turning on the rf field with frequency ω_0 for a time $t_\pi = \dfrac{\pi}{\gamma B_1}$. After t_π, the amplitude remains unchanged but to keep the spins in this orientation, we set the rf frequency far from resonance ($\omega_{rf} = \omega_0 - \Omega/\gamma$) with a 90^0 phase for a time $t_{hold\ down} = \dfrac{1/f_c - 2t_\pi}{2}$. Now we apply a second π pulse, with 180^0 phase, that inverts the spins back to their original alignment with B_0 for a time $t_\pi = \dfrac{\pi}{\gamma B_1}$. Here, unlike the earlier protocol, the frequency remains constant and it is the amplitude that is changed by turning it off for a time $t_{rf\ off} = t_{hold\ down}$. For this period of time, $B_{eff} = B_0$ and $M_0 = M_z(t)$. Again, to repeat the inversion after $t_{rf\ off}$ we turn on the rf field at ω_0 and after a time t_π, we jump to $\omega_{rf} = \omega_0 - \Omega/\gamma$.

The same condition seen in the first pulse protocol, $\omega_c \leq \omega_1$, must be met for this protocol however, in this case neither frequency modulation nor amplitude modulation follow the oscillation pattern of the cantilever.

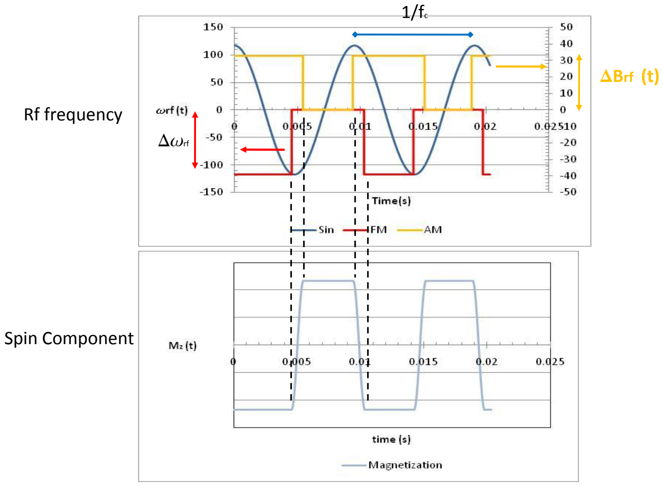

Figure 3.11: The application of π pulses synchronized with the resonance frequency of the cantilever modulates the force with frequency ω_c. In this case, B_{rf} is turned on and off.

3.3.3.1 Resonance Slice in IMANES

With adiabatic rapid passage, it is possible to invert the spins contained in a slice of thickness Δz. In NMRFM, dynamical measurements are performed with a single frequency, ω_0, to control the inversions of the spins.

One of the biggest difficulties in cyclic non-adiabatic inversion is to control the thickness of the resonance slice and to manipulate the rotation of the spins when they are immersed in different magnetic fields. Figure 3.12 shows how the resonance slice thickness can be controlled. As is done with MRI, using an rf field containing an array of consecutive frequencies $\omega_0 \pm \Delta\omega'$, we can manipulate equally all the spins contained in a range $B_0 \pm \Delta'$. For the same gradient field, the larger $\Delta\omega'$, the larger the resonance slice will be.

3.4 Noise Sources

The minimum force that a cantilever in thermal equilibrium can detect, based on its characteristics, was discussed in Section 3.2. In this section other sources of noise that can add to the thermal noise, are discussed.

3.4.1 Environmental Noise

Environmental noise is all the noise present in a non-ideal instrument and can, in principle, be avoided with better design; for example, by better shielding and vibration isolation.

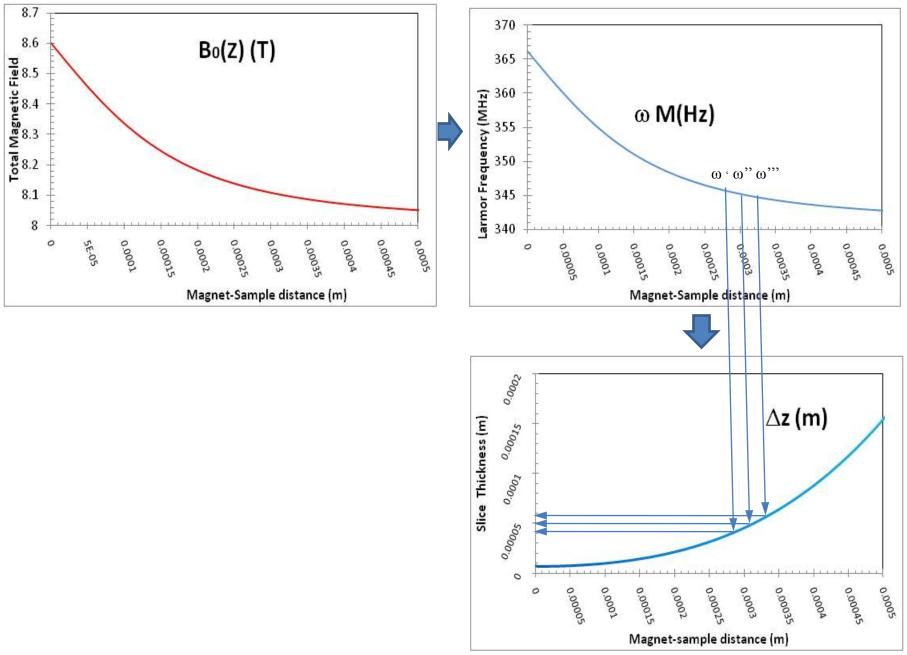

Figure 3.12: Representation of magnetic field, Larmor frequency and resonance slice. Each arrow corresponds to a different resonance frequency. An array of $\omega_0 \pm \Delta\omega'$ corresponds to a resonance slice.

3.4.1.1 Mechanical Perturbations

Due to the loading limitations of the probe in the magnet, it is not feasible to have a spring-based system that "detaches" the sensor from the environment. As a result, the system is not ideally isolated from environmental noise vibrations, making holidays, nights and weekends, the best time for data acquisition.

3.4.1.2 Laser

For cantilever motion detection in NMRFM, the most common technique used is laser interferometry. The laser is a fundamental component of the data acquisition system; but at the same time it can experience changes in its wavelength or it can generate perturbations on the cantilever that will affect the measurements. If the laser's temperature changes, its wavelength may also change. This can give a false reading to the lock-in fringe control that uses the wavelength of the light as reference to keep the fiber-cantilever distance constant. Variations in the cantilever-fiber distance result in small changes of the intensity observed. This problem can be solve by using a temperature control that keeps the laser temperature constant.

Another source of noise is the heating of the cantilever by the laser beam, especially during experiments performed at cryogenic temperatures [21, 22]. This effect increases the thermal noise, thus affecting the sensitivity of the experiments, $F_{min} = \sqrt{S_F \Delta\nu} = \sqrt{\frac{4kk_BT\Delta\nu}{\omega_c Q}}$ [22]. The intensity of the laser plays a main role in the heating factor of the cantilever. Using a 90 % to 10 % beam splitter is a way to reduce this effect. Another noise effect as a consequence of the laser incidence on the cantilever is random ω_c shifts. These deviations in the cantilever frequencies have origins in the trapping or releasing of individual electrons by the photons. These frequency shifts can be slowed down by reducing the wavelength of the Lasers used during measurements.

3.4.1.3 Mechanical Dissipation in a Static Magnetic Field

When a cantilever contains magnetic materials, magnetic dissipation can be observed as a reduction of the cantilever's quality factor [23–25]. This dissipation has mainly been observed in magnets-on-cantilevers geometries, but it has also recently been seen in non-magnetic cantilevers [26, 27]. The origin of this dissipation is the fluctuating orientation of the magnetization with respect to the magnetic field. These dissipations, which can reduce the quality factor of the cantilever, can be eliminated if the direction of the cantilever oscillation doesn't involve change in orientation between the directions of the cantilever and the magnetic field $B_0\hat{z}$.

3.4.2 Non-Contact Friction

As seen in Figure 3.2, the gradient of the magnetic field decreases in magnitude with distance from the magnet. In the search for maximum sensitivity, the sample-magnet distance needs to be reduced as much as possible. However, cantilever - magnetic tip interactions appear as a noise effect and increase as the distance between these two is reduced. This is not the case in our experiments where the sample-magnet distance is on the order of micrometers for micron-scale sample analysis, but it is typical for high resolution experiments within distances around 100 nm or less. Some of the observations and studies of these perturbations can be found at [22], [28], [29], and [30] for interested readers.

3.4.3 Thermal Noise

Thermal noise is the ultimate limiting factor of the minimum detectable force in the sensitivity of the cantilever. When the cantilever is in thermodynamic equilibrium with the environment, the equipartition theorem,

$$\frac{1}{2}k\langle x^2\rangle = \frac{1}{2}k_BT \tag{3.20}$$

indicates that the vibration amplitude of the cantilever is directly proportional to its thermal energy.

The cantilever's tip vibration amplitude can be associated with a driving force noise characterized by a white noise power spectrum, S_F, such that

$$\langle x^2\rangle = \int_0^\infty |G(f)|^2 S_F\ df, \tag{3.21}$$

where $|G(f)|^2$ is the absolute square of the mechanical transfer function, or

$$|G(f)|^2 = \frac{f_c^4/k^2}{(f_c^2 - f^2)^2 + (f_c \cdot f/Q)^2}. \tag{3.22}$$

Solving for large Q, we have $\langle x^2\rangle = \dfrac{S_F Q f_c}{2k^2}$, which we can substitute into Equation (3.20) to express the noise power spectrum density with units of $\mathrm{N}/\sqrt{\mathrm{Hz}}$:

$$S_F = \frac{4kk_BT}{2\pi f_c Q} = 4\mathit{\Gamma} k_BT \tag{3.23}$$

where $\mathit{\Gamma}$ is defined as the friction coefficient of the cantilever [22].

For minimum force detection, measurements of the spectral density with bandwidth $\Delta\nu$ gives the expression $F_{min} = \sqrt{S_F\Delta\nu} = \sqrt{\dfrac{4kk_BT\Delta\nu}{\omega_c Q}}$ that shows how cantilevers with small k, large Q and ω_c improve the minimum force that the oscillator can detect [21, 31].

3.5 Signal Sensitivity

It is assumed for the following calculations, that during the modulation sequence, all the spins remain locked to the effective field (the adiabatic condition is fulfilled), that $\frac{M_z}{M_0} = 1$, and that only thermal noise limits the sensitivity of the cantilever.

We define the signal to noise ratio (SNR) as the ratio of the maximum induced magnetic force that can be obtained from a selected section of a sample and the minimum force that can be detected by the cantilever.

$$SNR = \frac{F_{mag}}{F_{min}} = \frac{M_0 \cdot \nabla_z B}{\sqrt{S_F \Delta\nu}} \tag{3.24}$$

Using Equations 3.9 and 3.3 we obtain:

$$SNR = \frac{N\gamma^2\hbar^2 I(I+1)}{3k_B T} B_0 \cdot \nabla_z B \cdot \sqrt{\frac{\omega_c Q}{4kk_B T\Delta\nu}}. \tag{3.25}$$

For the case of a resonance slice smaller than the sample we can use Equation 3.7 to obtain

$$SNR = n2\Omega A \frac{\gamma\hbar^2 I(I+1)}{3k_B T} B_0 \cdot \sqrt{\frac{\omega_c Q}{4kk_B T\Delta\nu}}. \tag{3.26}$$

To end this section it is interesting to take a short look at an example. In 2009, C. L. Degen, M Poggio, H. J. Mamin and C. T. Rugar [20] detected a signal from 100 nuclear ^{1}H spins with a SNR of 2 at 300 milikelvin. Improvements in cantilevers, gradient magnet fabrication and measurements techniques will be necessary in order to increase the SNR for single atomic resolution measurements.

Chapter 4

Experimental NMRFM System

Our experimental system is the result of the substitution of an external manual coarse positioning stages probe [32] by a whole new system composed of piezoelectric stages and a semi-automated software control system for scan processes, measurements, and analysis.

The control and data acquisition system of the NMR-Force-Microscope is described, with software code explained in Appendix A. A PCIe-6259 multifunction DAQ from National Instruments (Austin, Texas) was chosen as the communication hub between microscope and station control. The card is a multifunction card that has 4 analog outputs at 16 bits, up to 2.8 MS/s (2 μs full-scale settling), 48 digital I/O lines and 32 analog inputs. These characteristics allow the generation of signals for control of the NMR force microscope nano-positioning stages, for spin manipulation, and for data measurements.

By using a combination of manual and digital switches it is possible ,with the DAQ card, to perform nine different functions, to control six positioning stages and also to perform frequency modulation, amplitude modulation and control of the rf gate. Only two analog inputs are used during the experiments. This arrangement allows a fast data acquisition from the lock-in amplifier and DAQ. The GPIB card controls the set up of the commercial instrumentation like lock-in amplifier, signal generator and multimeter. Simultaneously, to perform interferometer measurements, an analog fringe-lock circuit is used to keep the relative distance between fiber and cantilever fixed.

Most of the elements that comprise the experiment are described in this chapter: the nuclear magnetic resonance force microscope, laser interferometer, magnetic field gradient, position control, fiber-lock, generation of modulated rf field system, data acquisition, data analysis, and the components designed and fabricated for NMRFM measurement purposes. Figure 4.1 is a schematic representation of the whole system and its components.

The set of computer programs utilized to perform NMRFM measurements are shown in the Appendix. Those are the positioning stage control, cantilever driven scan, cantilever power spectrum density, multimeter, oscilloscope, signal generator, signal analysis and 2D image representation. The software not only controls the commercial instruments via GPIB, but also controls the main parts of the experiment, from spin excitation to data acquisition and analysis. With the advantage of sequential processes and multiple digital and manual switches, it was possible to maximize our resources with a single DAQ and GPIB card.

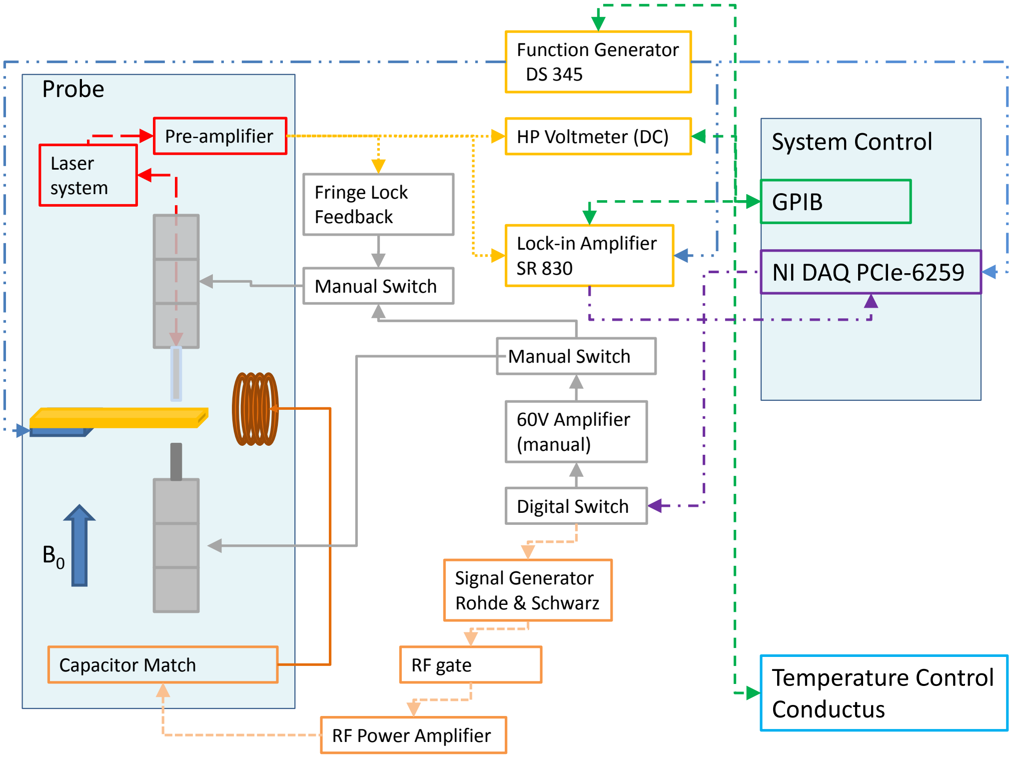

Figure 4.1: Representation of the components and connections of our NMRFM system. Green (dashed) lines indicate GPIB connections that control the setting of the commercial equipment and transmit data. Purple (dash-dots) lines are the inputs and outputs from the DAQ. The inputs come from the X and Y channels of the SR830 lock-in amplifier. The purple output contains the signals for 3D axis position control and rf modulation. A set of switches separates the type of signals into their corresponding channels: grey (solid) for position control and orange (square-dots) for rf modulation. Red (long dash) lines indicate laser signal paths and blue (long dash-dot-dot) lines are the DS 345 signal generator outputs that drive the cantilever and synchronize with the lock-in SR830 and the, DAQ.

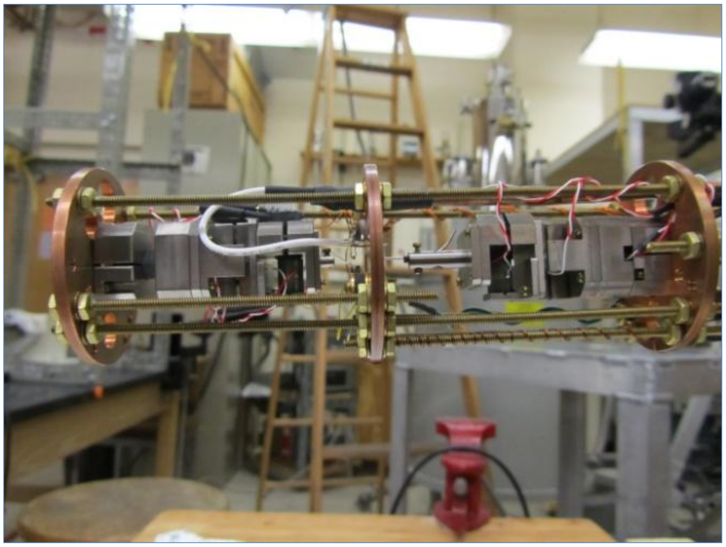

Figure 4.2: Image of the Nuclear Magnetic Resonance Force Microscope. Behind it can be seen the 8.05 T NMR superconducting magnet with the tail dewar incorporated.

4.1 Nuclear Magnetic Resonance Force Microscope

4.1.1 Cryostat Probe

The microscope is in a vacuum-sealed cryostat probe designed to work in an 8.05 T NMR superconducting magnet with a He tail dewar used for variable temperature measurements. The previous microscope contained external manual coarse positioning stages [32]. The new microscope contains piezoelectric positioner stages, three for the fiber interferometer and three for the gradient magnet. The threaded bars give us flexibility to add or remove fine piezoelectric positioners for future high sensitivity 3D measurements, or other components to the microscope without needing to make major changes to the probe.

The cantilever and the rf coil are stationary parts of the microscope, and the fiber interferometer and gradient magnet are aligned with the cantilever by using the x, y and z piezoelectric positioner stages.

4.1.2 Fiber-Optic Interferometer

The fiber optic interferometer is the component of the probe that transforms the oscillation of the cantilever into a analog voltage ready for analysis. The interferometer system is described in the following two subsections.

4.1.2.1 Laser System

As mentioned earlier, the laser power can heat the cantilever and cause noise perturbation effects. To avoid this, an 1310 nm beam from a diode laser is split in two with a 90%/10% directional coupler. The beam with 90% is sent through a fiber with a bad cleave (to avoid unwanted reflection) and the 10% beam is used for interferometry purposes, as seen in Figure 4.3. When the light reaches the end of the fiber, some is reflected and some is transmitted. The transmitted light hits the cantilever and is reflected back into the fiber. The resulting interference is a function of the fiber-cantilever distance and is transformed by a photodiode into current, then into voltage by a current-to-voltage op-amp circuit. The signal coming from the current to voltage circuit has two components, V_{DC} and V_{AC}.

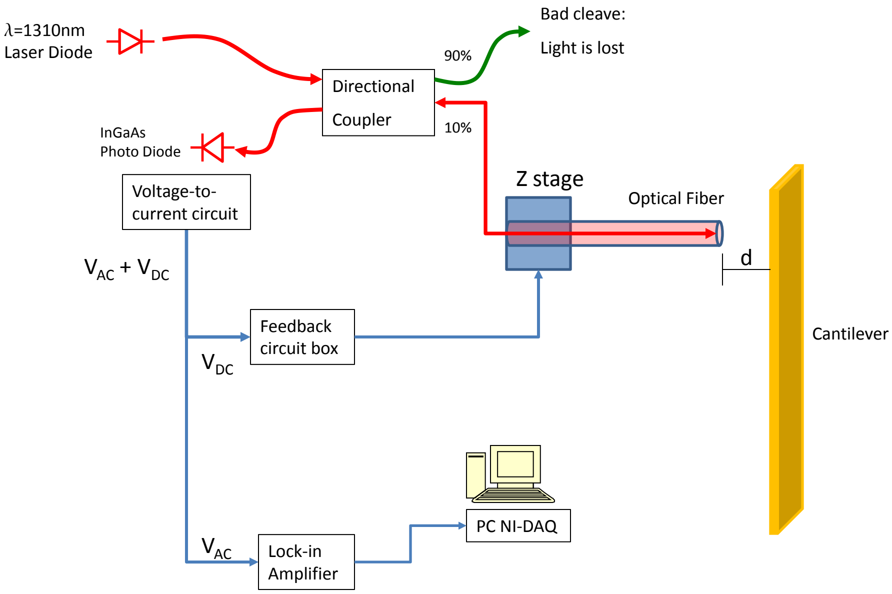

Figure 4.3: Overview of the fiber-optic interferometer and use of the signals measured

The resulting signal can be expressed as

$$V_{sig} = V_{off} + A \cdot \sin\left(\frac{2\pi}{\lambda/2} d\right), \tag{4.1}$$

where V_{off} is due to the difference in percentage between the transmitted and the reflected light at the tip of the fiber and λ is the wavelength of the laser. Constructive interference occurs when

$$2d = (n + \frac{1}{2})\lambda \tag{4.2}$$

and destructive interference occurs when

$$2d = n\lambda. \tag{4.3}$$

If the fiber-cantilever distance varies, the output voltage measured will change as a function of d, as described by Equation (4.1). The DC component, measured with a voltmeter, is an indication of the cantilever-fiber distance and is used to keep a fixed distance between both components during measurements.

On the other hand, the AC component of the signal represents the cantilever oscillations. These oscillations are on the order of nanometers in amplitude and have frequencies on the order of kilohertz, measurable by lock-in amplifiers. Figure 4.3 shows how the AC component of the voltage-to-current circuit output is measured with the lock-in amplifier for cantilever oscillation measurements. The voltage signal displacement measured from the fringe center, $\partial V_{sig}/\partial d$, can be converted into the amplitude of vibration of the cantilever by using:

$$\frac{\partial V_{sig}}{\partial d} = \frac{2\pi}{\lambda} V_{pp}. \tag{4.4}$$

The top graph in Figure 4.4 is a recorded measurement of the interference signal when the fiber is moving towards the cantilever. Two effects are evident in this graph: the oscillation due to the interferometry effect and an increase of the amplitude V_{pp} because as the fiber gets closer to the cantilever, more light gets reflected back into the fiber. The bottom graph shows the linear behavior of the fringe around its center as described in Equation (4.4).

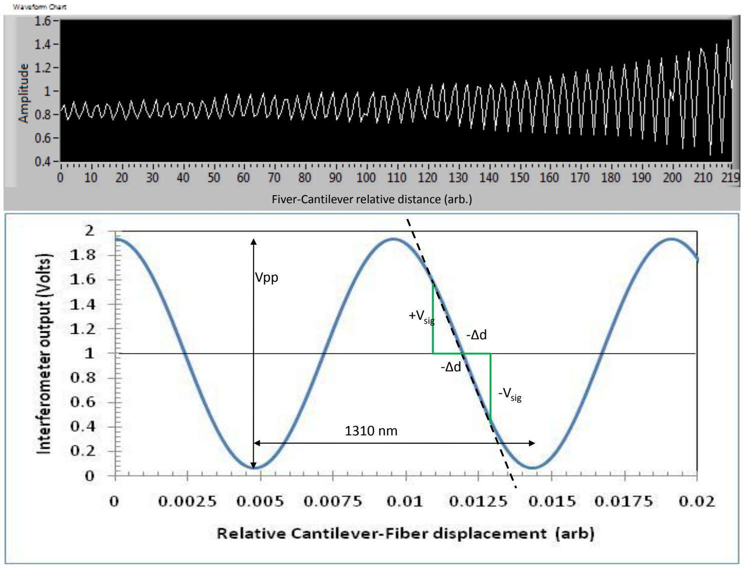

Figure 4.4: Top, interferometer voltage output as fiber moves closer to the cantilever. Bottom, interferometry fringe as a function of fiber-cantilever distance.

This linear behaviour is used for two purposes: The first purpose is to calibrate the interferometer cavity length so that the fiber-cantilever distance can be kept constant with the use of a feedback circuit lock; the second purpose is to calibrate the measurement of the cantilever's small tip oscillations.

4.1.2.2 Feedback Circuit for Fiber - Lock

In order to measure the cantilever's oscillations, it is necessary to keep the mean cantilever-fiber distance constant, that is, to stay on a known (the ateepest) part of the interference pattern. For this purpose, we use a home-made analog feedback circuit that controls the voltage that drives the z piezo

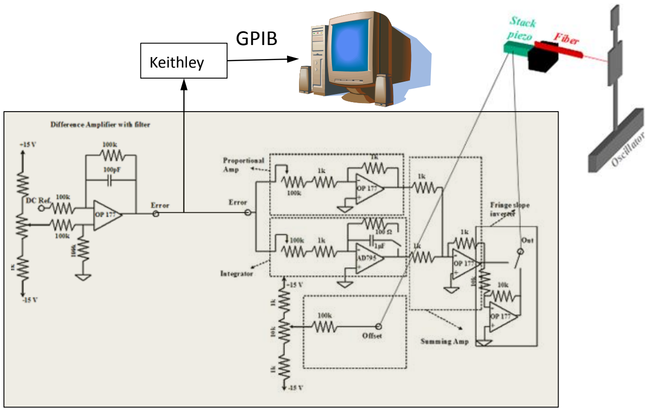

Figure 4.5: Analog fringe lock circuit diagram.

to lock in the position of the fiber with respect to the cantilever. Scans of the distances provide interferometric fringes where the peak-to-peak distance represents a movement of distance $\lambda/2$. Locking the position when the voltage of the interferometer is at the center of the fringe gives the most linear measurement of the cantilever oscillations, as is seen in Figure 4.4.

Our feedback circuit is a copy of the one used by Utkur Mirsaidov [23] shown in Figure 4.5. However, other types of circuits like the ones at [32–34] and [35] function as well. The mechanism is the same regardless: a piezo-stack controls the z position of the fiber and a varying voltage from -15 V to $+15$ V controls the length of the z piezo and thus the position on a fringe. A description of the procedure necessary to lock the fiber-cantilever distance with the fringe lock feedback circuit can be found in Reference [33] [p.121]. Since the piezo-stack behaviour is temperature dependent, it is necessary to make adjustments in the feedback voltage that drives the piezo to obtain the same results at cryogenic temperatures.

4.1.3 Mechanical Oscillator Characterization

The NMR Force Microscope system is built around the cantilever sensor held against a piezo plate, which is used as a shaker, and these two components are attached to the middle plate shown in Figure 4.2. The sample, a micrometer size ammonium sulphate crystal, is attached to the cantilever with five-minute epoxy. The external magnetic field is perpendicular to the cantilever. As mentioned earlier, the amplitude of the cantilever's oscillation at its resonance frequency is given by $A = Q\frac{F}{k}$, and the CAI demands that $\frac{(\gamma B_1)^2}{\omega_c \Omega} \gg 1$. Thus the most important characteristics of a mechanical oscillator for our experiments are the quality factor, resonance frequency and the spring constant.

In this section, the main methods used to determine these three values will be described in detail. We use two methods for this purpose: 1) driven frequency scans and 2) fast fourier measurements of the power spectral noise.

4.1.3.1 Driven Frequency Scan

The cantilever is located on top of a PZT 840 piezo plate transducer (American Piezo Ceramics, Inc.) that can be driven with a function generator (DS 345) that generates a sinusoidal voltage signal. The expansion of the piezo is described by

$$\Delta h = d_{33} V, \tag{4.5}$$

where d_{33} is a temperature dependent constant.

To perform resonance-frequency scan measurements, a newly redesigned Labview software is used. This program controls the frequency settings of the DS 345, reads the data through a Stanford Research SR 830 DSP Lock-in Amplifier and stores the measured R, X, Y, and ϕ values for each one of the driving frequencies.

For each driven frequency scan, the oscillation amplitude Δh is set constant during the scan. The cantilever is shaken at frequency f during an acquisition time ΔT, and the driven frequency is changed in steps of size Δf. The cantilever's tip oscillation amplitude is measured by the fiber interferometer and sent to the lock-in amplifier that is synchronized with the DS 345. The signals are averaged with a time constant τ that also defines the time interval length of measurements $\Delta T = 5 \cdot \tau$ and the driven step size $\Delta f = 1/4\tau$ for a 6 dB/octave filter. It is always convenient to choose step sizes around 1% smaller than the bandwith size and deduce from there the corresponding values of τ and ΔT.

Figure 4.6 shows the resonance frequency scans with X (the in-phase channel), Y (the quadrature channel) and $R = \sqrt{X^2 + Y^2}$ values from a cantilever provided by John Maroon and Jonilyn Longenecker. The graphs show that for different phase settings, R doesn't change while X and Y components vary with respect to each other.

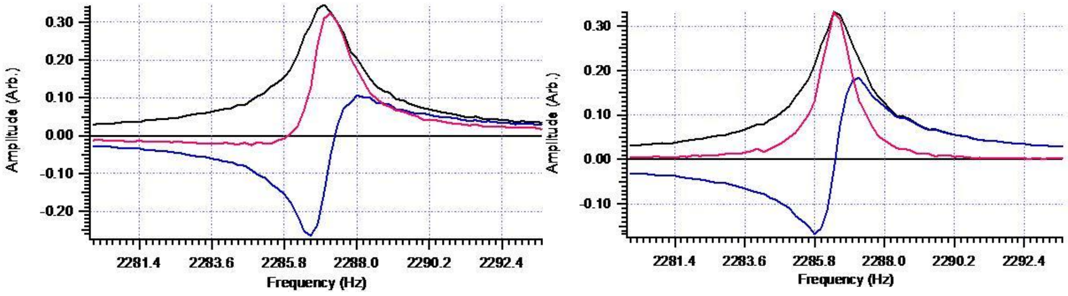

Phase 0

Phase 28

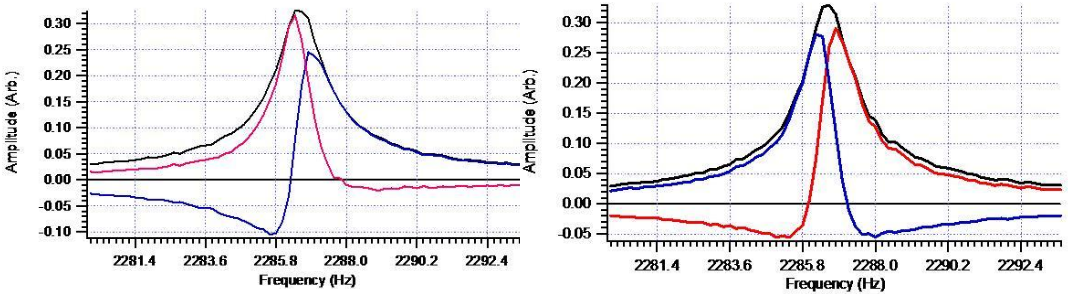

Phase 50

Phase 70

Figure 4.6: Resonance frequency scans for different values of the phase of the lock-in amplifier. R values are shown in black lines; Y values in blue lines, and X values in red lines.

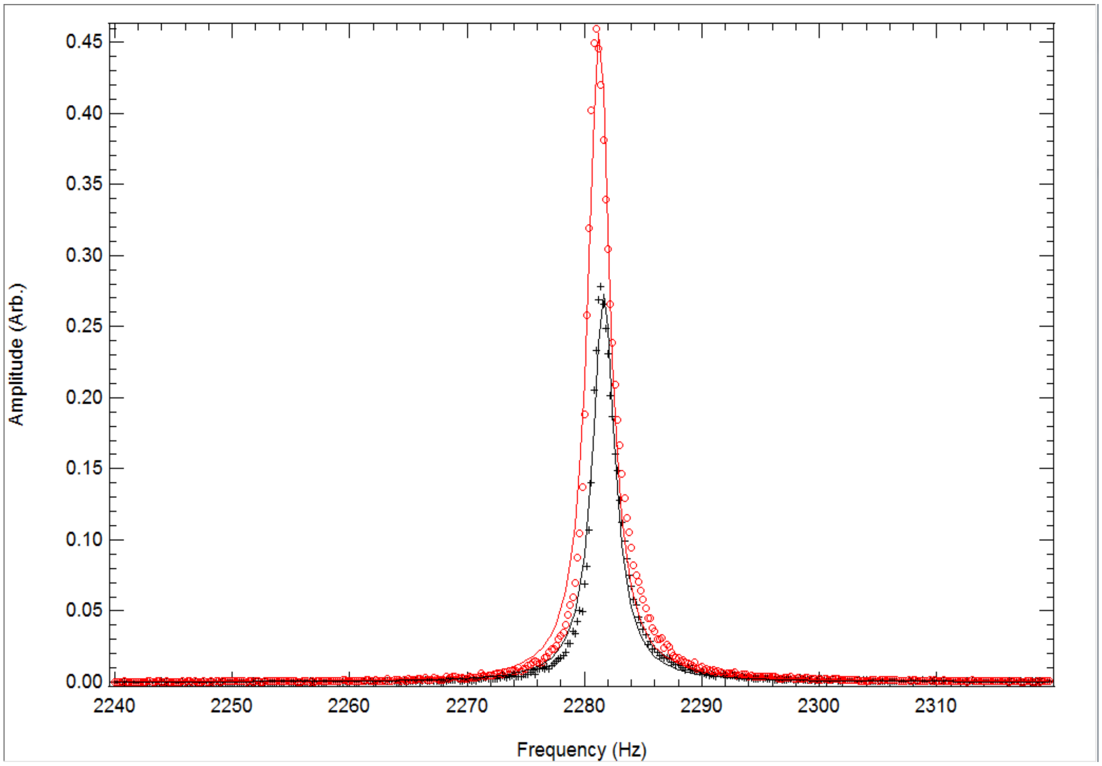

Figure 4.7: Resonance frequency scans of X with Lorentzian fits for two different driving amplitudes.

For our measurements, we set the phase at a value that, at exactly the resonance frequency of the cantilever, makes X a maximum and Y zero. The result can be seen in Figure 4.6 at phase 28. The frequency scans of the X component were fitted to a Lorentzian curve with Igor Pro software and the value of Q was obtained by dividing the resonance frequency of the cantilever by the full width at half maximum (FWHM) of the curve

$$Q = \frac{\omega_c}{\Delta\omega}. \tag{4.6}$$

Figure 4.7 shows the X measurements of two driven scans and the corresponding Lorentzian fits. The averaged values obtained from both fits are $f_c = 2286$ Hz and $\Delta\omega = 1.170$ Hz giving $Q = 1953$.

4.1.3.2 Power Spectral Noise and Spring Constant

For the characterization of the cantilever's spring constant k, an indirect method based on the equipartition theorem is used. As seen in Section 3.4.3, thermal noise will make the cantilever vibrate with some amplitude that can be related to the driving force noise characterized by a white noise power spectrum S_F. Since the lock-in amplifier measures the RMS noise vibrations with some bandwidth related to the power spectrum, the amplitude of the cantilever vibration can be obtained for spring constant characterization. The RMS noise vibration $\sqrt{|G(f)|^2 S_F}$ is measured by the lock-in taking a time series measurement at some previously determine frequency and bandwidth. A fast Fourier transform (FFT) of the digitized measurements results in a graph

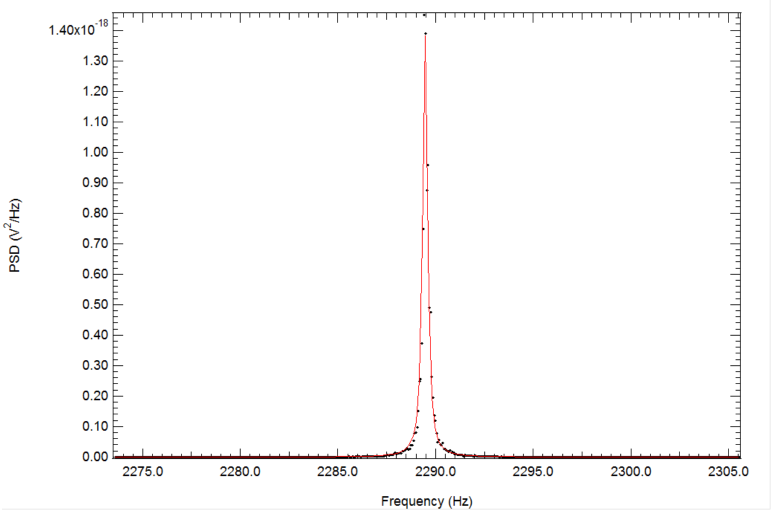

Figure 4.8: Noise Power Spectrum as obtained from Labview software

in the frequency range showing the RMS amplitude spectrum. Squaring the RMS amplitude spectrum and dividing it by the bandwidth, the noise power spectrum is obtained.

The mean square noise vibration amplitude of the oscillator for a fixed temperature described in Equation (3.12) is due to the contribution to the noise power by the frequency spectrum. This area under the noise power spectrum, shown in Figure 4.8, gives the value $\langle x^2 \rangle$. The Equipartition Theorem, Equation (3.20), a link between thermal energy and mechanical energy, is used to calculate its spring constant k from the mean square noise vibration amplitude of the cantilever due to thermal noise.

Previously, in our experiments the data were stored in the lock-in amplifier's memory with a maximum sampling interval of $\Delta t = 1/512$ Hz. A new program was developed in which the data were measured and stored using the DAQ to achieve a faster sampling rate during data acquisition. With this new program, we are able to sample at up to 1 MS/s. The time series is then Fourier transformed using Labview. The frequency resolution of this Fourier transform is

$$\Delta f = \frac{1}{N\Delta t} = \frac{f_S}{N}, \tag{4.7}$$

where f_S is the sampling rate and N is the number of points stored. Large time measurements or low sampling rates increase the frequency resolution. However, the frequency range scanned is determine by the sampling rate:

$$f_{range} = \frac{N}{2} \cdot \Delta f = \frac{f_S}{2}. \tag{4.8}$$

Equations 4.11 and 4.12 provide the variables that set the resolution and range of the FFT measurements. During measurements, it is required that the bandwidth of the lock-in amplifier ($\Delta\nu$) be at least twice the spectrum of the FFT, $\Delta\nu \geq \dfrac{2}{\Delta t}$, so that the roll-off of the filter will not attenuate the outlying frequencies.

4.1.4 Permanent Magnet

A sample-on-cantilever geometry was chosen to perform our experiments. The sample was attached to a cantilever aligned perpendicularly to the magnetic field and a long rod with its geometrical long axis along the oscillation direction of the cantilever, as shown in Figure 3.1, is an optimal

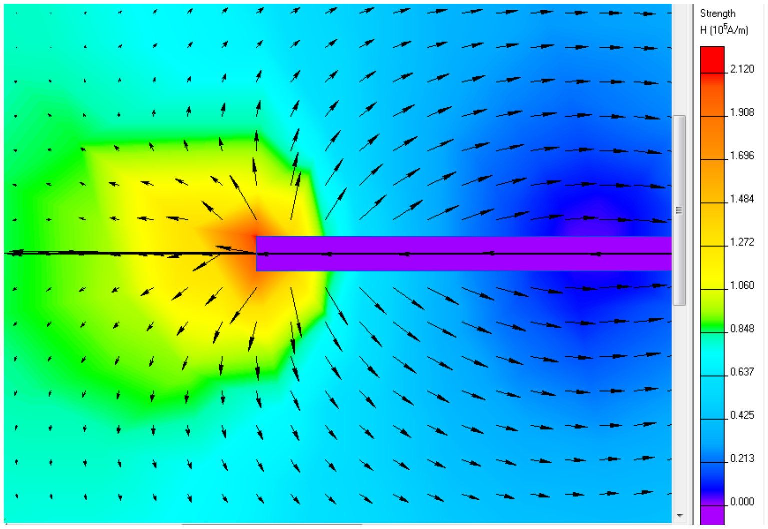

Figure 4.9: Value of the Magnetic field of a Permalloy Bar in a 1 Tesla magnetic field

geometry to generate a large magnetic field gradient. The magnetic field for a uniformly magnetized rod is described by

$$B_{PM}(z) = \frac{4\pi M}{2}\left(\frac{z}{\sqrt{z^2+r^2}} - \frac{z-L}{\sqrt{(z-L)^2+r^2}}\right), \tag{4.9}$$

while the gradient of the magnetic field along the same direction can be described by

$$\frac{\partial B}{\partial z} = \frac{4\pi M}{2}\left(\frac{1}{\sqrt{z^2+r^2}} - \frac{z^2}{(z^2+r^2)^{3/2}} + \frac{(z-L)^2}{((z-L)^2+r^2)^{3/2}} - \frac{1}{\sqrt{((z-L)^2+r^2)}}\right). \tag{4.10}$$

where M is the magnetization of the magnet, z is the magnet-sample distance along the long axis, L is the length of the magnet and r is the radius of the magnetic cylinder.

Figure 3.2 shows the total magnetic field and the value of the gradient from which we can optimize the resonance slice size and force by carefully adjusting the sample-magnet distance. Figure 4.9 shows a two-dimensional simulation of the direction and intensity of the magnetic field generated by a permalloy rod aligned along an external magnetic field with QuickField software.

4.1.5 The RF Coil

The rf field responsible for spin manipulation was provided by a 0.5 mm diameter wire rolled around the same type of wire to form a coil with three turns. This wire is coated with Niclad, an insulator that prevents shorts between the individual turns. The equation that describes the magnetic field generated by a coil with current I is:

$$B = \frac{1}{2}\frac{\mu_0 N I}{L}\left(\frac{x}{\sqrt{x^2+R^2}} - \frac{x-L}{\sqrt{(x-L)^2+R^2}}\right) \tag{4.11}$$

where $\mu_0 = 4\pi \times 10^{-7}$ T·m/A, N/L is the number of turns per unit length, I is the current, x is the distance outside the coil along the axis and R is the radius. Figure 4.10 shows the coil, the sample, and the cantilever used during the experiments.

At rf, the capacitance and inductance of the circuit plays a major role in the efficiency of the power transmission. The power delivery from the power amplifier to the coil is maximized by using a tuned, or impedance-matched, network to avoid power reflections at the cable interfaces or other circuit components . The use of variable tuning capacitors and an HP Network Analyzer

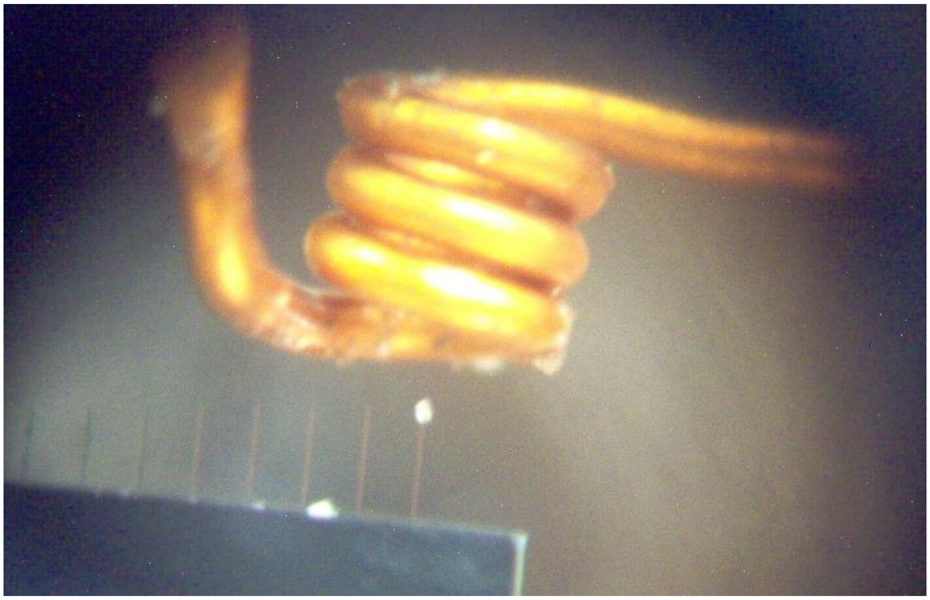

Figure 4.10: Image of coil, cantilever and sample.

allows us to adjust the circuit overall impedance to 50 Ω. The capacitors, located outside the probe for easy tuning, are connected to the coil by a rigid coaxial cable (RG 174) that runs along the probe. The tuning capacitors are either parallel tuned series matched or series tuned parallel matched as shown in Figure 4.11.

When the modulated waves are allowed through the rf gate, the waves are amplified in an ENI 5100L-NMR rf Power Amplifier by 50 dB with a maximum output of 100 watts. The maximum transmission of power is achieved when the carrier frequency of the wave and the tune frequency of the circuit

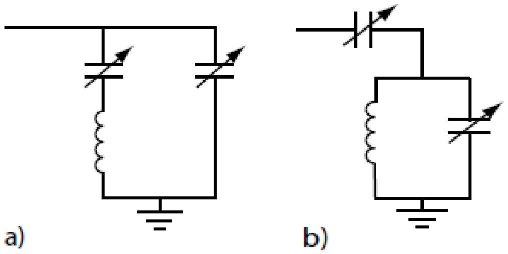

Figure 4.11: Possible impedance matched configurations: a) parallel matched series tuned, b) series matched and parallel tuned

match. As the carrier frequency moves away from the tuned frequency the power delivered decays; how quickly is a function of the quality factor of the circuit. The potential of the rf coil to generate the B_1 field is proportional to $Q = f/\Delta f$, the quality factor of the circuit. High quality factors allow high fields, but since they have narrow frequency bands, small changes in frequency will cause large changes in the amplitude of B_1.

4.1.5.1 RF Signal and Artifact

The core of the NMRFM experiments consists of coupling the frequency-modulation (FM) of the carrier frequency to the cantilever's resonance frequency, as was indicated in Section 3.3. High Q factors will help to generate large B_1 fields, a desired property to overcome the linewidh effect in solid samples and simultaneously accomplish the CAI condition with high amplitudes of FM. At the same time, high Q factors can cause amplitude modulation (AM) as the frequencies move away from the carrier frequency, producing undesired

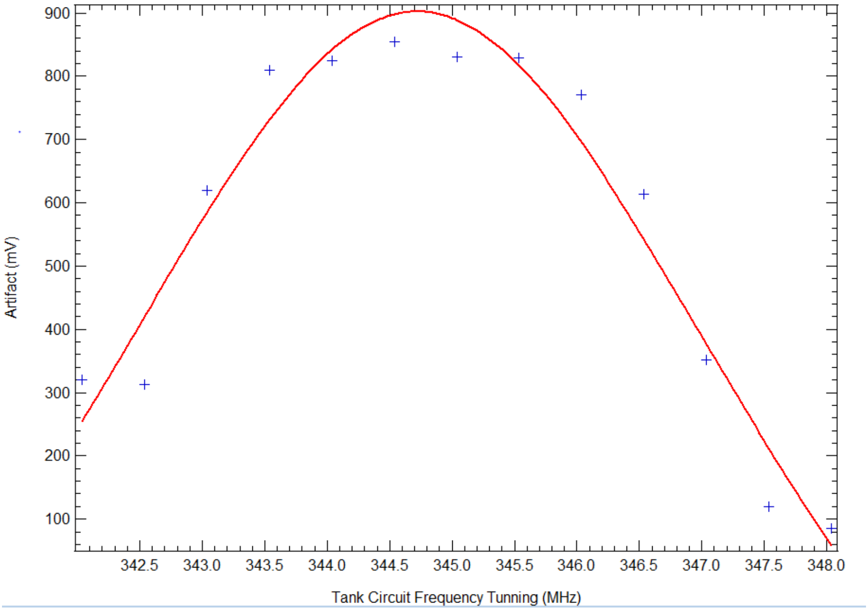

Figure 4.12: Artifact effects as a function of the frequency at which the tank circuit is tuned. The signal generator carrier frequency is set to 346.0 MHz.

artifact effects on the cantilever.

Figure 4.12 shows the cantilever artifact effects for a constant value of the carrier frequency center at 346.0 MHz and the tank circuit tuned for different frequencies. It can be observed that as the tank circuit is tuned for frequencies away from the carrier frequency, the artifact effect is reduced because the B_1 amplitude is also being reduced during frequency modulation. Here, modulation of the rf wave matches the cantilever frequency, $f_c = 2288.6$ Hz. The amplitude of modulation input was set to 1000 mV, which is equivalent to 500 kHz. The lock-in amplifier time constant 1 ms and the sensitivity 1 mV. Figure 4.13 shows the cantilever artifact effect around the cantilever's resonance frequency. There is a noticeable decay of the artifact as the modulated frequency moves away from the resonance frequency.

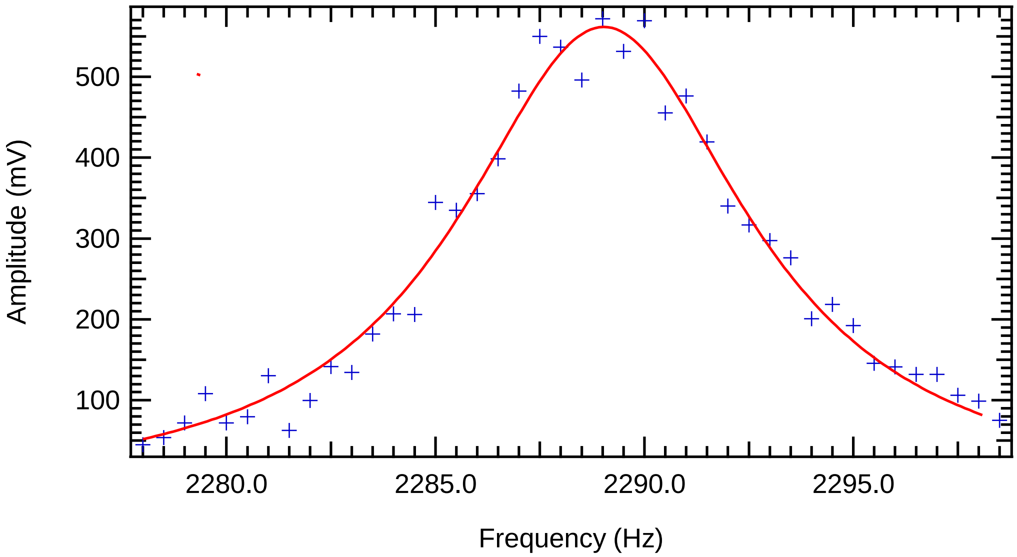

Figure 4.13: Artifact effects as a function of the modulation frequency. The cantilever resonance frequency is 2288.6 Hz

One possible technique used to avoid the artifact effects using the sawtooth technique in which the FM and the AM oscillate at $2\omega_c$ but modulate the spin at ω_c, as described in Section 3.3.2. Another possibility is the use of the cyclic non-adiabatic inversions (CyNAI) as described in Section 3.3.3, where matching ω_1 with ω_c avoids the necessity of any type of modulation. Finally, another possibility is the use of microwires instead of coils, as described by M. Poggio et al. [17]. Since microwires are not as dependent on a quality factor, there are smaller changes in the amplitude of the magnetic field during modulation, and large artifact effects are not induced on the cantilevers.

4.1.5.2 Frequency Modulation Comparison

As indicated in the previous section, artifact effects can be avoided or mitigated by the use of different techniques. Here we show several studies of the effects of different modulation techniques on different cantilevers.

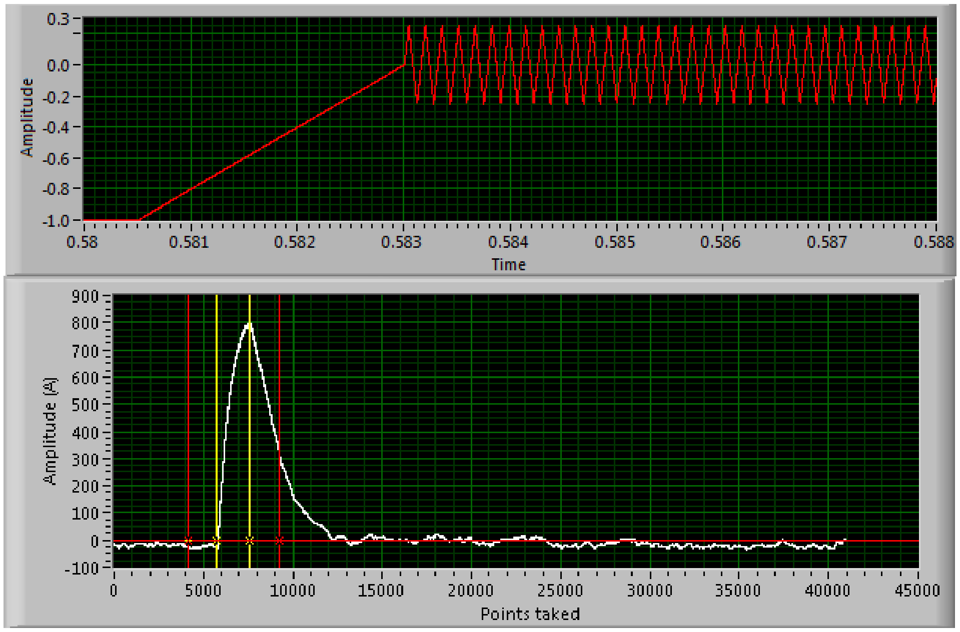

Figure 4.14: Top, triangular modulation wave. Bottom artifact effect.

The first cantilever studied, courtesy of Jae-Hyuk Choi at KRISS, was also used during dynamical NMRFM measurements of ammonium sulphate

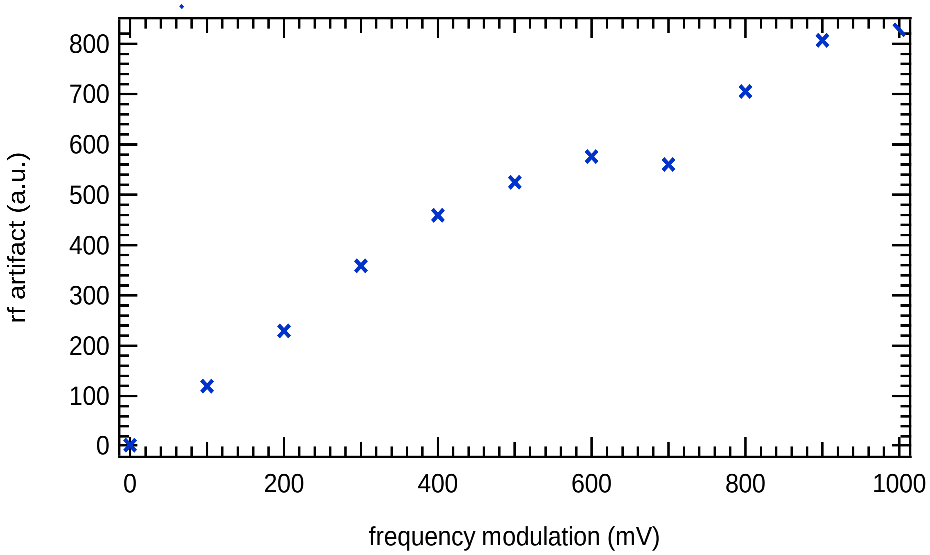

Figure 4.15: Artifact effects as a function of the amplitude of the FM.

and had values of $Q = 1032$, $k = 0.0056$ N/m and $f_0 = 6400$ Hz. The artifact is due to the triangular-shape frequency modulated rf field shown in Figure 4.14. The deviation from the carrier frequency, $\Delta\omega$, during modulation is expressed in volts instead of frequency units. A more detailed explanation will be given below where rf generation is explained. For now, keep in mind that there is a linear behavior where ±1 V is the equivalent to ±500 kHz with 1% uncertainty.

A measurement of the cantilever's perturbations for different magnitudes of the frequency modulations is shown in Figure 4.15. It can readily be seen how the artifact increases as we increase how much the frequency deviates from the carrier wave. A more detailed look shows that the reaction of the cantilevers for the first five $\Delta\omega$ have different constant of proportionality than for the largest deviations. For small $\Delta\omega$, the perturbations are linearly dependent on the increase in modulation. As a result an harmonic response of the cantilever to the perturbations and/or to the fact that the change in rf field amplitude is small at the tip of the tuned circuit transfer function. The different rate of increase of the artifact at higher $\Delta\omega$ may be due to a non-harmonic behaviour of the cantilever and/or to the fact that the amplitude of the B_1 field change is smaller for large $\Delta\omega$ owing to the transfer curve of the quality factor.

Using another type of cantilever, courtesy of Jonilyn Longenecker and John Marohn at the department of Chemistry and Chemical Biology at Cornell University, similar artifact studies have been performed. A typical new cantilever had values of $Q = 3338$, $k = 0.000322$ N/m and $f_0 = 2288.8$ Hz. This type of cantilever is more sensitive to the changes in the amplitude of the rf magnetic field B_1. As a result, shown in Figure 4.16, the cantilever is highly perturbed in a way that saturates the lock-in amplifier and measurements of the oscillation amplitudes can't be performed. If cantilevers of this type are to be used with rf coils as a source to generate the magnetic field, techniques other than triangular modulation must be used.

Sawtooth-shaped frequency modulation with amplitude modulation, as in Figure 3.7, appears to be a solution to this problem. Sawtooth frequency modulation at $2\omega_c$ with amplitude modulation was studied and observed for this cantilever. As can be seen in Figure 4.17, the artifact effect appears at double the resonance frequency of the cantilever without perturbation at the

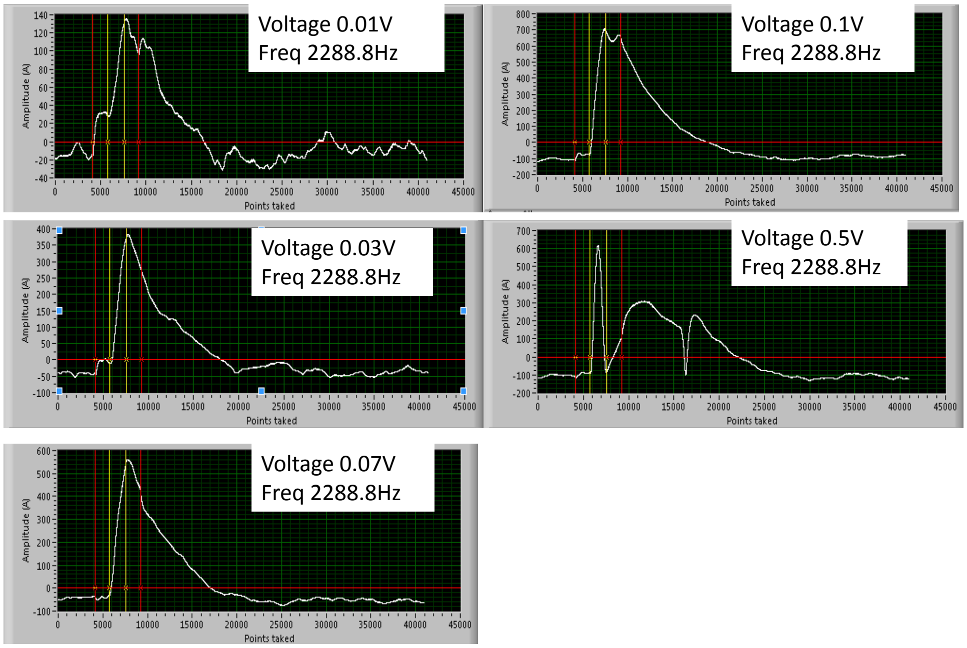

Figure 4.16: Cantilever artifacts for different $\Delta\omega$ frequency modulations.

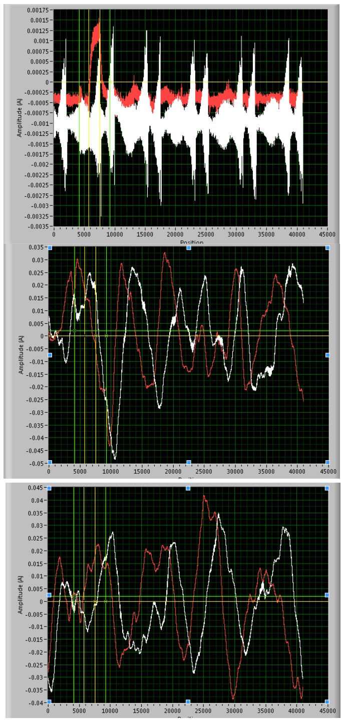

•Resonance freq cantilever	2289.3 Hz
•Resonance frequency rf signal	4578.6 Hz
•Lock-in amplifier at	4578.6Hz

•Resonance freq cantilever	2289.3 Hz
•Resonance frequency rf signal	4578.6 Hz
•Lock-in amplifier at	2289.3Hz

•Resonance freq cantilever	2289.3 Hz
•Resonance frequency rf signal	Noise
•Lock-in amplifier at	2289.3Hz

Figure 4.17: Cantilever artifact effect for sawtooth frequency modulation observing at $2f_c$ (top image), at f_c (middle image), and with only cantilever thermal noise at f_c (bottom image)

resonance frequency. It is expected that by using this technique, the signal observed will only be from the contribution of the modulated spin force and thermal noise, since artifact effects have been eliminated.

A comparison of artifact effects for the same cantilever using triangular modulation and pulse modulation (like the one shown in Figure 3.10) was performed and is shown in Figure 4.18. The two resonance frequencies of the cantilever utilized were: $\omega_c = 2290$ Hz represented in red squares and $\omega_c = 17770$ Hz represented by blue circles. The first five points are pulse sequence mea-

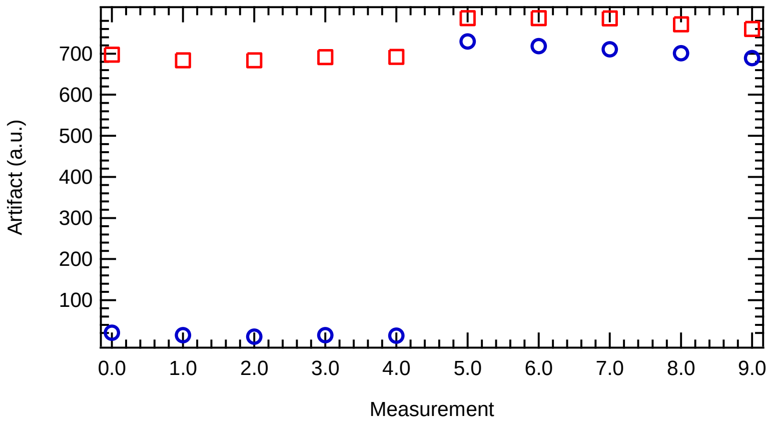

Figure 4.18: Artifact effects for the same cantilever using triangular modulation and pulse modulation. The two resonance frequencies of the cantilever utilized were: 2290 Hz represented in red squares and 17770 Hz represented by blue circles. First five points are pulse sequence measurements and the rest are correspond to artifacts measurements during triangular FM.

surements and the rest correspond to artifact measurements during triangular FM. The studies were performed with $B_1 = 33$ G, which corresponds to π pulses of length 4 μs. For triangular modulation at each one of the cantilever's resonance frequencies, the artifact effect has similar intensity. In both cases triangular modulation induces larger artifacts than the ones generated by the pulse modulations. A dependency with the resonance frequency of modulation is noticeable in this case. For higher frequencies of the cantilever ω_c, the ratio with respect to the Rabi frequency ω_1 decreases because the time where the rf field frequency is off resonance is smaller. As mentioned in Section 3.3.3, the artifact effect became zero with $\omega_c = \omega_1$.

4.2 Positioning Control

In previous sections, cantilever characterization with the fiber interferometer has been described, including the role of the gradient magnet. Also, the rf coil system used to generate the magnetic field B_1 has been discussed, including the inconvenience of a change of the magnetic-field amplitude during frequency modulations. Now we will describe the positioning control of the gradient magnet and the fiber interferometer.

The control system is a design borrowed from Attocube Systems' nanopositioners. The microscope uses two identical stages, one for the positioning of the fiber optic interferometer with respect to the cantilever and the other for the gradient magnet positioning, also with respect to the cantilever. Figure 4.2 shows how the two stages are incorporated into the microscope.

The Attocube stages are of the slip-stick type with capabilities of coarse motion of several millimetres and finer motion on the sub-nanometer scale. The clamping pieces are made of titanium because of the non-magnetic properties and light weight of the material. These pieces are clamped to a machined graphite bar thanks to screws with springs underneath to control the clamping force. At the same time the graphite bar is epoxied to another titanium holder piece with Epotek H77 black epoxy. The stages are driven with a sawtooth signal that is described in [35, page 30].

To drive the piezo stacks, a software control system has been developed to drive the stages sequentially where the step size and frequency can be

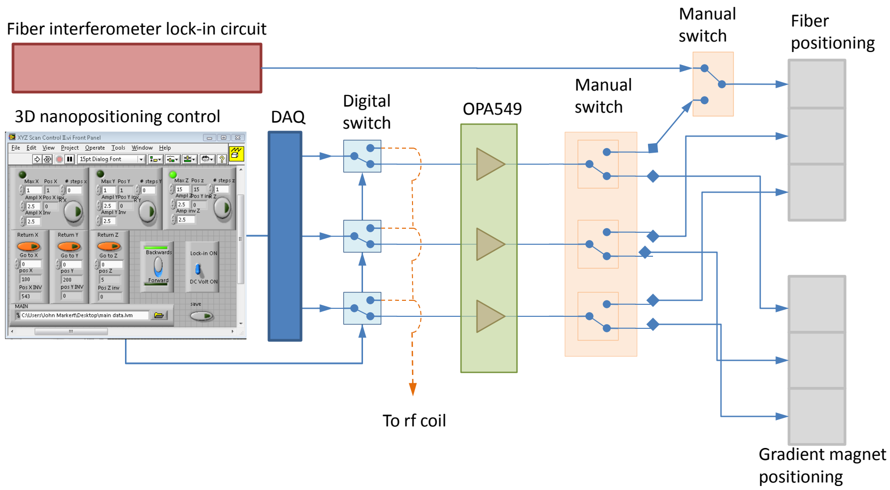

Figure 4.19: Nano-positioning control diagram generated by the 3D Scan control system explained in the text.

calibrated. The software generates a sawtooth signal with an amplitude of up to 5 V, which is amplified up to 60 V with a set of three OPA549 high-voltage op amps. Each one of them drives, although not simultaneously, the two stages assigned to the same axis. A switch is used for the selection of the gradient magnet or the fiber stage. These op amps have the ability to withstand high voltages, and high currents simultaneously, a characteristic necessary for performing the fast voltage drops that define the sawtooth shape.

During NMRFM experiments, the z axis of the fiber stage, when it is not being driven by the software positioning control, is connected to the feedback lock circuit for use for interferometric purposes. Meanwhile, the gradient magnet stage used for scanning is driven between measurements.

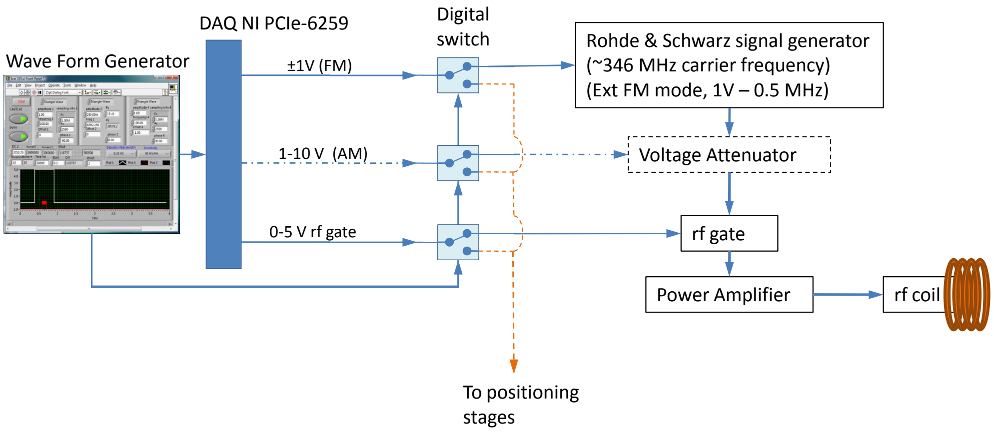

Figure 4.20: Rf generator set-up. Amplitude modulation is optional in the system.

4.3 RF Generator

The RF waves that couple the spin modulation with the cantilever's resonance frequency are generated in a home-made Labview signal generator. This signal generator allows us to customize the design of the spin manipulation protocols and the continuous shape of waves that are used during the measurements. Triangular, sawtooth, or sinusoidal frequency modulations are easily available. The system allows us to synchronize frequency modulation and amplitude modulation in the same wave, as can be seen in Figure 4.20.

All the generated output waves come from the DAQ as voltage signals and are redirected, thanks to a digital switch, into a signal generator, a voltage attenuator, and an rf gate. The frequency modulation output with a range between -1 V and 1 V is sent into a Rohde & Schwarz signal generator set to have a carrier frequency near 346. MHz. At this carrier frequency and in external frequency-modulation mode, a linear transformation allows for a frequency deviation of 500 kHz for 1 V input. When this technique is used, the phase of the carrier can't be easily synchronized with the modulated input signal. For measurements where phase synchronization is necessary, this technique is not valid. However, in our experiments, the cantilever-frequency modulation signal need not be synchronized with the carrier phase.

If a sawtooth wave is needed, amplitude modulation must be included and synchronized with the frequency-modulated wave to keep hold of the magnetization, as discussed in Chapter 3. Our custom design passes a continuous wave through an rf gate controlled by a 0-5 volt signal, also generated by the same customized signal generator, and synchronized with the waves. This signal simultaneously triggers the data acquisition program, a custom-made oscilloscope software that reads the X and Y outputs from the lock-in amplifier and saves them in the right folder. A third output with voltages between 1-10 V from the signal generator controls the variable attenuator, model number $ZX73-2500+$ from Minicircuits. The frequency-modulated waves coming out from the Rohde & Schwarz are sent into the voltage variable attenuator where the amplitude of the wave is modulated up and down twice each cantilever cycle.

4.4 NMRFM Measurements

When the right conditions are obtained: resonance slice located in the sample, B_1 large enough to overcome the linewidh of the sample, small artifact effect, and large amplitude of modulation fulfilling the CAI condition; the induced magnetic forces can be observed. During modulation, the signal measured by the data acquisition system will be a combination of the artifact and the nuclear magnetic force. Assuming that the artifact effect remains constant during measurements as shown in Figure 4.18, this effect can be considered as an offset in the measurements. If a signal is measured in which the cantilever's amplitude is larger than the offset, a more precise study will be conducted to verify whether a magnetic force has been measured.

The design and generation of the modulation in frequency and amplitude is tailored in our custom-made Icai 105 software. Once the signal is built, it is synchronized with a second signal, a pulse, that will act as a trigger. Both digital signals are sent into the DAQ to be transformed into analog waves. The FM signal is sent into the Rohde & Schwarz and the pulse will open and close the rf gate or trigger the oscilloscope. The cantilever response is sent into a lock-in amplifier and the in-phase and quadrature channels are sent back to the DAQ, digitized and read by a custom-built oscilloscope. Both signals are read at a sample rate of 8192 S/s and saved automatically in the same folder. The oscilloscope has the features of averaging, controlling the acquisition sample rate, and the use of different types of triggers. The oscilloscope has the capability of recording consecutive measurements with the feature called: save

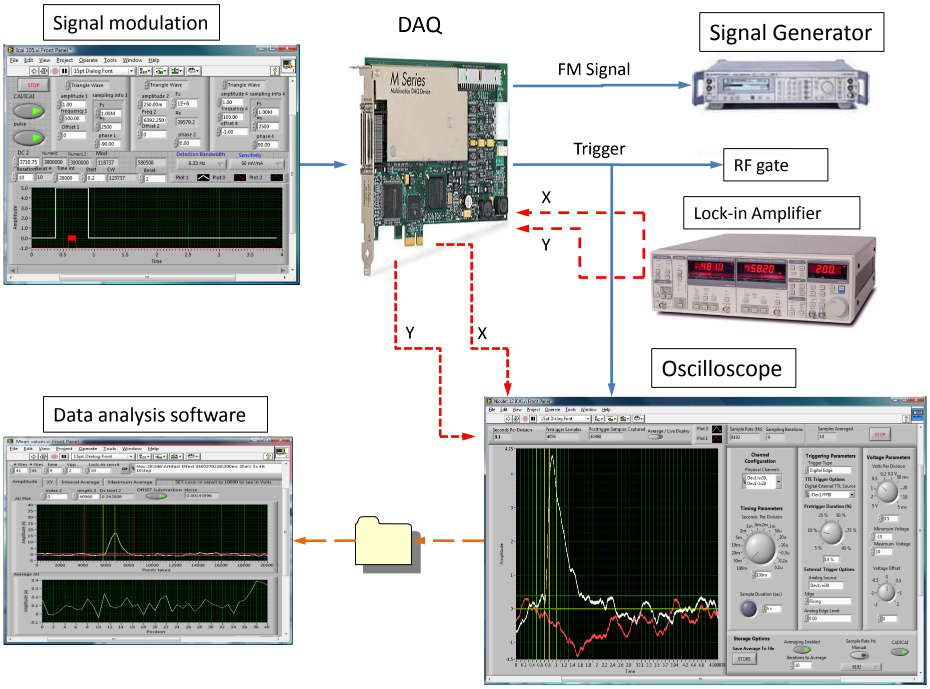

Figure 4.21: Data acquisition and analysis process. Our handmade signal generator sends the analog signals to the rf gate and to the Rohde & Schwarz signal generator. The cantilever response is sent into a lock-in amplifier and the in-phase and quadrature channels are sent back to the DAQ and read by a custom-built oscilloscope. Both signals are read and saved automatically in a folder. The data analysis software reads each file and shows a representation of the cantilever oscillation for each measurement.

using the next available filename. With this feature all the files containing the measurements are recorded with the same name but ending with a number that sets the order in which they were recorded. This particular feature allows the use of an automatic data analysis software.

NMRFM gradient magnet position scans are tedious and long. Depending on the size of the steps and their range, the scans can have hundreds of files. Since each file corresponds to a five-second time series, the number of points per file is 40960. However, since each measurement recorded contains the order in which they were stored, a program can read all the files keeping the same order as when they were obtained. Because of the trigger, all the artifacts always start at the same position for all the measurements. The program is set to look only at a specific section of the artifact or signal-plus-artifact and average all the values with respect to an averaged baseline. At the same time, the software looks at the maximum value of the time series, corresponding to the end of the continuous wave, and averages the values for a determined interval of points around this maximum. The advantage of this system is the reduction of hundreds of time series to a single file containing the averaged values of the cantilever responses at each measurement.

If the spin magnetic force is detected by the catilever during the scans, the set of measurements will contain files with only artifacts and files containing both. With the Main Values program, the files with the nuclear magnetic force most often appear during the scans as a larger oscillation by the cantilevers than the ones with only artifact (that is, the signal is in phase with the artifact for our arrangement). This effect is shown in next section where the results of two gradient position scans are shown.

Chapter 5

Results and Discussion

5.1 Introduction

Position-dependent force-detected NMR measurements on a 25x15x7 μm^3 single crystal of ammonium sulfate $(\text{NH}_4)_2\text{SO}_4$ were performed at room temperature in a sample-on-oscillator configuration. The measurements utilized our new probe with dual 3-axis piezo-driven stages for fiber interferometer and gradient magnet positioning, as well as the previously mentioned LabView-software-based control system capable of signal generation, data acquisition, and analysis. Force signals were detected with 12 μm resolution in a one-dimensional scan. Measurements of NMR relaxation times $T_2^* = 1.5 \pm 0.3$ μs, $T_2 = 44 \pm 2$ μs, and $T_1 = 5.6 \pm 0.7$ s were obtained in an 8 T magnetic field, extending the frequency range of previous measurements and revealing an unexpected frequency-dependent fluctuation spectrum at room temperature. These techniques open a window to dynamical imaging scans in materials research on single microcrystals with resolutions on the micron scale at room temperature and at sub-micron scales at lower temperatures.

5.2 Positioning Scans

In the experiment, the ammonium sulfate single crystal sample used has a relatively high proton spin density $n_H = 6.5 \times 10^{22}$ cm^{-3} and a long, nearly frequency-independent spin-lattice relaxation time ($T_1 = 3.9 - 4.4$ s for $10 - 60$ MHz), also known to be sensitive to ammonium tetrahedra dynamics [36]. The material was attached to the cantilever with Devcon 5 Minute epoxy; it also could stay attached under vacuum conditions without degradation for an extended period.

During a scan the cantilever response was monitored, each time the gradient magnet was moved, throughout the typically 200 ms during which the modulated rf field was applied. Although the rf excitation ideally has no Fourier component at the mechanical oscillator frequency, a small background signal due to induced periodic motion from the frequency-modulated rf signal can be observed as a vertical baseline offset in the scan data shown in Figure 5.1. When the resonance slice coincides with the sample position, the spin signal can be seen over the rf background signal. The two scans shown investigated both the effect of a 0.3 MHz shift in resonance frequency and the effect of the lock-in amplifier time constant τ, by looking at 346.337 MHz with $\tau = 300$ ms and at 346.037 MHz with $\tau = 30$ ms. As expected, the ~ 346.3 MHz, $\tau = 300$ ms data (circles) exhibit a lower random noise amplitude than the ~ 346.0 MHz, $\tau = 30$ ms data (crosses). More importantly, these two scans (and a variety of others) confirm the NMR nature of the force-detected signal: here, the peak has shifted approximately 80 μm for a 0.3 MHz fre-

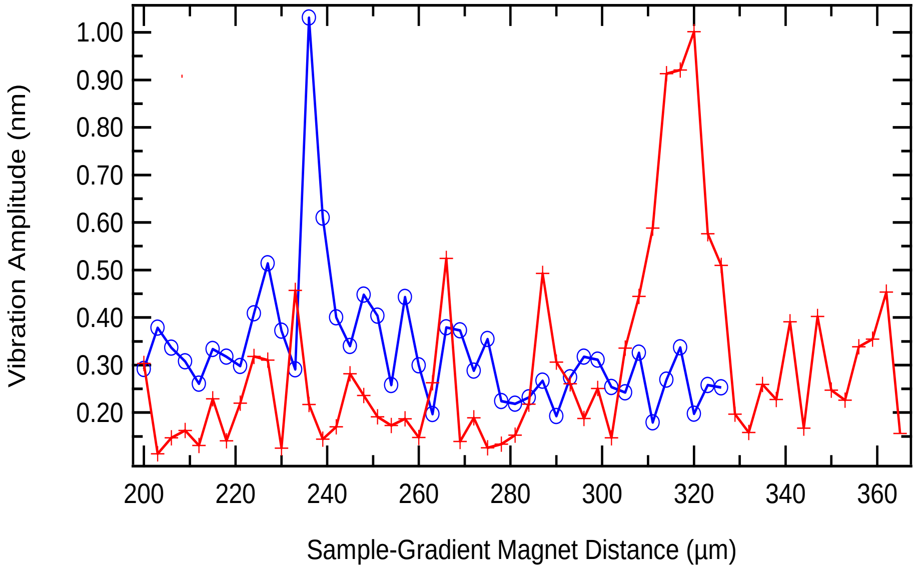

Figure 5.1: Result of two consecutive scans at 346.03MHz (crosses) and 346.33MHz (circles) showing the observed force signals over the rf artifact baselines (offset).

quency shift, which, with $\gamma \approx 42.6$ MHz/T, corresponds to a magnetic field gradient of approximately 90 T/m. For the ^{1}H nuclear Curie magnetization and our sample dimensions, a net moment of 2.2×10^{-17} J/T is expected; thus for the 90 T/m field gradient, a force of only 2.0 fN is expected. Thus we typically signal-averaged 9 to 25 times to improve signal-to-noise a factor of 3 to 5, that is, to bring this force appreciably above our noise level of $1.4 - 4.3$ fN mentioned above.

5.3 Spin Manipulation Experiments

For the subsequent experiments, the resonant slice was centered at the sample location for the Larmor frequency in use, and remained fixed there.

5.3.1 Spin Nutation

First, spin nutation experiments were performed in which the net nuclear magnetic moment is tilted away from the z axis by a variable angle θ with pulses at the Larmor frequency ω_0 of different durations τ_p; the angle of nutation is described by Equation (2.19). The expected spin signal was fitted to a damped sinusoidal function with an offset value as described by

$$A = e^{(-\tau_p/\tau)} \cdot \cos(\gamma B_1 \cdot \tau_p) + b. \tag{5.1}$$

Figure 5.2 shows two nutation-experiment plots with different lock-in amplifier time constants. The period obtained from these Rabi oscillations corresponds to $T_{Rabi} = 7.2$ μs, and with, $\theta = \omega_1 t = \gamma B_1 t$, Equation (2.19), we thus determine an rf field amplitude of $B_1 = 33$ gauss.

Once the magnitude of B_1 is known, it is possible to control with relatively good precision the orientation of the magnetization. This control then permits the possibility of performing dynamical measurements on our sample. Another advantage of knowing the rotating rf field is that maintaining the experiment within the CAI limit is no longer estimated and the maximum amplitude of frequency modulation can be exploited. In our particular case, 33 G corresponds to a limiting amplitude of frequency modulation of $\Omega = 200$

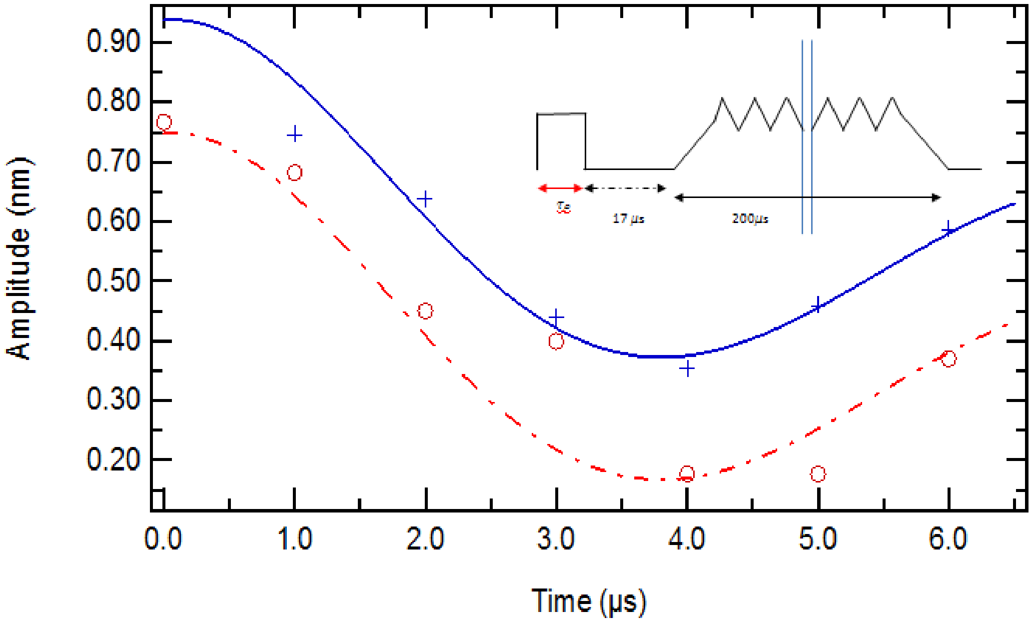

Figure 5.2: Nutation experimental data (nuclear magnetic moment, measured by the cantilever amplitude, as a function of nutation pulse length τ_p) at 346.2 MHz and fits to Eq. (5.1) using two different lock-in amplifier time constants; $\tau = 30$ ms (crosses and solid line) and $\tau = 300$ ms (circles and dash-dot line). Inset: rf frequency modulation pattern used to tilt (during τ_p) and measure (cyclic adiabatic inversion after τ_p) the spin orientation.

kHz to safely avoid non-adiabatic effects (using a conservative adiabaticity factor of 10).

5.3.2 Spin Echo

Next, spin-echo measurements at room temperature were performed with $\pi/2 = 1.8$ μs and $\pi = 3.6$ μs pulses for $B_1 = 33$ G. First a $\pi/2$ pulse was applied to set the magnetic field in the x–y plane. The inhomogeneity of the magnetic field in the ammonium sulfate will destroy the net magnetization M_0 in an unknown dephasing time T_2^*. Next, the application of a π pulse at, say, time $\tau_{1-2} = 20$ μs after the first pulse will invert all the spins and set the system toward a rephasing state, the spin echo. Since NMRFM typically measures only the magnetization along the z axis, a third pulse (a second $\pi/2$ pulse) at time τ_{2-3} after the π pulse will shift the remaining magnetization from the $x - y$ plane back to the z axis for sampling. By changing the length of τ_{2-3} before the CAI modulation is used to sample the magnetization, observation of the instantaneous state of the magnetization is possible, as is shown in Figure 5.3. The data show a maximum of the spin echo when $\tau_{1-2} = \tau_{2-3} = 20.5 \pm 0.3$ μs. The half-width at half-maximum (HWHM) of a gaussian fit of the echo is a measure of the time T_2^* that it takes for the magnetization to be appreciably destroyed (the free induction decay time) or reconstructed; our data indicate $T_2^* = 1.5 \pm 0.3$ μs. This time corresponds to a total linewidth of $\Delta B = 1/(\gamma T_2^*) \approx 25 \pm 5$ G.

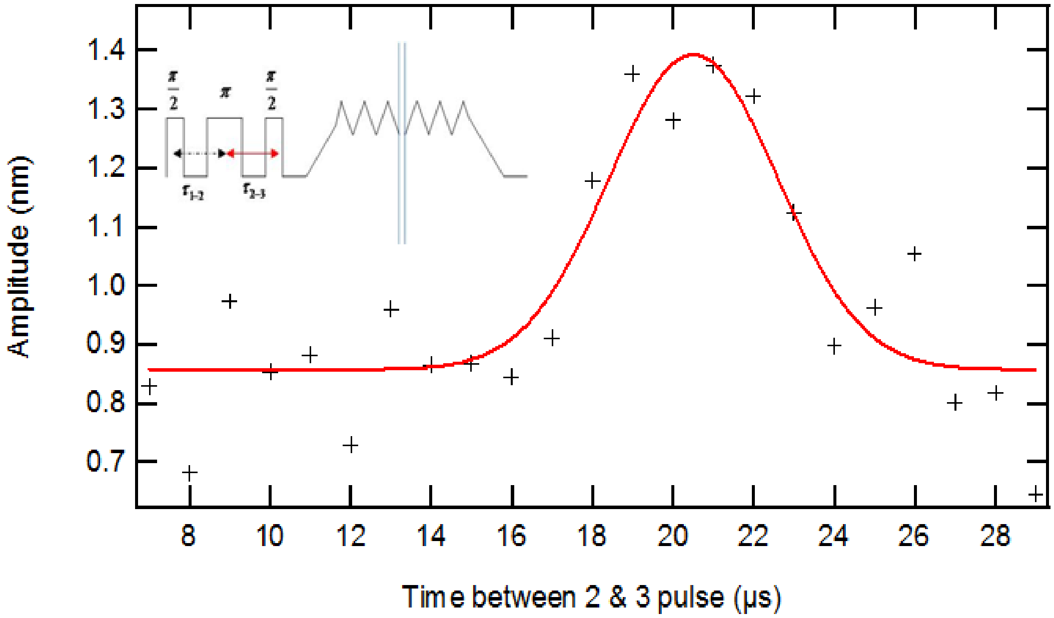

Figure 5.3: Spin-echo measurement fitted to a gaussian curve. Inset shows the rf modulation pattern used. $\tau_{1-2} = 20\mu$s. The time τ_{2-3} is increased in intervals of 1 microsecond.

5.3.3 Spin-Spin relaxation time T_2

The determination of the spin-spin relaxation time T_2 is readily performed by a measurement of the decay in amplitude of spin echoes as we increase the value of the pulse spacing above, that is, for variable $\tau_{1-2} = \tau_{2-3} = \tau_a$. Since these points are obtained when the magnetization has rephased, that is, when the effect of the inhomogeneous fields has been overcome, the decay in this signal is from homogeneous broadenings, here mainly due to the dipole-dipole interaction between proton spins. The results of this experiment, for time τ_a between both $\pi/2 - \pi$ and $\pi - \pi/2$ pulses, increased by the same amount, are shown in Figure 5.4; such data are expected to decay with a characteristic time T_2 and a function of the total time increment $2 \cdot \tau_a$ as described by Equation (5.2):

$$\frac{M(t)}{M(0)} = e^{-\left[\frac{2\tau_a}{T_2}\right]^2} \tag{5.2}$$

To obtain the spin-spin relaxation time, we performed a linear fit to the natural logarithm of Equation (5.2), i.e., by assuming a gaussian decay of the magnetization. We obtained a spin-spin relaxation time $T_2 = 44 \pm 2$ μs.

Since we have measurements of both T_2 and T_2^*, we can calculate the inhomogeneity of the magnetic field inside the sample described by Equation (5.3) [10]:

$$\frac{1}{T_2^*} = \frac{1}{T_2} + \gamma \cdot \Delta B_0 \tag{5.3}$$

Our measurements of ^{1}H T_2 and T_2^* provide a value of the field inhomogeneity of $\Delta B_0 = 24 \pm 5$ G; thus the linewidth $\Delta B = 25 \pm 5$ G obtained

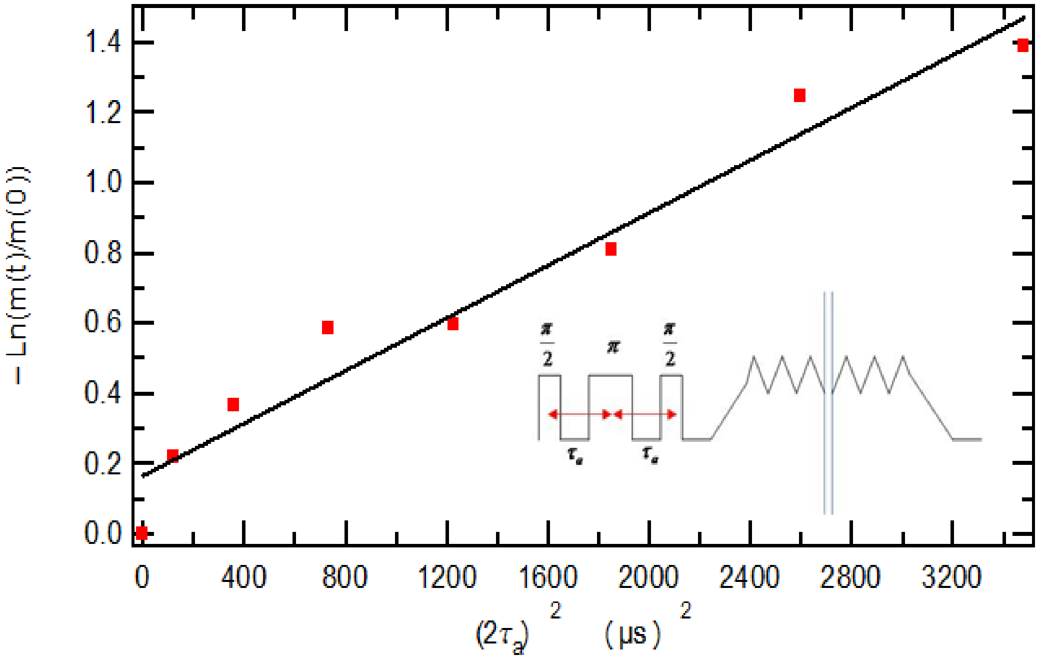

Figure 5.4: Spin-Spin interaction measurements and linear fit. Inset describes the rf protocol used for measurements. Both red (continuous) arrows shows the variables used to perform the measurements.

above is dominated by inhomogeneous broadening, as is also evident from the relative magnitudes of T_2 and T_2^*. Such a large inhomogeneity is consistent with the large applied field gradient of the permalloy-wire gradient magnet.

5.3.4 Spin-lattice relaxation time T_1

Finally, our last experiment focuses on the observation of the properties of the spin-lattice relaxation time T_1 of protons in single-crystal ammonium sulfate at room temperature at 346 MHz. In the high-temperature paraelectric phase of ammonium sulfate (above 236 K), the ammonium tetrahedra are rapidly re-orienting so that rapid, random motion-modulated dipole-dipole interactions are expected to dominate the T_1 relaxation. The spectral density of sufficiently rapidly fluctuating interactions is flat, that is, independent of frequency, and has been modeled [Ref. [36], Figure 2] to be frequency-independent above about 40 MHz, with $T_1 = 4.3 \pm 0.1$ s.

To measure the spin-lattice relaxation time T_1, first we destroy the net magnetization using a train of $\pi/2$ pulses with a time between them greater than T_2, as seen in the bottom right inset of Figure 5.5; here, we use $\tau_a = 100$ μs. With time, the magnetic moment gradually recovers along the z axis, which involves T_1 (energy-exchange) processes. This can be seen in the top inset where each point represents the value of the magnetization at different times. A fit was performed by assuming that the nuclear spin magnetic moment behaves as

$$\frac{M(t)}{M(\infty)} = \left(1 - e^{-\frac{t}{T_1}}\right) \tag{5.4}$$

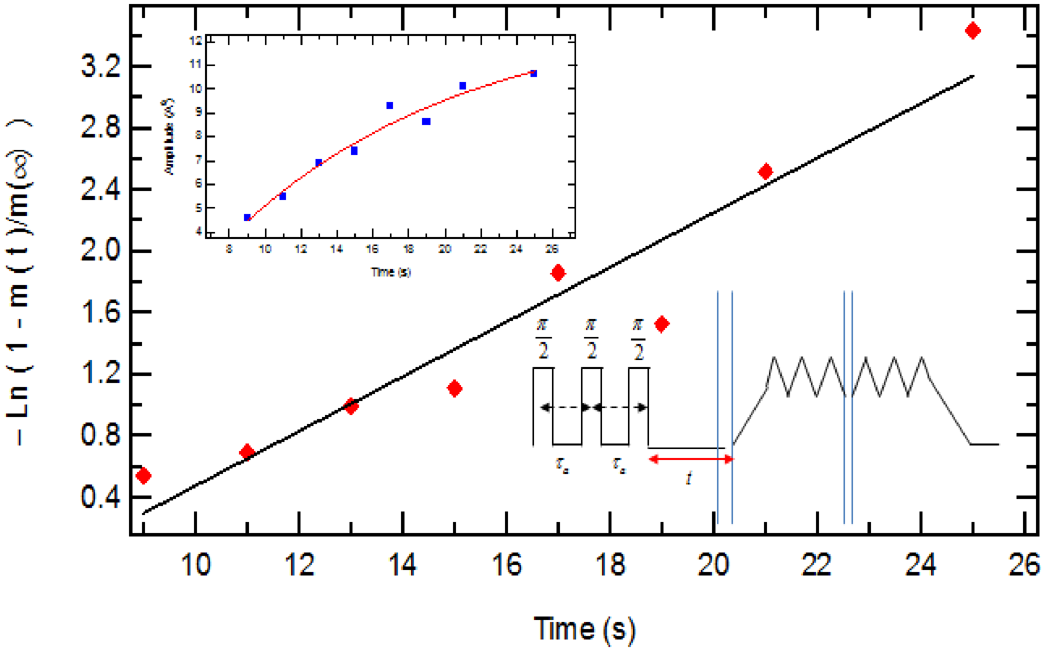

Figure 5.5: Spin-lattice relaxation measurements and linear fit to an exponential recovery. Bottom inset: the rf protocol used for the measurements, where the red (continuous) lower arrow is the variable time delay after destroying the magnetization, before CAI measurements. Top inset: the net magnetization recovered at different times after the net magnetization has been destroyed.

The resulting fit, shown in Figure 5.5, gives a value of the spin-lattice relaxation time of $T_1 = 5.6 \pm 0.7$ sec. This time is appreciably longer than the assumed frequency-independent value $T_1 = 4.3 \pm 0.1$ s modeling the behavior of T_1 above 40 MHz in Ref. [36]. This result suggests that the motion-modulated dipolar interactions due to rapidly re-orienting ammonium tetrahedra do not have the presumed single exponential correlation time previously used to model the data, perhaps due to the constrained motion. In fact, a careful examination of the data of Figure 2 in Ref. [36] reveal a slow, nearly linear increase in T_1 throughout the range $10-50$ MHz, a linear extrapolation of which is consistent with the value $T_1 = 5.6$ s at 346 MHz found here.

5.4 Conclusions

Measurements of ^{1}H NMR properties in single-crystal ammonium sulfate with NMRFM techniques have been achieved with a new microscope and software system that has proven both reliable and flexible. These microcrystal NMRFM results provide promising micron-scale resolution even at room temperature. Beyond simple detection, measurements of dynamical properties were performed, and the values of the various nuclear spin relaxation times obtained: $T_2^* = 1.5 \pm 0.3$ μs, $T_2 = 44 \pm 2$ μs, and $T_1 = 5.6 \pm 0.7$ s. The first measurement shows that gradient-magnet inhomogeneity dominates the linewidth, with $\Delta B = 25 \pm 5$ G. The T_2 measurement directly probes the nuclear dipole-dipole interactions, and provides a value of the second moment, $M^2 = (1/(\gamma T_2))^2 = 0.71$ G^2 at room temperature, which can be used to compare different models of ammonium tetrahedral rotations [37]. The new T_1 data here indicate that a simple BPP theory with a single correlation time may not be appropriate for this material. Even at such high temperature, T_1 increases with frequency, or conversely, the longitudinal relaxation rate decreases with increasing frequency. This nearly $1/f$ contribution to the relaxation rate behaviour is reminiscent of processes with a distribution of correlation times, where several (or many) lorentzian $1/f^2$ tails sum to produce interesting, $1/f$-like behaviour.

Chapter 6

Summary and Future Work

6.1 Summary

This dissertation has been written with the intention of becoming a guide to performing NMRFM with a fully developed probe and control station. An introduction describing the history and achievements behind NMRFM was given in Chapter 1. Also, the results obtained during our experiments were listed and briefly described.

In Chapter 2, the principles of magnetic resonance were described and explained. First, the behavior of magnetic moments submerged in a magnetic field was described in detail, particularly the population differences due to Boltzmann polarization. Second, spin manipulation and relaxation effects were portrayed, finishing with the Bloch Equations as a mathematical description of the microscopic and macroscopic behavior of the spins.

Chapter 3, focused on the theoretical aspects of nuclear magnetic resonance force microscopy. It contained a detailed description of the physical phenomena of magnetization, the gradient magnet, and mechanical oscillators. It also depicted in detail magnetic modulation techniques, from ones already used to some other novel ones that we are currently implementing.

Finally the cantilever sensitivity and the most common sources of noise were covered, finishing with the description of the signal-to-noise ratio (SNR) and its dependence on several variables.

After the theory, the physical components of the system were explained, as well as how the design, geometry and orientations are used in this state-of-art NMRFM system. One by one, the variable temperature probe, the fiber-optic interferometer, the cantilever, the gradient magnet and the rf coil were described. Chapter 4 also includes information on the new control system used for positioning control, rf generation, and data acquisition that has proven to be very successful.

Chapter 5 is a trip through the measurements obtained during my experiments. Force measurements of around 2 fN were obtained with a SNR of 5 in a 12-μm-thickness resonance slice in the z direction. Once the resonance is aligned with the sample, spin nutation measurements were performed, and spin-echos were observed, resulting in a measurement of the rotating magnetic field of $B_1 = 33$ gauss and a magnetic field inhomogneity of 25 G. Finally, dynamical measurements of nuclear spins in ammonium sulfate were obtained, resulting in the determination of spin-spin and spin-lattice relaxation times of 44 ± 2 μs and 5.6 ± 0.7 s respectively.

Finally, some conclusion regarding the results were provided. Overall a step forward into our capabilities of performing dynamical NMRFM measurements has been achieved.

6.2 Future Work

6.2.1 Sawtooth with AM and FM Experiments

In the past years the capability of performing dynamical measurements and applying new modulation techniques in NMRFM has become a reality in our lab. Now that the design of new sequences and modulation techniques have been enabled, we can focus more on the physics and less on the engineering parts of the experiments. Still more work is necessary if higher sensitivity is desired, but detailed studies of micrometer sized samples at room temperature can now be performed and better resolution at low temperatures obtained.

Now, amplitude-modulation synchronized with frequency modulation, as used in the sawtooth continuous-wave technique discussed in Section 3.3.2, is available in our lab. Some sawtooth or similar experiments already demonstrated the success of this technique [15], [16], [17], [18], [19] and [20]. Since our NMRFM system has a different method for generating continuous waves, a new technique described in Section 4.3 has been developed to synchronize FM and AM. Our imminent future work is to perform NMRFM measurements with this type of FM, AM combination in a sawtooth wave. This arrangement should allowed us to use more sensitive cantilevers, avoiding undesired artifact effects during modulation. More sensitive measurements and higher resolution experiments can now be performed in which the limit in sensitivity is the cantilever's thermal noise.

6.2.2 NMRFM in Liquid Samples

A second NMRFM probe designed to be used in a 1-tesla magnetic field has also been built. This probe uses the same principles as the one described in this dissertation, including stages, signal generator, and the data acquisition and control system. However, the cantilever now is aligned with the field, the gradient magnet is attached to the cantilever, and samples in the liquid state are attached to the stages.

Our first experments are designed to measure liquid samples with different concentrations of para magnetic impurities. Three microtubes, one with pure water and other two with two different concentrations of copper sulphate (0.01 M and 0.003 M), are attached together parallel to each other. The same magnetic forces are expected to be obtained for each concentration, but differences in T_1 will allow us to differentiate one sample from the others. This experiment is a preamble to a more ambitious one, in which NMRFM measurements of blood, plasma, or organic samples under ambient conditions can be performed.

6.2.3 NMRFM Using IMANES

Achieving measurements in NMRFM without having to fulfil the Cyclic Adiabatic Inversion condition could bring this technique to a new level in which high-frequency cantilevers can be used, with no limitation on the amplitude of the frequency modulation involved, and small or zero artifact effects. If all these conditions can be accomplished, NMRFM with atomic resolution could be achieved as a combination of MRI and AFM. Thanks to the new signal generator system, the IMANES technique will be tested and, if positive results are obtained, the best of the three types of modulations proposed will be studied as will the possibility of using higher resonance-frequency cantilevers.

Appendices

Appendix A

Software

A.1 Driven Frequency Scan

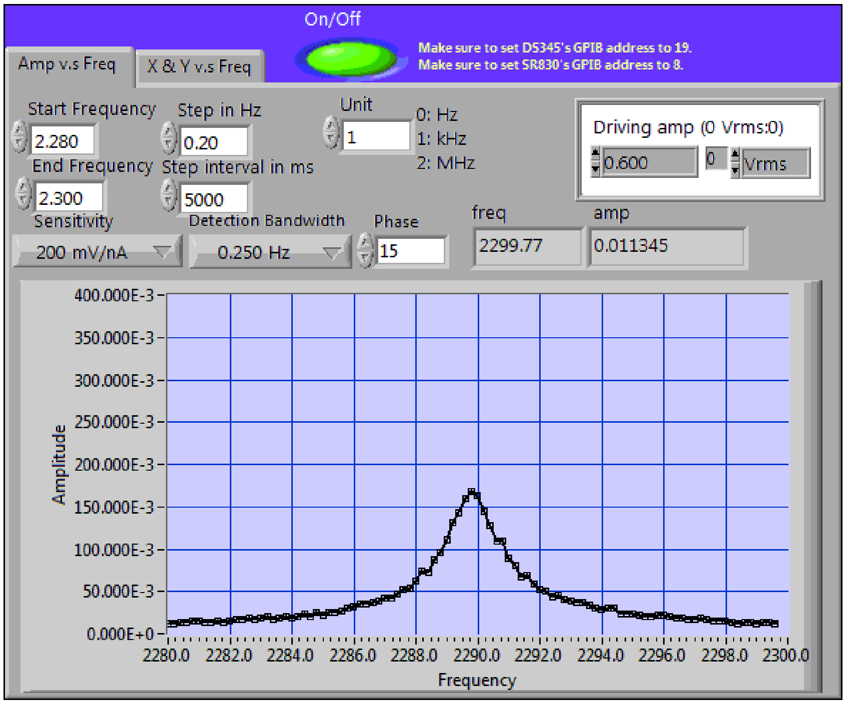

Make sure to set DS345's GPIB address to 19.
Make sure to set SR830's GPIB address to 8.

Start Frequency: 2.280
End Frequency: 2.300
Step in Hz: 0.20
Step interval in ms: 5000
Unit: 1
0: Hz
1: kHz
2: MHz
Driving amp (0 Vrms:0): 0.600 0 Vrms
Sensitivity: 200 mV/nA
Detection Bandwidth: 0.250 Hz
Phase: 15
freq: 2299.77
amp: 0.011345

Figure A.1: Control software to perform driven frequency scans of cantilevers.

The cantilever characteristics, Q, k, and ω_c, play an important role in the values that the variables Ω, F_{min}, Δz and SNR will have. To determine the parameters that will dictate the limits of the experiment, accurate characterization of the cantilever is necessary. With this purpose, driven frequency scans are used to obtain the resonance frequency, the quality factor and also set the phase of the lock-in amplifier. During the frequency scans, the cantilever is driven by a piezo plate, and the parameters of the signal generator, DS 345, and of the Lock-in Amplifier, SR 830, are controlled with the software all of the time.

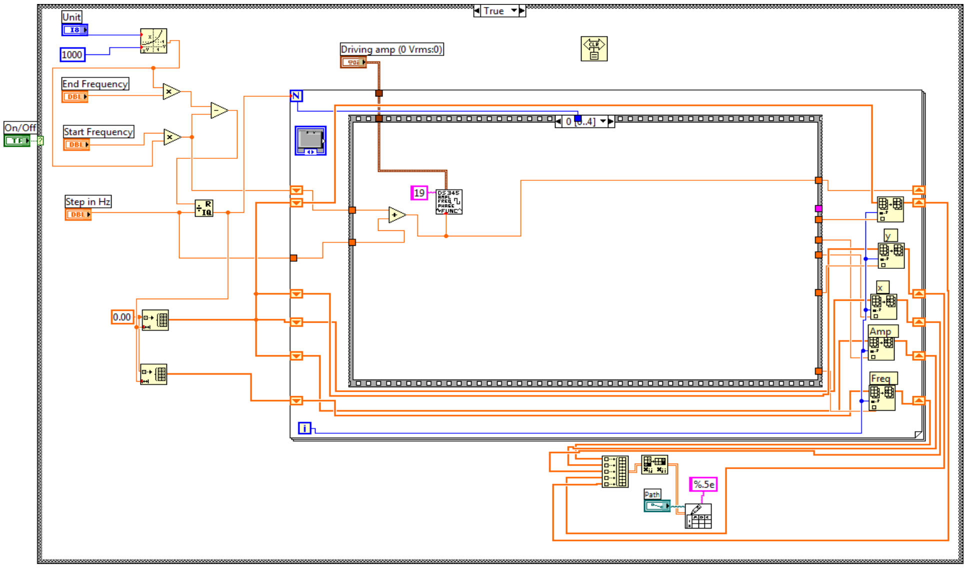

Figure A.2: Control software diagram with the settings of the driven frequency scan, and the DS 345 function generator.

Figure A.1 is an image of the control panel of our program, freq scan FRXYPPhase. Two tabs in the software can be seen here, where: Amp v.s. Freq tab shows the R values at each frequency, and X & Y v.s. Freq tag, shows a graphical representation of the in-phase and quadrature channels measured. It also shows the control parameters of the sensitivity, the detection bandwidth and the phase settings of the lock-in amplifier that will be used during the scans.

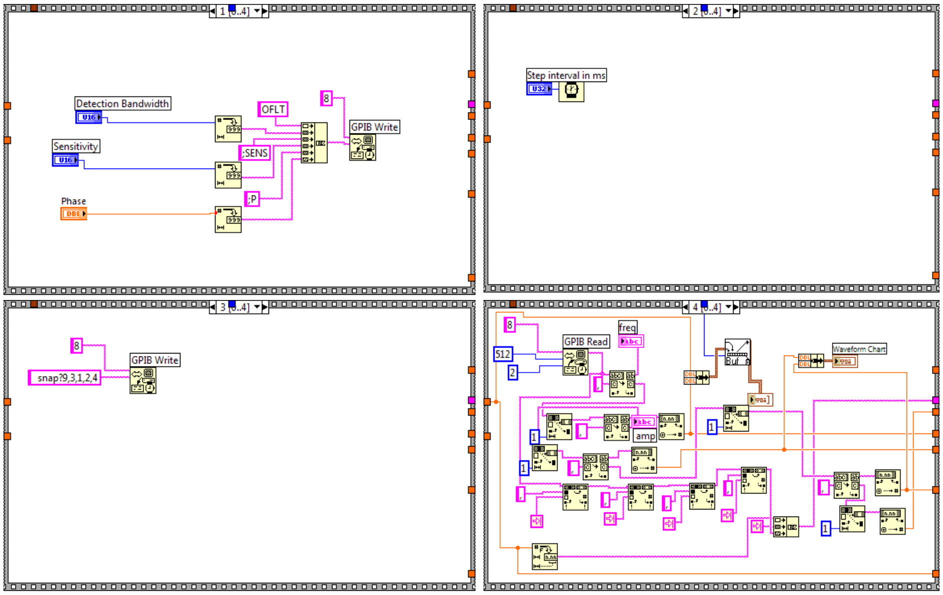

Figure A.3: Four components of the stack sequence structure.

Figure A.2, shows the parameter settings of the amplitude and the frequency, and also the stack sequence structure, 0[0..4], that contains the vi program used to communicate with the DS 345. Figure A.3 shows the other four parts of the stack sequence structure. 1[0..4] set the values of the lock-in amplifier SR 830. 2[0..4] makes the system wait for the DS 345 and SR 830 to reach the new values. The stack sequence structure 3[0..4] tells the lock-in to send the values R, X, Y and phase of specific measurement to the PC and finally 3[0..4] organizes the values obtained to set a corresponding frequency with the measured values.

A.2 Power Spectrum

To obtain the value of k it is necessary to use a different approach than the driven frequency scan. As described in Section 4.1.3.2, using FFT measurements we can obtain the cantilever's noise power spectrum and later, calculate its spring constant. To obtain this value a new software has been designed to take advantage of the full capabilities of the DAQ card. Figure A.4, shows the control panel of the program Amplitude Spectrum from the DAQ card. The DS 345 sets the value of the center frequency at which the SR 830 will be measuring, and the lock-in amplifier sets the detection bandwidth and sensitivity. The sample rate and sample duration are controlled by setting directly the parameters of the DAQ card.

Figure A.5 contains the settings for the oscilloscope, the DS 345 and the SR 830. Simultaneously the microscope temperature is measured, using a Conductus temperature controller calibrated for a Cernox CU - Copper bobbin (small, 4-lead) from Lakeshore, and averaged 1000 times. Inside the stack sequence structure 0[0..6], the center frequency is sent to the DS 345.

Figure A.6 shows the next 4 processes of the software. The stack sequence structure 1[0..6] makes the program wait, 2[0..6] sends information of the chosen parameters to the lock-in amplifier, 3[0..6] tells the system to start the time series measurement and 4[0..6] makes the system wait for 1 second.

Figure A.7 shows the stack sequence structure 5[0..6]. Here, the Linear average program reads the time series measurements from the oscilloscope and

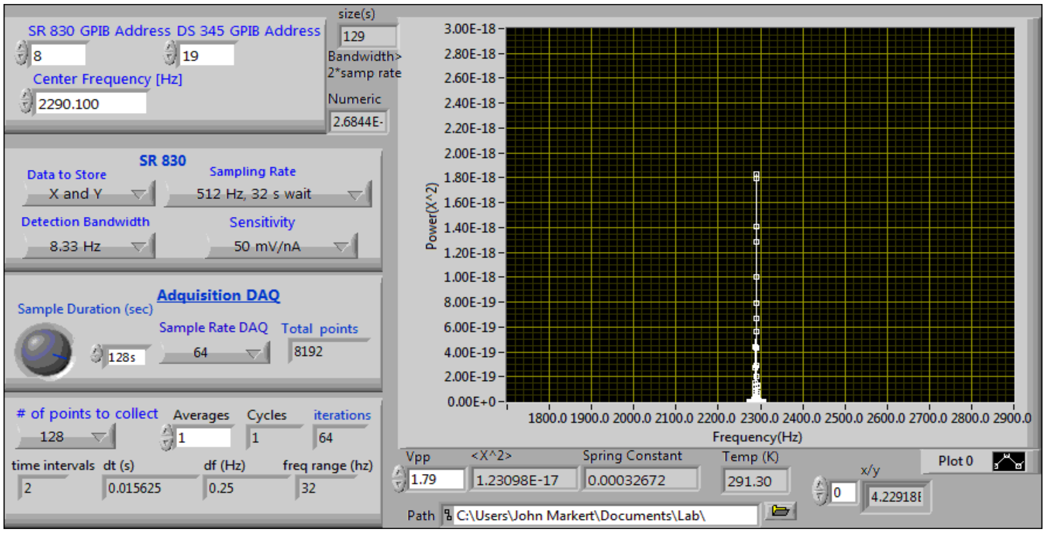

SR 830 GPIB Address: 8
DS 345 GPIB Address: 19
Center Frequency [Hz]: 2290.100
size(s): 129
Bandwidth> 2*samp rate
Numeric: 2.6844E-

SR 830
Data to Store: X and Y
Sampling Rate: 512 Hz, 32 s wait
Detection Bandwidth: 8.33 Hz
Sensitivity: 50 mV/nA

Adquisition DAQ
Sample Duration (sec): 128s
Sample Rate DAQ: 64
Total points: 8192

# of points to collect: 128
Averages: 1
Cycles: 1
iterations: 64
time intervals: 2
dt (s): 0.015625
df (Hz): 0.25
freq range (hz): 32

Vpp: 1.79
<X^2>: 1.23098E-17
Spring Constant: 0.00032672
Temp (K): 291.30
x/y: 0 4.22918E
Path: C:\Users\John Markert\Documents\Lab\

Figure A.4: Control software to perform FFT and obtain the cantilever's noise power spectrum. Given the V_{pp} and temperature, the program calculates automatically the spring constant.

sends it to a For loop to divide the time series in N intervals. Fourier transformations of each set of data are performed and the average of each value is calculated. In case the results obtained are very noisy, there is the possibility to repeat this measurement as many times as necessary for averaging purposes. Finally in 6[0..6], Figure A.8, is shown in the section in which data and frequency are aligned in a For loop and plotted as the noise power spectrum. Secondly, the integral of the noise power spectrum, gives $\langle x^2 \rangle$ and using the temperature measured and the Equipartition Theorem k is calculated.

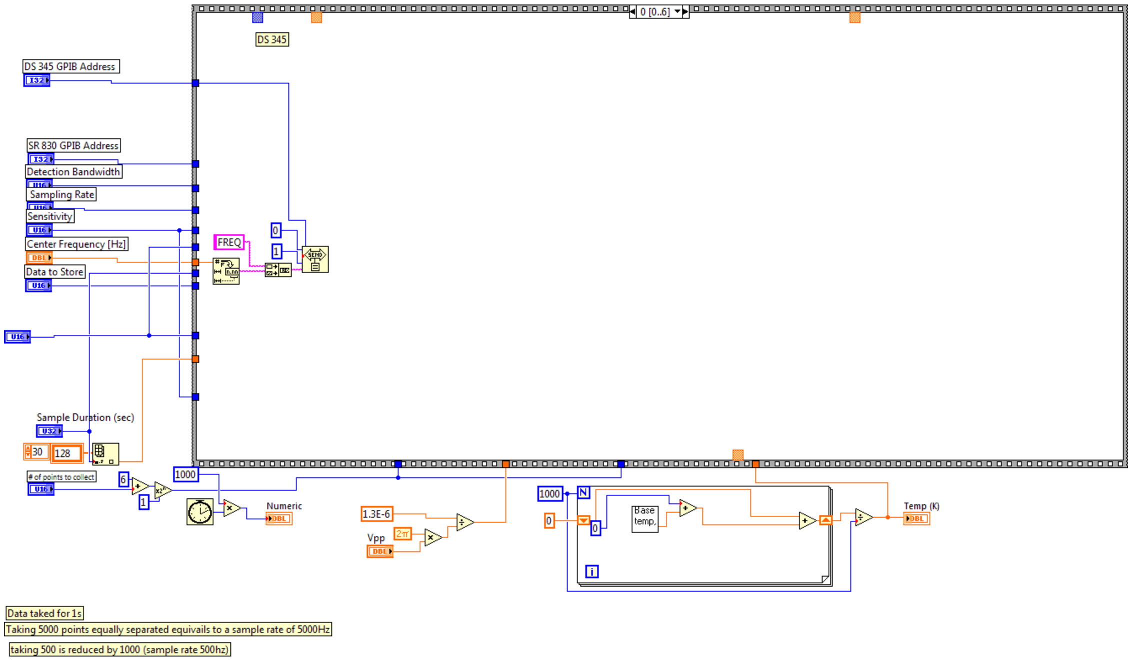

Figure A.5: Block diagram showing the stack sequence structure 0[0..6].

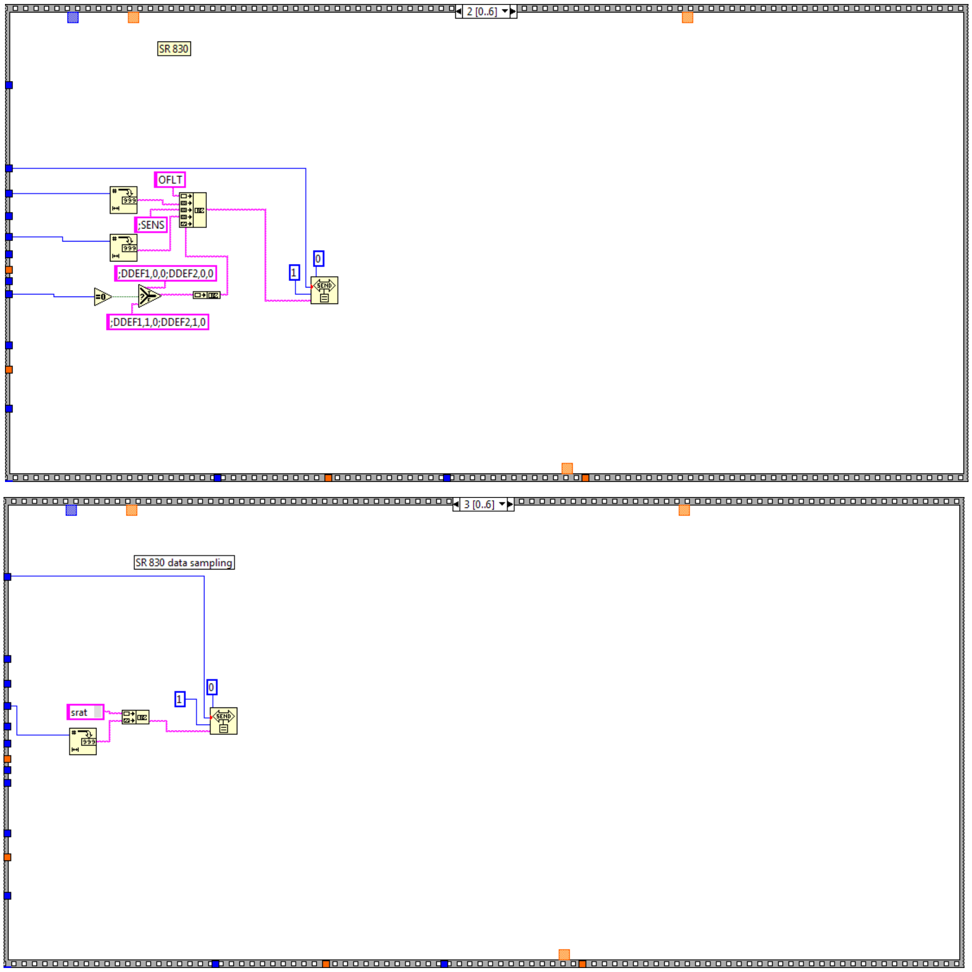

Figure A.6: Block diagram showing the stack sequence structure 1[0..6] to 4[0..6].

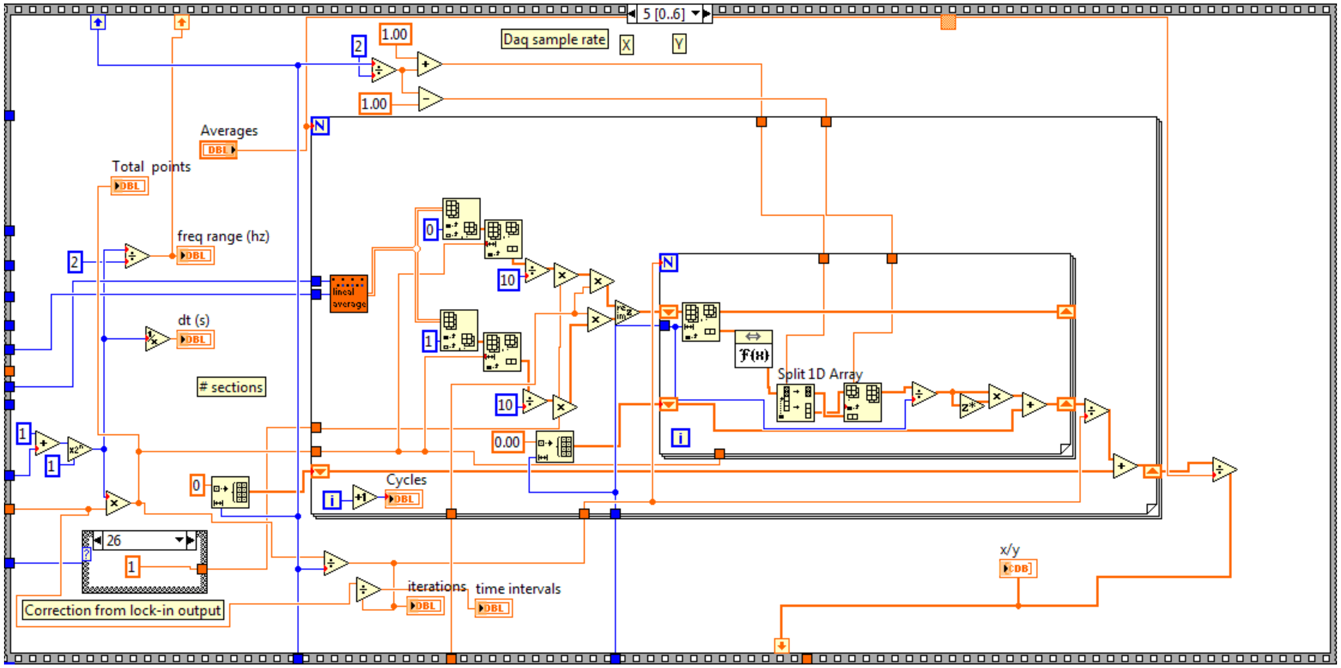

Figure A.7: Block Diagram showing the stack sequence structure 5[0..6]. Linear average program reads the time series measurements from the oscilloscope. Inside the for loop the Fourier transformation of the data takes place.

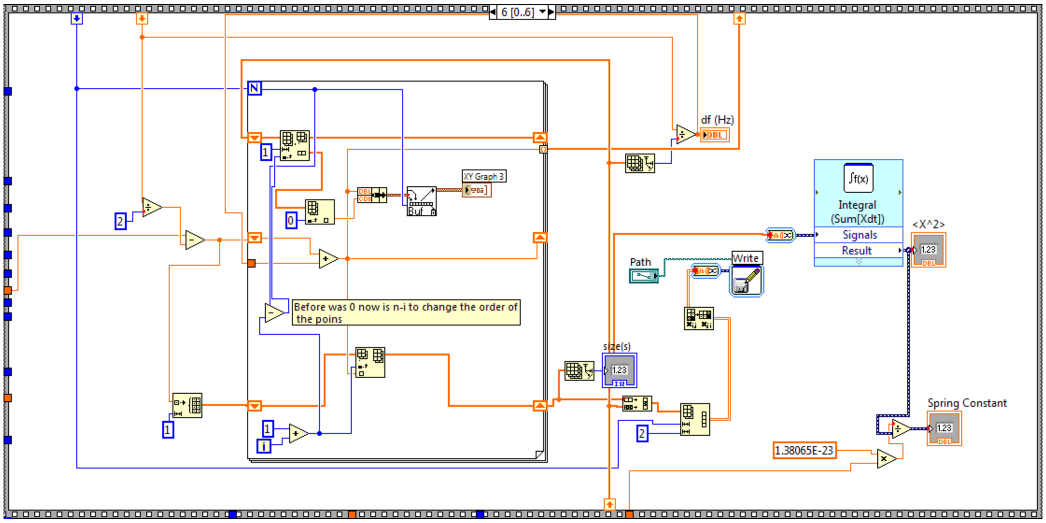

Figure A.8: Block Diagram showing the stack sequence structure 6[0..6]. The results are aligned with its corresponding frequency, buffered and plotted as a noise power spectrum. Integral of the results give $\langle x^2 \rangle$ and the Equipartition Theorem is used to obtain k.

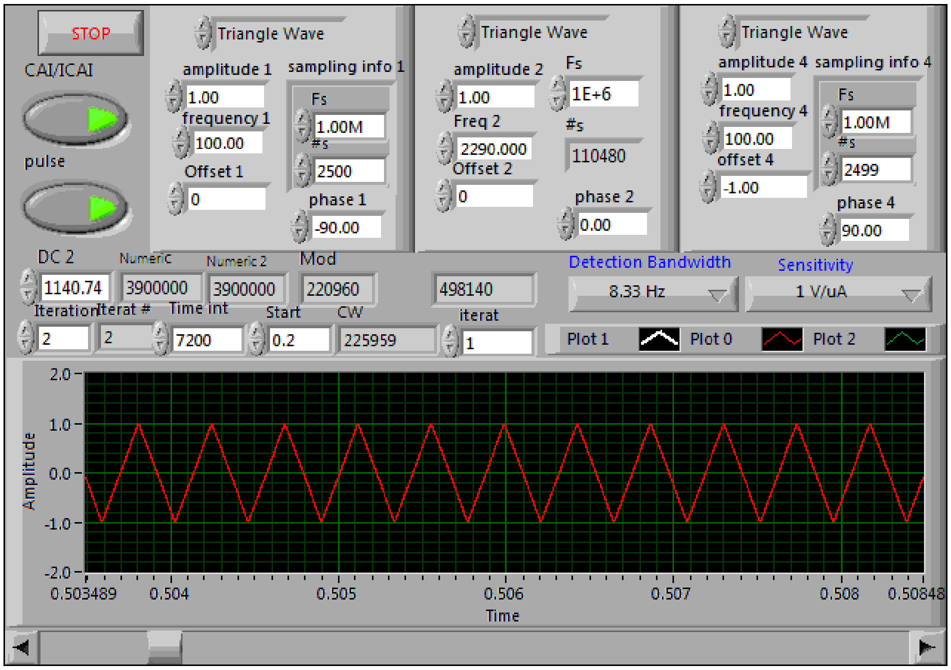

Triangle Wave
amplitude 1: 1.00
frequency 1: 100.00
Offset 1: 0
sampling info 1: Fs 1.00M, #s 2500
phase 1: -90.00

Triangle Wave
amplitude 2: 1.00
Freq 2: 2290.000
Offset 2: 0
Fs: 1E+6
#s: 110480
phase 2: 0.00

Triangle Wave
amplitude 4: 1.00
frequency 4: 100.00
offset 4: -1.00
sampling info 4: Fs 1.00M, #s 2499
phase 4: 90.00

DC 2: 1140.74
Numeric: 3900000
Numeric 2: 3900000
Mod: 220960
498140
Detection Bandwidth: 8.33 Hz
Sensitivity: 1 V/uA
Iteration: 2
Iterat #: 2
Time int: 7200
Start: 0.2
CW: 225959
iterat: 1

Figure A.9: Control software to perform triangular frequency modulation.

A.3 Signal Generator ICAI 105

The Icai 105 program gives shape to the frequency modulation of the carrier frequency, that will couple the force to the cantilever at its resonant frequency. Figure A.9 is an image of the control panel that controls the rf gate, the FM and the AM. In the control panel, the pulse button selects if the generated signal is going to be sent (bright green), or if only the results are shown in the graph (dark green). The CAI/ICAI button has the option to close or not close the rf gate for half of a period at the middle of the modulated wave (dark green). The first triangle wave cluster is responsible for bringing B_{eff} to the $x' - y'$ plane. The second triangle wave cluster is responsible for coupling the nuclear moment with the cantilever at its resonant frequency. Finally, the third triangle wave returns the magnetization to the z axis. The detection bandwidth and sensitivity controls set the acquisition parameters of the lock-in amplifier during the measurements. The control DC2 is used to synchronize the phase of the modulated wave with the lock-in. The iteration control indicates how many times the continuous wave will be applied, and the time interval indicates the time between repetitions. The start control sets the time delay between the rf gate opening and the beginning of the modulation. Finally, the iterations control sets how many times a section of the continuous wave is repeated to control the length of the modulation.

Figure A.10, shows the stack sequence structure 0[0..2], in which the settings of the lock-in and the signal generator are determined.

Figure A.11, shows the stack sequence structure 1[0..2] where the digital

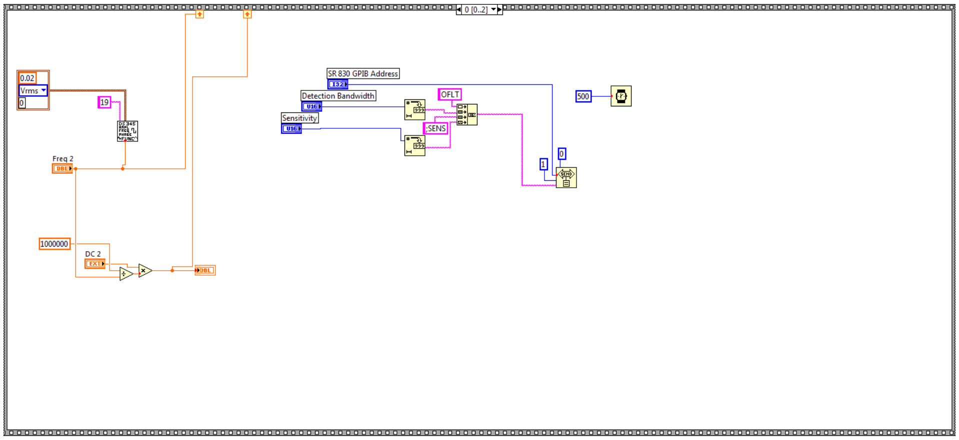

Figure A.10: Diagram of 0[0..2] setting the values of the SR 830 and DS 345.

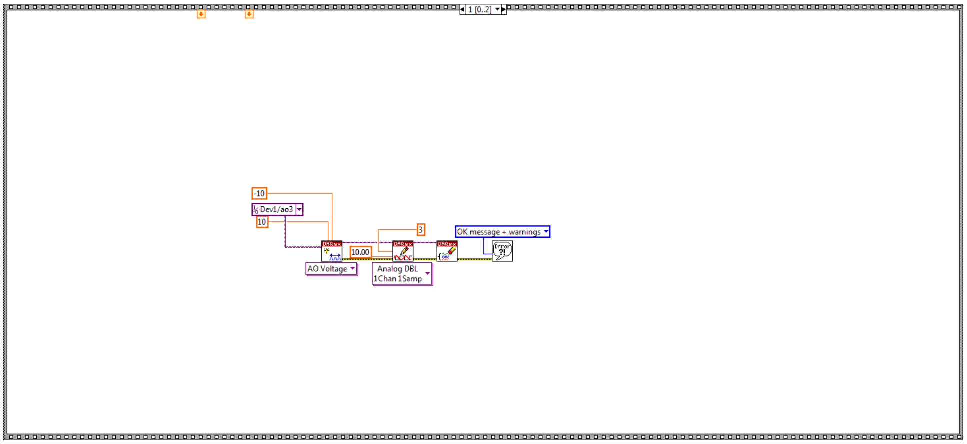

Figure A.11: Diagram of 1[0..2]. It turns on the digital switches.

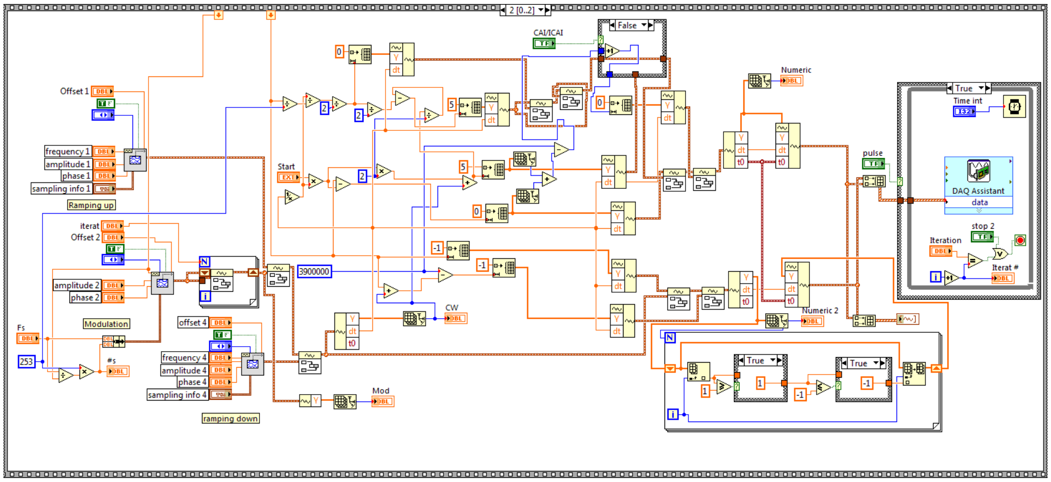

Figure A.12: Diagram of 2[0..2]. Creation of the modulated signal with a maximum output of 1 V.

switches are turned on, to direct the FM, AM and rf gate triggers through the channels connected to the signal generator, the voltage attenuator and the rf gate.

Figure A.12, shows the stack sequence structure 2[0..2], in which the three triangular signals are generated, and the modulation is sent into a For loop to control its length. The rf gate trigger measures the length of the pulse and extends it, on both sides, by a quantity indicated in the start box shown in Figure A.9. Once the FM is generated, two case structures in a For loop set the voltage limits for the triangular wave. In cases where the designed signal has a higher amplitude than the limit, the wave is chopped at the top and bottom. Finally, when the waves are fully designed and synchronized, they are sent into the DAQ Assistant to be transformed into analog output signals.

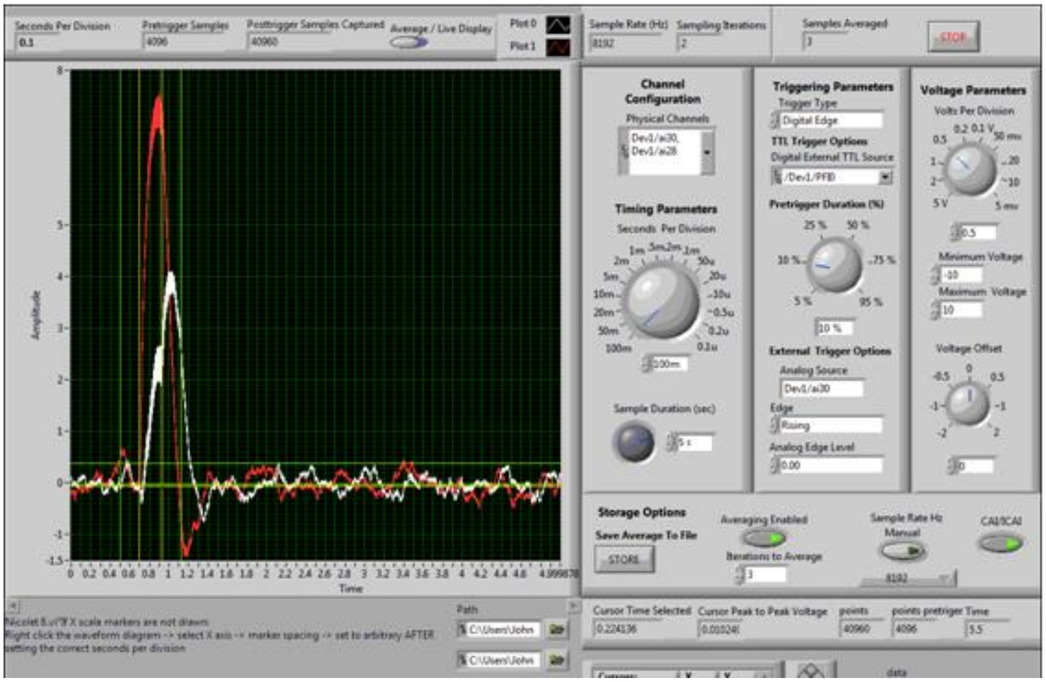

Seconds Per Division: 0.1
Pretrigger Samples: 4096
Posttrigger Samples Captured: 40960
Sample Rate (Hz): 8192
Sampling Iterations: 2
Samples Averaged: 3
Physical Channels: Dev1/ai30, Dev1/ai28
Trigger Type: Digital Edge
Digital External TTL Source: /Dev1/PFI0
Pretrigger Duration (%): 10 %
Seconds Per Division: 100m
Sample Duration (sec): 5 s
Analog Source: Dev1/ai30
Edge: Rising
Analog Edge Level: 0.00
Volts Per Division: 0.5
Minimum Voltage: -10
Maximum Voltage: 10
Voltage Offset: 0
Iterations to Average: 3
Sample Rate Hz Manual: 8192
Cursor Time Selected: 0.224136
Cursor Peak to Peak Voltage: 0.010240
points: 40960
points pretriger: 4096
Time: 5.5
Path: C:\Users\John
C:\Users\John

Nicolet 8.vi"If X scale markers are not drawn:
Right click the waveform diagram -> select X axis -> marker spacing -> set to arbitrary AFTER setting the correct seconds per division

Figure A.13: Control software designed to acquire data from the lock-in amplifier.

A.4 Data Acquisition

The Nicolet 12 Icai program is designed to perform time series measurements in synchronization with the modulation of the continuous wave. The rf gate triggers the oscilloscope that measures the cantilever oscillations during modulation, making the later analysis of the measurements easier. Figure A.13 shows a measurement of both channels coming from the lock-in amplifier. The system can control the length and the sample rate of the measurements. It is also capable of performing averages and storing the data in a folder indicating the order in which they were recorded.

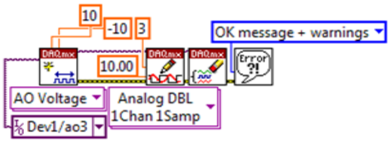

Figure A.14: Diagram of stack sequence structure 0[0..1] used to turn off a digital switch.

Figure A.15 shows the main components of the program. The data acquisition system reads the voltage from the DAQ card at a previously determined rate and for a specific interval of time. The data acquisition begins with an external trigger that can be chosen to be digital, analoge or continuous. The measurements can be averaged a defined number of times to increase the SNR. The times series is shown in a graph and can be stored in a predetermined folder for future analysis.

A.5 Data Analysis, Main Values Program

The Main Values program is designed to read one by one all the measurements recorded in a same folder by the Nicolet 12 Icai program. By indicating the V_{pp} of the interferometry laser and the lock-in sensitivity, the program transforms the data (in volts) into amplitude of oscillation. The graphical representation of the data can be customized to contain all the points or just a specific section of the measurements. The red vertical lines are indications

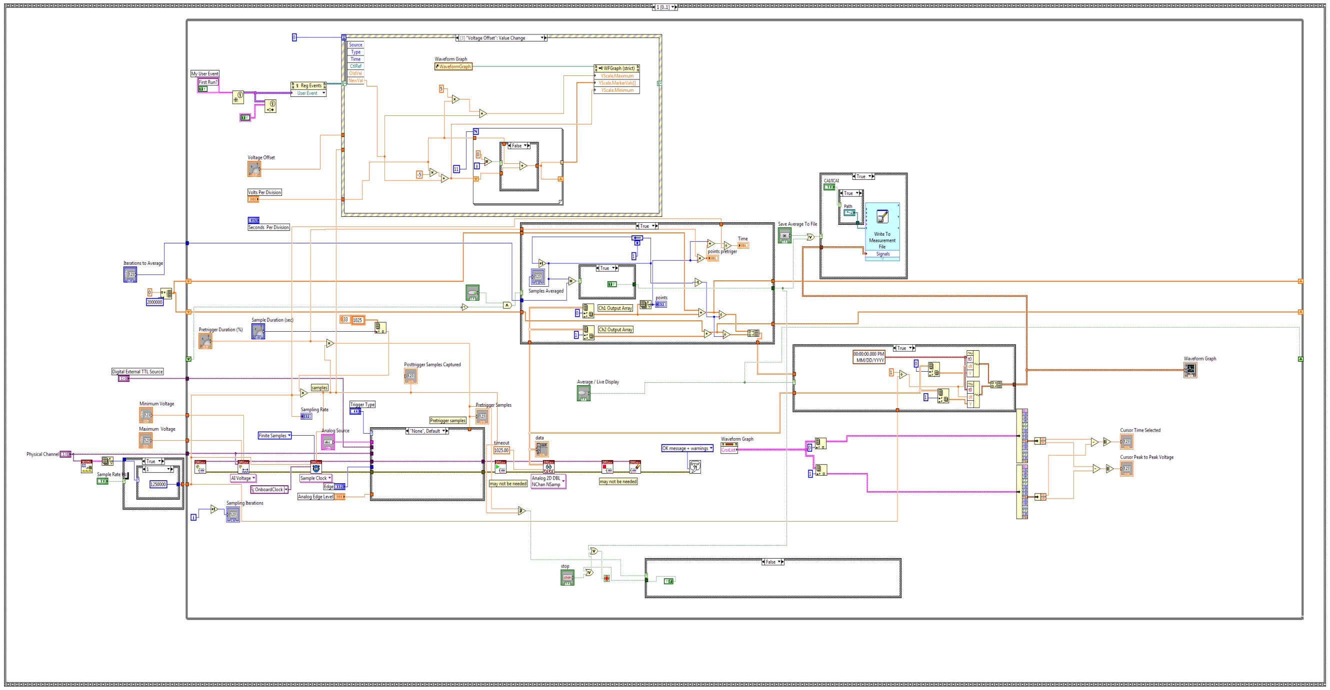

Figure A.15: Diagram of stack sequence structure 1[0..1] used to acquire, present and record the information.

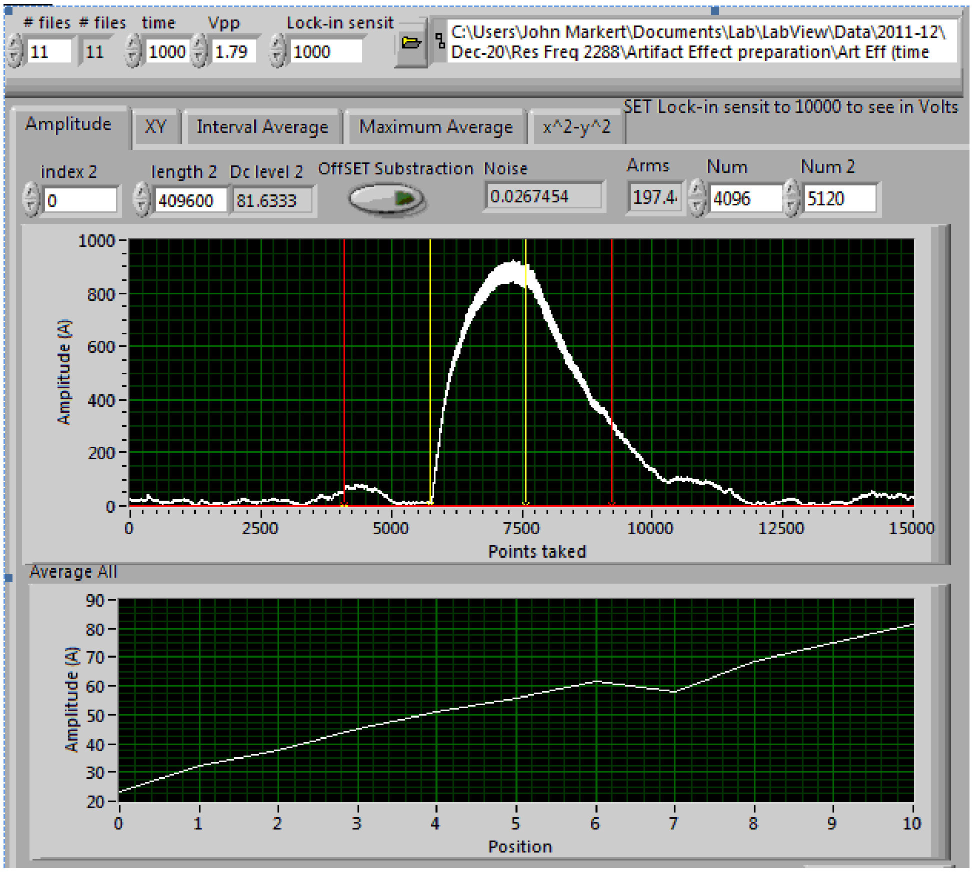
files 11
files 11
time 1000
Vpp 1.79
Lock-in sensit 1000
C:\Users\John Markert\Documents\Lab\LabView\Data\2011-12\ Dec-20\Res Freq 2288\Artifact Effect preparation\Art Eff (time
SET Lock-in sensit to 10000 to see in Volts
index 2 0
length 2 409600
Dc level 2 81.6333
Noise 0.0267454
Arms 197.4
Num 4096
Num 2 5120

Figure A.16: Control software designed to analyze all the sequences and identify the magnetic force over the artifact.

of when the rf gate is turned on and when it is off, and the yellow lines are the limits of the time length of the modulation.

The software can average an interval of points; one option is to select a specific area to be averaged and a second option is to tell the program to average an interval centered around the maximum value of the cantilever oscillation response. Storing each one of the time series measurements, during the gradient magnet positioning scan, makes it possible to obtain a graphical representation of the cantilever response as a function of the position of the cantilever.

Figure A.17 shows how the program is capable of reading sequentially all the scans recorded using a For loop, and performing five different types of graphical representations. A time interval of the file corresponding to the cantilever response to the frequency modulation is selected to analyse the cantilever response, and the rest is used to calculate the noise base line. The results for each one of the files (base line, average amplitude and maximum amplitude) are stored in memory and then saved in a single file that contains the order of the measurement with the corresponding analysis. For cases when the cantilever oscillations are only due to artifact effects, the cantilever oscillations are of similar amplitude. An average of such values is taken as the offset of the measurements. For cases when the resonant frequency coincides with the sample position, an increase in amplitude (with respect to the artifact offset) of oscillation proportional to the force is expected. Matching each of these results with the corresponding position of the gradient magnet results in a mapping of the magnetic force.

A.6 Position Control and Scan

Figure A.18 is the control panel of the XYZ Scan Control II program. It main function is to generate the sawtooth signals and control the displacement of the stages. It can perform, backwards of forwards, single step displacements,

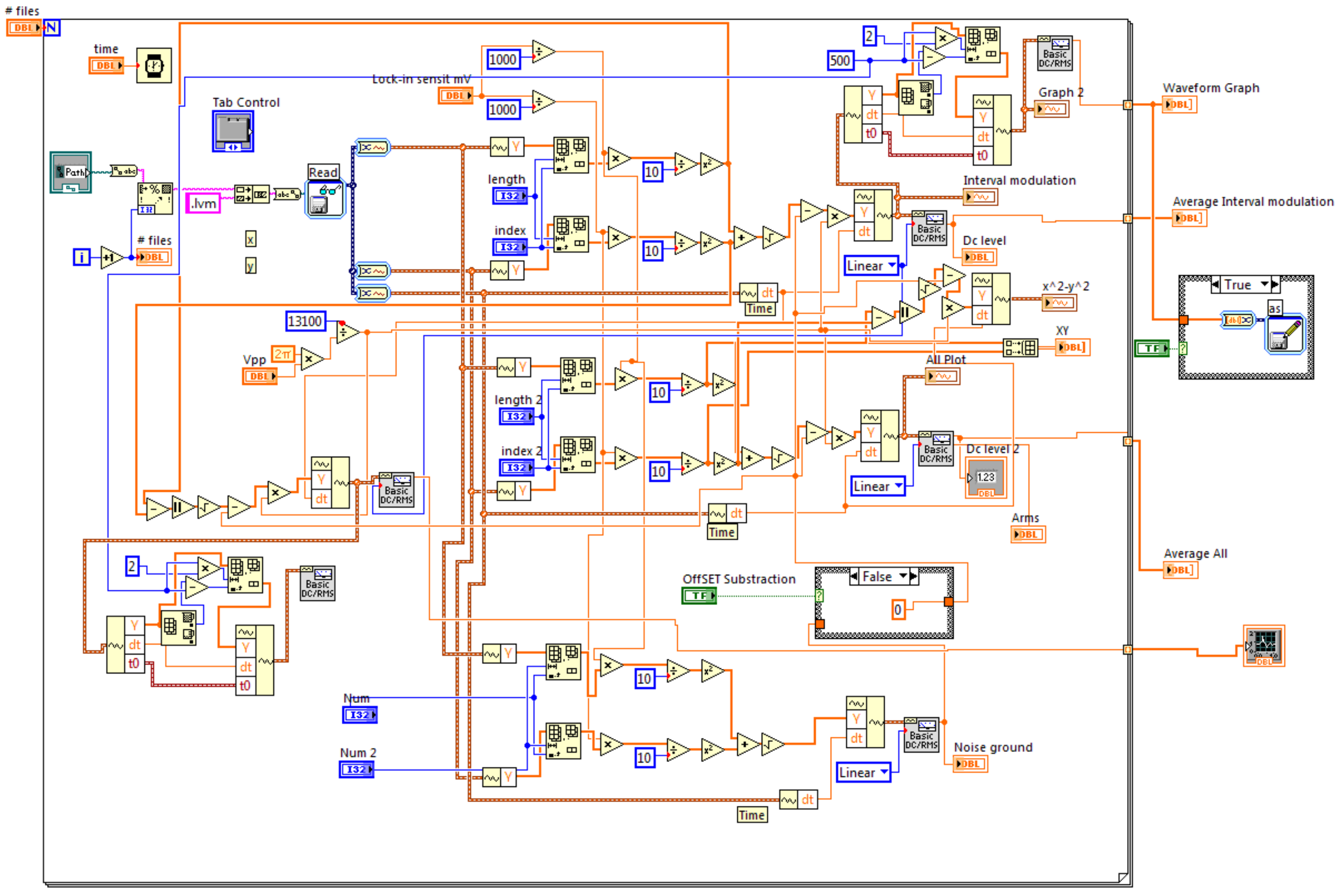

Figure A.17: Diagram of Main Values program used to read the files that form the scan, represent graphically all the values and measure the cantilever's oscillation amplitude.

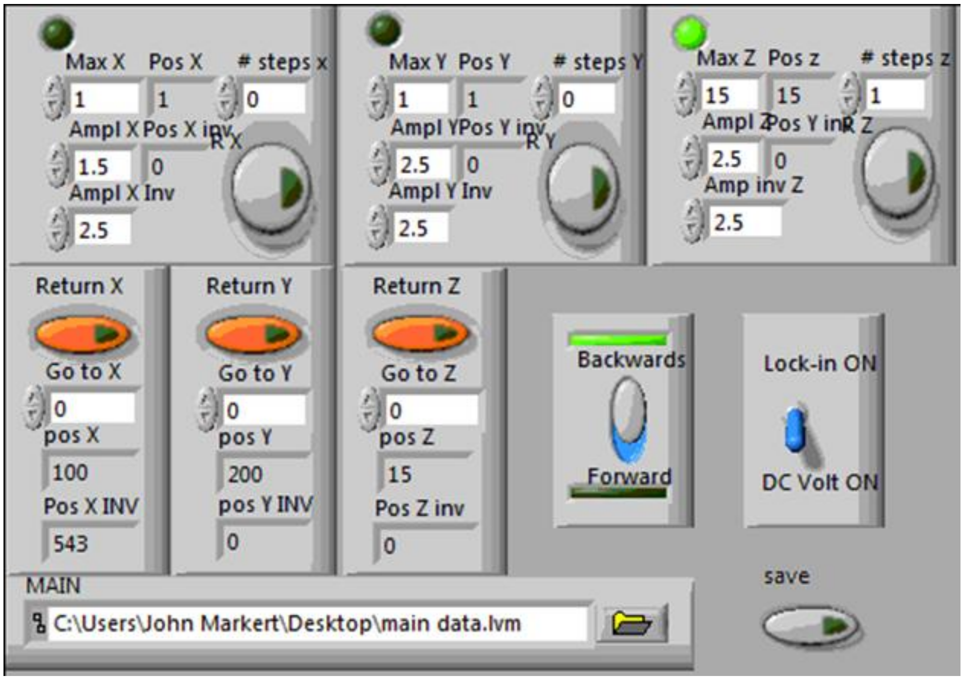

Max X 1
Pos X 1
steps x 0
Ampl X 1.5
Pos X inv 0
Ampl X Inv 2.5

Max Y 1
Pos Y 1
steps Y 0
Ampl Y 2.5
Pos Y inv 0
Ampl Y Inv 2.5

Max Z 15
Pos z 15
steps z 1
Ampl Z 2.5
Pos Y inv 0
Amp inv Z 2.5

Go to X 0
pos X 100
Pos X INV 543

Go to Y 0
pos Y 200
pos Y INV 0

Go to Z 0
pos Z 15
Pos Z inv 0

MAIN C:\Users\John Markert\Desktop\main data.lvm

Figure A.18: Control software to control the displacement of the stages.

with measurements from the interferometer between each step, or continuous displacements in which the measurements are performed at the end of the full displacement. Another possibility is to customize how often measurements are taken between steps. The source of the signal measured is can be DC (multimeter) or AC (lock-in amplifier). Finally for imaging purposes a full 3D scan can be recorded and saved.

Before continuing into the program description, is necessary to explain that to perform three dimensional scans the system starts in the position (x_0, y_0, z_0). During the scan sequence, the gradient magnet moves first to the

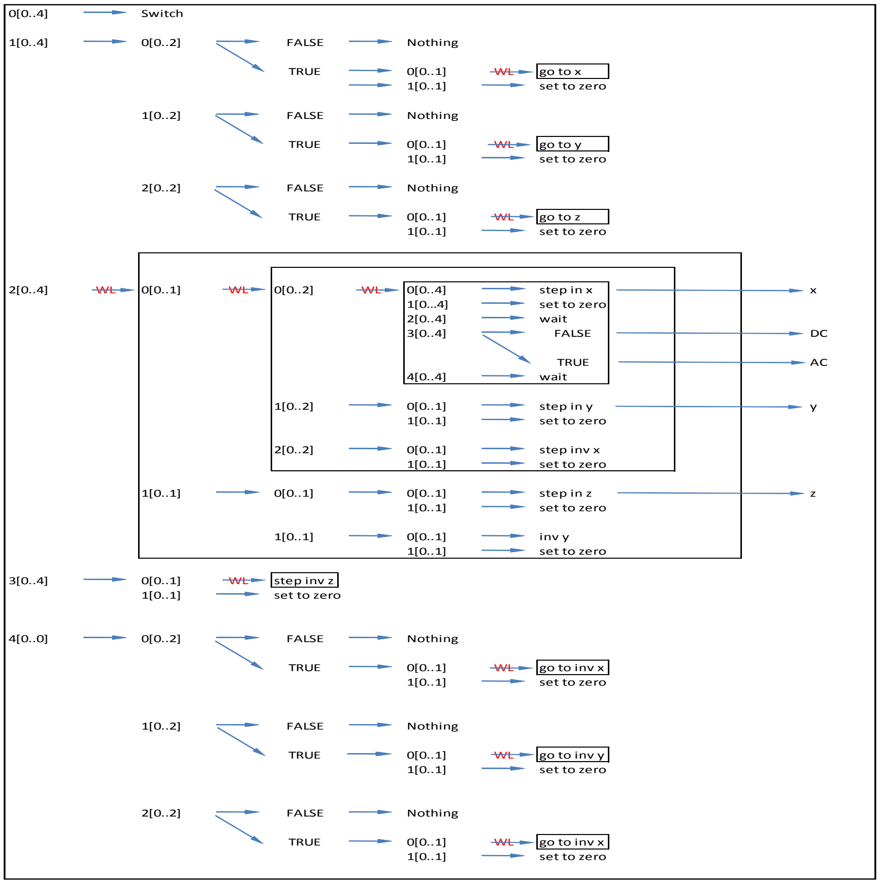

Figure A.19: Schematics of the XYZ Scan program.

x_1 position, second to the x_2 and continues until the position (x_n, y_0, z_0) is reached. Then the system performs a step into the y_1, returns back to x_0, and starts again from (x_0, y_1, z_0) along x until it reaches (x_n, y_1, z_0). The gradient magnet then moves back to (x_n, y_2, z_0) and goes to (x_0, y_2, z_0). When the full plane has been covered, (x_n, y_m, z_0), the stages come back to the (x_0, y_0, z_0) position and a step in z moves the system into the beginning of the second plane. Now with the same technique the second plane can be scanned, and continues until the full scan is completed.

Another thing necessary to keep in mind is that Labview "code" is very different from a typical programming language. Because of the use of so many sequence stacks it is very hard to show the program in a way that one doesn't get lost. To solve this, a schematic diagram is shown in Figure A.19 with a graphical similarity to the "code". I will call each column a level for easy follow up of the indications. For example the first level has 5 stacks, from 0[0..4] to 4[0..4]. Stack 1[0..4] has 3 levels, for example 1[0..4], 1[0..2], and 0[0..1]. True/False is a case structures and is not considered a level, neither the results, go to y, or, set to zero. To finish the introduction, it is necessary to mention the While Loop (WL), whose function is to repeat a sequence until an equality is accomplished.

Moving on, in the first level, the stack sequence has five processes. Figure A.20 shows 0[0..4], a stack sequence structure. Its function is to turn the digital switches to zero so any output sent after this frame will be directed into the piezo stacks and not the signal generator, rf amplifier or voltage attenuator.

The first level, stack 1[0..4] is responsible for the called, go to function, that makes the stages move along x (0[0..2]), y (1[0..2]), or z (2[0..2]) to a specific position. To do so a while loop is responsible for performing a determined number of steps consecutively, until the position indicated is reached. Then a set to zero function is responsible for ensuring that no voltage is sent

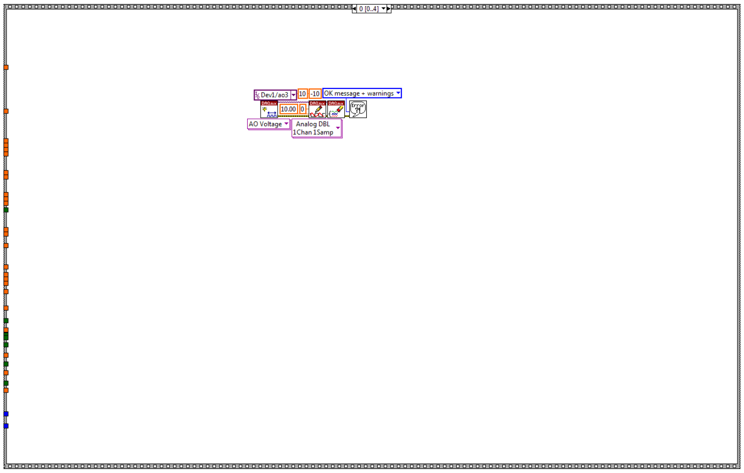

Figure A.20: Control software to turn off the digital switch.

to the piezos. Figure A.21 shows the go to x part of the "code" and the stack path system 1[0..4],(0[0..2], True, (0[0..1])). The set to zero function is shown in A.22 and will always follow a driven function. The false case structure is an empty box used to indicate when a stage does not want to be driven. For example, if only a displacement in the z direction is desired, the x and y paths will end in false and the z in true, and follow the go to function.

The next step is the Stack 2[0..4] located in the first level. It contains the center of the 3D scan system, shown in Figure A.23. To understand this system keep in mind the description of how the scans are performed and a look at the diagram of Figure A.19 will be helpful. The boxes represent a WL that performs repetitions of the sequences indicated inside. Under level one (2[0..4]), first stack (0[0..1]) in level two, and also first stack in level three (0[0..2]) it appears the fourth level with 5 stack sequences. Here, 0[0..4] con-

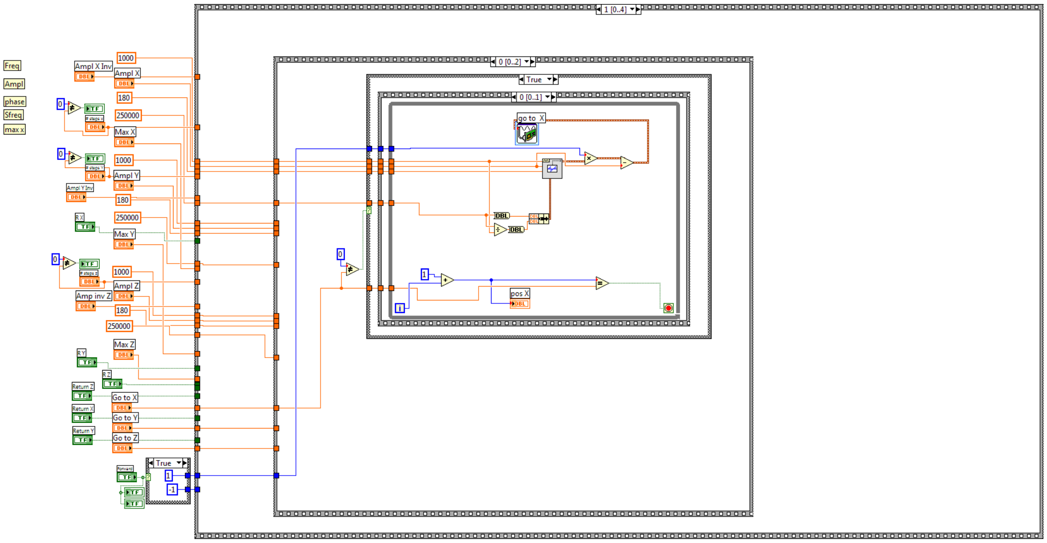

Figure A.21: Go to function that drives the stages consecutively until a determined position is reached.

tains the code to move the stage one step in x shown in Figure A.23. The system waits some time in 1[0..4] (in case the mechanical motion of the stages perturbed the fiber or gradient magnet). After this delay, the system measures the cantilever behavior from the multimeter or lock-in amplifier using a true or false case in 3[0..4], shown in Figure A.24. Finally, the program waits some time in 4[0..4]. If this process is repeated n number of times, the system performs starting at (x_0, y_0, z_0) a scan along the x direction, until the position (x_n, y_0, z_0) is reached.

Now the gradient magnet, located at the fourth level, moves back to the third level 2[0..4], 0[0..2], 1[0..2] in which a step in y, sets the system into the position (x_n, y_1, z_0). Next, in the same level, sequence 2[0..2], contains

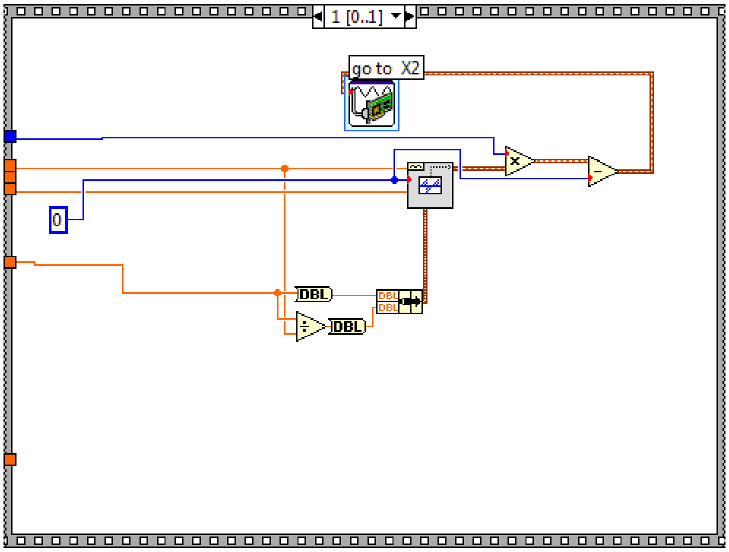

Figure A.22: Set to zero function. used to ensure that no residual voltage is sent to the piezos

the function step inv x, that performs n steps along x, but in the inverse direction, locates the system at (x_0, y_1, z_0). Repeating this whole process m times, a plane of dimension n x m is scanned, ending at (x_n, y_m, z_0).

To obtain the third dimension, again is necessary to move down another level. Now in level 2, but in sequence stack 1[0..1] the system starts moving up to level 4 in which it will perform a step in z setting the system at (x_0, y_m, z_1). Since the next step is to move y steps back using inv y the system will end in (x_1, y_m, z_1) at the origin, but beginning on the plane one level down in z. Repeating the process again first the scan along x, then adding y, performing scans along a plane and adding the z steps, plane by plane, a three dimensional scan can be performed.

Sequence stack 3[0..4] in level one is responsible to ensure that after the scan the position (x_0, y_0, z_0) is reached again after the scan ends. To finalize, in level one sequence stack 4[0..4], the same process as the one used for go to for the three directions is applied but in the reverse direction to ensure that the system reaches the original position as when the program was started.

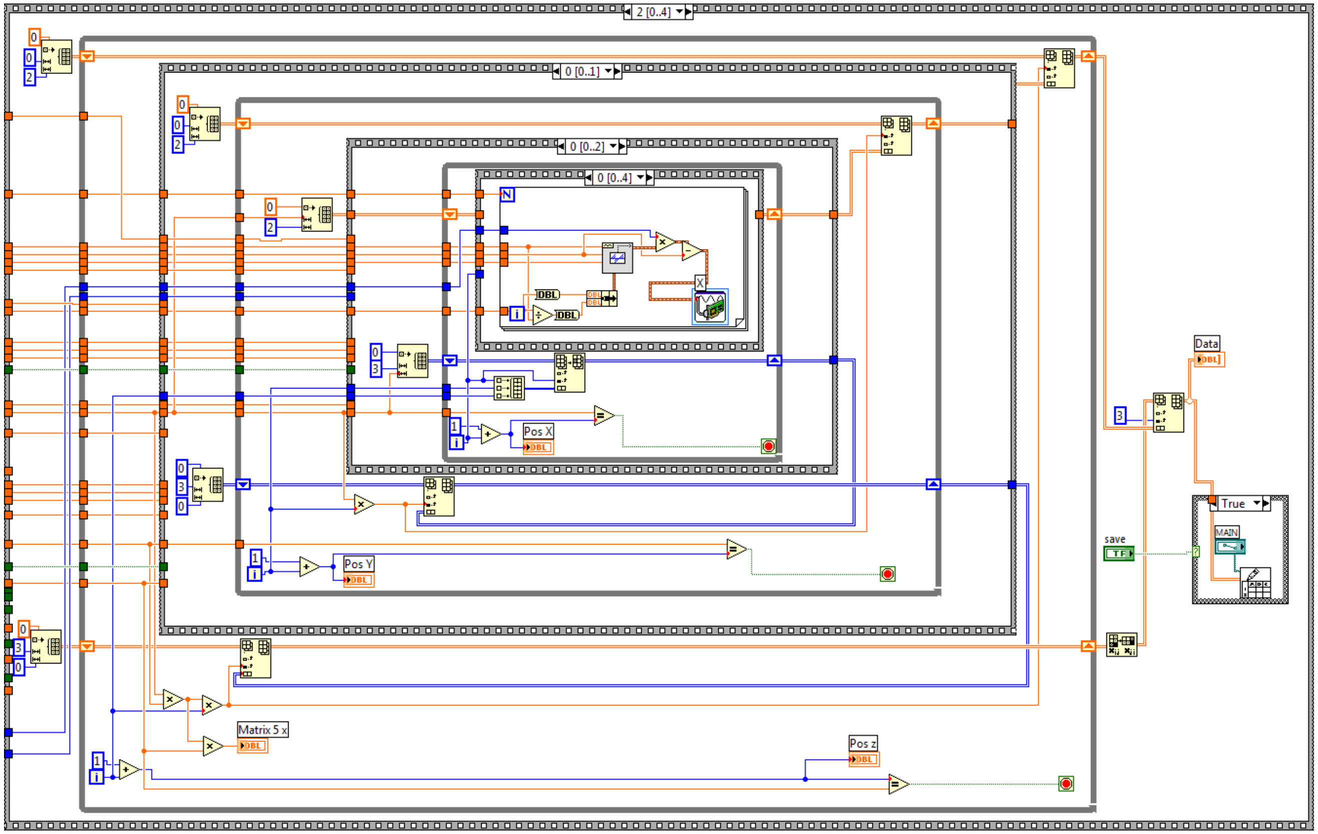

Figure A.23: Software diagram that contains the core of the 3D scan system.

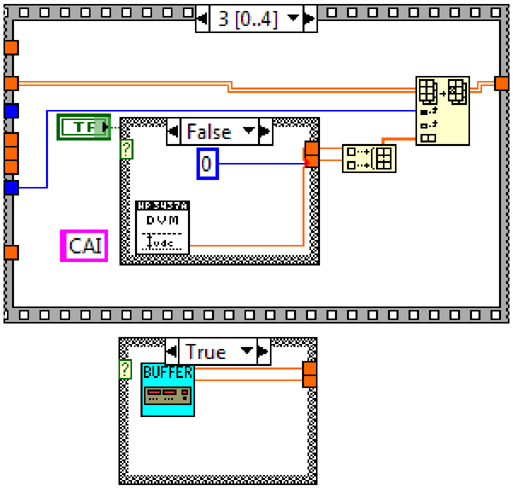

Figure A.24: Software diagram that contains the data acquisition options of DC measurements (multimeter), or AC measurements (multimeter).

Bibliography

[1] J. A. Sidles, “Noninductive detection of single-proton magnetic resonance,” *Applied Physics Letters*, vol. 58, pp. 2854–2856, 1991.

[2] D. Rugar, “Mechanical detection of magnetic resonance,” *Nature*, vol. 360, 1992.

[3] C. L. Degen and M. Poggio and H. J. Mamin and C.T. Rettner and D. Rugar, “Nanoscale magnetic resonance imaging,” *Proceedings of the National Academy of Sciences of the United States of America*, vol. 106, no. 5, pp. 1313–1317, 2008.

[4] J. A. Sidles and D. Rugar, “Signal-to-noise ratios in inductive and mechanical detection of magnetic resonance,” *Physical Review Letters*, vol. 70, no. 22, pp. 3506–3509, 1993.

[5] C. P. Slichter, *Principles of Magnetic Resonance.* Springer-Verlag, 2nd ed., 1980.

[6] A. Abragam, *The Principles of Nuclear Magnetism.* Oxford University Press, 1961.

[7] D. J. Griffiths, *Introduction to Electrodynamics.* Prentice Hall, 3rd ed., 1999.

[8] C. Kittel, *Introduction to Solid State Physics.* Wiley, 6th ed., 1986.

[9] T. Farrar and E. Becker, *Pulse and Fourier Transform NMR Introduction to Theory and Methods.* Academic Press, 1971.

[10] E. Fukushima, *Experimental Pulse NMR, A Nuts and Bolts Approach.* Addison-Wesley, 1981.

[11] J. D. Jackson, *Classical Electrodynamics.* Wiley, 3rd ed., 1999.

[12] D. Rugar and O. Zuger and S. Hoen and C. S. Yannoni and H.-M. Vieth, R. D. Kendrick, "Force detection of nuclear magnetic resonance," *Science*, vol. 264, pp. 1560–1563, 1994.

[13] C. W. Miller, U. M. Mirsaidov, T. C. Messina, and Y. J. Lee, "External effects on the resonant frequency of magnetically capped oscillators for magnetic resonance force microscopy," *Journal of Applied Physics*, vol. 93, no. 10, pp. 6572–6574, 2003.

[14] C. W. Miller, *Nuclear Magnetic Resonance Force Microscopy: Adiabaticity, External Field Effects, and Demonstration of Magnet-on-Oscillator Detection with Sub-Micron Resolution.* PhD thesis, University of Texas, 2003.

[15] C. L. Degen, *Magnetic Resonance Force Microscopy: NMR Spectroscopy on the Micro- and Nanoscale.* PhD thesis, ETH Zurich, 2005.

[16] C. L. Degen, M. Poggio, H. J. Mamin, and D. Rugar, "Role of spin noise in the detection of nanoscale ensembles of nuclear spins," *Physical Review Letters*, 2007.

[17] M. Poggio, C. L. Degen, C. T. Rettner, H. J. Mamin, and D. Rugar, "Nuclear magnetic resonance force microscopy with a microwire rf source," *Applied Physics Letters*, 2007.

[18] J. Mamin, M. Poggio, C. Degen and D. Rugar, "Nuclear magnetic resonance imaging with 90-nm resolution," *Nature*, 2007.

[19] L. A. Madsen, G. M. Leskowitz, and D. P. Weitekamp, "Observation of force-detected nuclear magnetic resonance in a homogeneous field.," *PNAS*, vol. 101, 2004.

[20] C. L. Degen, M Poggio,H. J. Mamin, C. T. Rugar, "Nanoscale magnetic resonance imaging," *Proceedings of the National Academy of Sciences, PNAS*, vol. 106, 2009.

[21] H. J. Mamin and D. Rugar, "Sub-attonewton force detection at millikelvin temperatures," *Applied Physics Letters*, 2001.

[22] D. Rugar, B.C. Stipe, H.J.Mamin, C.S. Yannoni, T.D. Stowe, K.Y. Yasumura, T.W. Kenny, "Adventures in attonewton force detection," *Appl. Phys. A*, 2001.

[23] U. Mirsaidov, *Nuclear Magnetic Resonance Force Microscopy of Ammonium Dihydrogen Phosphate and Magnetism of Cobalt Nanocrystals.* PhD thesis, The University of Texas at Austin, 2005.

[24] Tse Nga Ng, Neil E. Jenkins, and John A. Marohn, "Thermomagnetic fluctuations and hysteresis loops of magnetic cantilevers for magnetic resonance force microscopy," *IEEE Transactions on Magnetics*, 2006.

[25] B. C. Stipe, H. J. Mamin, T. D. Stowe, T.W. Kenny, and D. Rugar, "Magnetic dissipation and fluctuations in individual nanomagnets measured by ultrasensitive cantilever magnetometry," *Phys. Rev. Lett.*, 2001.

[26] Fei Xue, P. Peddibhotla, M. Montinaro, D. P. Weber, and M. Poggio, "A geometry for optimizing nanoscale magnetic resonance force microscopy," *Applied Physics Letters*, 2011.

[27] J. G. E. Harris, R. Knobel, K. D. Maranowski, A. C. Gossard N. Samarth, and D. D. Awschalom, "Damping of micromechanical structures by paramagnetic relaxation," *Applied Physics Letters*, 2003.

[28] B. C. Stipe, H. J. Mamin, T. D. Stowe, T.W. Kenny, and D. Rugar, "Noncontact friction and force fluctuations between closely spaced bodies," *Physical Review Letters*, 2001.

[29] Steven A. Hickman, Eric W. Moore, SangGap Lee, Jonilyn G. Longenecker, Sarah J. Wright, Lee E. Harrell, and John A. Marohn, "Batch-fabrication of cantilevered magnets on attonewton-sensitivity mechani-

cal oscillators for scanned-probe nanoscale magnetic resonance imaging," *ACSNANO*, 2010.

[30] S. A. H. Seppe Kuehn and J. A. Marohn, "Advances in mechanical detection of magnetic resonance," *The Journal of Chemical Physics*, 2008.

[31] T. D. Stowe, K. Yasumura, and T. W. Kenny, D. Botkin, K. Wago, and D. Rugar, "Attonewton force detection using ultrathin silicon cantilevers," *Appl. Phys. Lett.*, 1997.

[32] M. D. Chabot, *Force Detection of Nuclear Magnetic Resonance using Double-Torsional Micro-Oscillators*. PhD thesis, The University of Texas at Austin, 2001.

[33] W. Lu, *Fabrication and Characterization of a Double Torsional Mechanical Oscillator and its Application in Gold Micromass Measurements*. PhD thesis, The University of Texas at Austin, 2008.

[34] Y. J. Lee, *Construction of a Low Temperature Nuclear Magnetic Resonance Force Microscope*. PhD thesis, The University of Texas at Austin, 2006.

[35] H.-J. Chia, *Force Detected Nuclear Magnetic Resonance on* $(NH_4)_2SO_4$ *and* MgB_2. PhD thesis, University of Texas, 2009.

[36] T. J. Nordland, "Ferroelectric mode in ammonium sulfate," *J. Chem. Phys.*, 1976.

[37] R. Goc, “Calculation of the nmr second moment for materials with different types of internal rotation,” *Solid State Nucl. Magn.*, 1988.

Index

Vita

Isaac Vicente Manzanera Esteve, was born Valencia, Spain on June 09, 1977. He attended the University of Valencia and received Bachelor of Science with a degree in Physics. During this time in 2003 he attended the University of Texas where he spent a year as an exchange student. He applied to graduate school at the University of Texas and was accepted to the physics department in 2005. Immediately, he started to work in the laboratory of John T. Markert focusing primarily on Nuclear Magnetic Resonance Force Microscopy. After graduation he will work with John C. Gore, PhD. Director; pursuing research involving 15T imaging and parahydrogen hyperpolarized imaging at the Vanderbilt University Institute of Imaging Science.

This dissertation was typed by the author. You can contact the author at: imanes@physics.utexas.edu